B

A Second Interaction Region For Gamma-Gamma, Gamma-Electron and Electron-Electron Collisions

Contents

B.1 Introduction . . . 973
B.2 Physics Opportunities at $\gamma\gamma$ Collider: The Higgs Sector and Other New Physics . . . 974
B.2.1 The Higgs $\gamma\gamma$ Partial Width . . . 974
B.2.2 Higgs CP Eigenvalue . . . 975
B.2.3 Higgs Boson Search . . . 976
B.2.4 Strongly Interacting Electroweak Sector . . . 976
B.2.5 Supersymmetry . . . 977
B.2.6 Compositeness . . . 977
B.3 Major Parameters . . . 978
B.3.1 Basic Scheme . . . 978
B.3.2 Laser Parameters . . . 978
B.3.3 Electron Beam Parameters . . . 979
B.4 CP Issues . . . 980
B.4.1 Optimization of the Laser Parameters . . . 980
B.4.2 Low-Energy Electrons Due to High-Order Multiple Scattering . . . 983
B.4.3 Compton Conversion Efficiency . . . 984
B.5 IP Issues . . . 987
B.5.1 Optimization of Spectral Luminosity . . . 987
B.5.2 Polarization . . . 987
B.5.3 Collision of the Spent Electron Beam . . . 987
B.5.4 Disruption of Low Energy Electrons . . . 988
B.6 Luminosity Calculations . . . 989
B.6.1 Simulation Code Development . . . 989
B.6.2 Simulation of the CP . . . 990
B.6.3 Telnov's Simulation Results for $\gamma\gamma$, γe^- and e^-e^- Luminosities . . . 990
B.7 Backgrounds and Other Detector Considerations . . . 999
B.7.1 Introduction . . . 999
B.7.2 Physics Requirements . . . 999
B.7.3 Backgrounds . . . 1000
B.7.4 Detector Considerations . . . 1000
B.7.5 Initial Simulations . . . 1002
B.7.6 Conclusions . . . 1003

B.8 Laser Optical Path in IR . . . 1006
B.8.1 Single-Pass Scheme . . . 1006
B.8.2 Optical Beam Focusing . . . 1009
B.8.3 Laser Damage of Optics . . . 1010
B.8.4 Ideas on Relaxing Average Laser Power Requirement Via Multipass Optics . . . 1013
B.9 Gamma-Gamma Final Focus System . . . 1015
B.9.1 Beam Parameters . . . 1015
B.9.2 Final Focus Doublet . . . 1016
B.9.3 Chromaticity Compensation . . . 1017
B.10 Extraction and Diagnostic Line . . . 1019
B.11 Laser Technology I: Solid State Lasers . . . 1020
B.11.1 Laser Materials . . . 1020
B.11.2 Chirped-Pulse Amplification . . . 1021
B.11.3 High-intensity, Short-pulse Laser Systems . . . 1023
B.11.4 Synchronization and Repetition Rate . . . 1024
B.11.5 1-ps, 1-J Laser System for Nonlinear QED Experiments . . . 1024
B.11.6 Average Power . . . 1024
B.11.7 NLC Laser Concept . . . 1025
B.11.8 A Ring Configuration for Multiplexing and Polarization Control . . . 1026
B.11.9 Polarization Control at the Interaction Point . . . 1028
B.11.10 Conclusion . . . 1029
B.12 Free-Electron Lasers . . . 1030
B.12.1 An FEL Scheme Using Induction Linac and Chirped Pulse Amplification Technique . . . 1030
B.12.2 Chirping Requirement and Tolerance . . . 1032
B.12.3 Induction Linac Driver . . . 1032

B.1 Introduction

To maximize the accessible high-energy physics, the NLC will have two interaction regions (IRs): one will study e^+e^- collisions and the other may study $\gamma\gamma$, γe^-, and e^-e^- collisions. In this appendix, we describe the final focus and interaction region required for $\gamma\gamma$ and γe^- collisions, henceforth referred to as IR2.

For both $\gamma\gamma$ and γe^- collisions, the required high-energy photons (γ beams) are most effectively produced via Compton backscattering of focused laser beams by the high-energy electron beams. The high-energy photon beams are then brought into collision with opposing electron and photon beams for γe^- collisions and $\gamma\gamma$ collisions, respectively. This region is distinctly different from the e^+e^- final focus and interaction region in that the final focus is optimized to produce rounder beams and that the IR must contain one IP for the luminosity collision and one or two conversion points where the photon beams are generated. With suitable laser and electron beam parameters, a luminosity of γe^- or $\gamma\gamma$ collisions comparable to that of the e^+e^- collisions can be achieved. The polarization of the high-energy photons can be controlled by the polarizations of the laser and the electron beams. With high luminosity and variable polarization, the $\gamma\gamma$ and γe^- collisions at TeV energies will significantly enhance the discovery potential and analytic power of a TeV linear collider complex. A conceptual layout of the NLC including the second IR for $\gamma\gamma$ collisions is shown in Figure B-1.

A review of $\gamma\gamma$ and γe^- colliders can be found in the proceedings of a workshop at Berkeley [Berkeley 1995]. The idea of incorporating γe^- or $\gamma\gamma$ collisions in a future linear collider via Compton backscattering of a laser beam [Arutyunian 1963] has been studied conceptually, especially by scientists from Novosibirsk [Ginzburg 1981, Ginzburg 1983, Ginzburg 1984, Telnov 1990, Telnov 1991, Telnov 1995]. The nonlinear QED experiment E-144 [Heinrich 1991] on the FFTB line at SLAC may be regarded as an essential "proof-of-principle" for future $\gamma\gamma$ or γe^- colliders.

The physics opportunities for γe^- and $\gamma\gamma$ collisions at the NLC are described in Section B.2. Some examples are [Brodksy 1994, Chanowitz 1994, Ginzburg 1994]:

- A $\gamma\gamma$ collider offers a unique opportunity for measuring the two-photon decay width of the Higgs boson, providing a glimpse of the mass scale beyond the TeV range.
- A $\gamma\gamma$ collider is well suited for searching for new charged particles, such as SUSY particles, leptoquarks, excited state of electrons, etc. because photons generally couple more effectively to these particles than do electrons or positrons.
- A $\gamma\gamma$ or γe^- collider serving as a W-factory, producing 10^6–10^7 Ws/year, allowing for a precision study of gauge boson interactions and a search for their possible anomalies.
- A γe^- collider is uniquely suited to studying the photon structure functions, etc..
- e^-e^- collisions (without conversion to γ rays) are interesting by themselves.

In the following, we describe a preliminary design of the IR2 for the NLC, with the goal of obtaining $L_{\gamma\gamma}$ about $10^{33}\,\mathrm{cm}^{-2}s^{-1}$ within a 10% bandwidth or several times $10^{33}\,\mathrm{cm}^{-2}s^{-1}$ for a broad spectrum. In this design, we chose to employ the electron beam parameters for the e^+e^- collision before the final focus system (FFS). However, the FFS for the $\gamma\gamma$ collision is modified so that $\beta_x^* = \beta_y^* < 1$ mm. An FFS satisfying the luminosity requirements is worked out with a tolerance requirement similar to that of the e^+e^- FFS. An elaborate optical mirror system in the very constrained region around the vertex detector and quadrupoles brings the laser beam into a tight focus at the conversion point (CP) located 5 mm upstream of the interaction

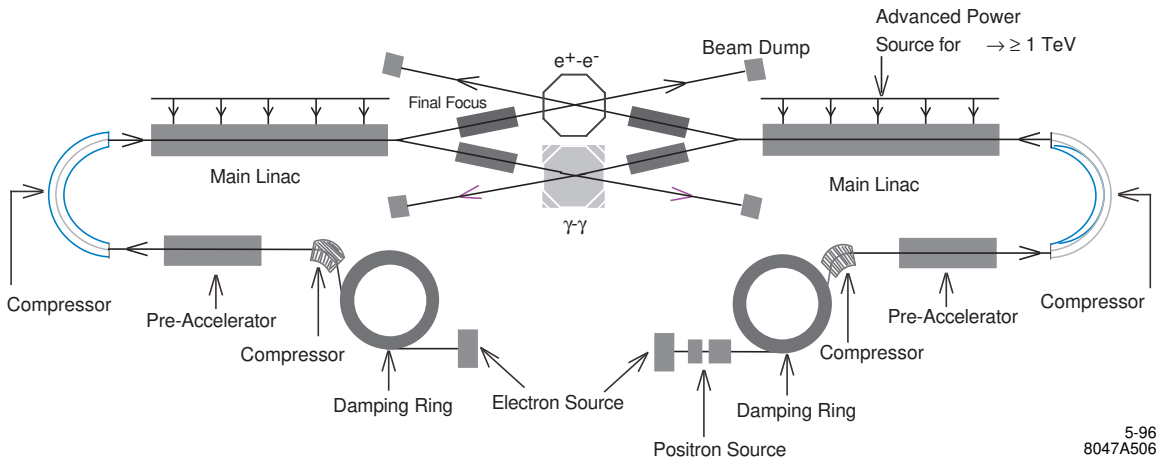

Figure B-1. *Next Linear Collider layout with a second IR for $\gamma\gamma$ collisions.*

point (IP). The laser required for the Compton conversion must have a TW of peak power and tens of kW of average power. Such a laser can be built by either combining diode pumping and chirped pulse amplification in solid-state lasers or by a free-electron laser driven by an induction linac and using chirped pulse amplification.

The phenomenon limiting the performance of the $\gamma\gamma$ collisions are different from those in the case of the e^+e^- collisions; the beamstrahlung is absent in the $\gamma\gamma$ collisions, while the e^+e^- pair creation is still important. Therefore the optimization of e-beam parameters for IR2 would be quite different from the case of IR1. Therefore it is worthwhile to revisit the damping rings and linac designs towards obtaining a smaller emittance and/or larger number of particles per bunch at a reduced pulse repetition rate if necessary. These more challenging topics are not pursued in this report.

B.2 Physics Opportunities at $\gamma\gamma$ Collider: The Higgs Sector and Other New Physics

Several review articles have been written on research that could be performed at the IR2 [Brodksy 1994, Chanowitz 1994, Ginzburg 1994]. In this section we focus on the new physics studies, especially concerning the properties of Higgs bosons. Other topics such as the study of the $t\bar{t}$ threshold region, and of the photon structure functions in the $e\gamma$ mode are omitted here.

B.2.1 The Higgs $\gamma\gamma$ Partial Width

One of the most interesting physics programs at a $\gamma\gamma$ collider is the measurement of the Higgs boson partial width into $\gamma\gamma$. This partial width is sensitive to physics beyond the Standard Model because heavy particles whose masses originate in the Higgs mechanism do not decouple in the one-loop diagram [Gunion 1993]. For

instance, the fourth generation contributes to the partial width even in the limit where its mass becomes infinity. Therefore, a study of the partial width may indicate new physics.

A plot of $\Gamma(H \to \gamma\gamma)$ with new physics contributions is shown in Figure 2.1 of Ref. [Gunion 1993].

Here we discuss measurements of the partial width $\Gamma(H \to \gamma\gamma)$ for two cases separately, if H decays predominantly into $b\bar{b}$ ($m_H \leq 150\,\mathrm{GeV}$ in the Standard Model) or WW and ZZ (for heavier Higgs in the Standard Model).

$\gamma\gamma \to H \to b\bar{b}$

For this measurement, it is preferred to use the electron helicity to make the photon energy spectrum peaked at its high end, and fix the ee center of mass energy to put the Higgs mass at the peak of the $s_{\gamma\gamma}$ spectrum. The most dominant background is the continuum production $\gamma\gamma \to b\bar{b}$ and $c\bar{c}$. It was pointed out [Barklow 1990] that a $J = 0$ combination of the photon helicities $(++)$ or $(--)$ significantly suppresses the background as m_b^2/s (m_c^2/s) because of the fermion chirality conservation. Furthermore, the continuum production prefers small angles while the signal is isotropic. A cut on the angle, *e.g.*, $|\cos\theta_b| < 0.7$, significantly suppresses the background. For a Standard Model Higgs boson in the intermediate mass range, $80 \leq m_H \leq 150\,\mathrm{GeV}$, the signal cross section is 300–1000 fb level and well above the background after the cuts. Statistical accuracy of $\Gamma(H \to \gamma\gamma)$ is ~5% with an integrated luminosity of 20 fb^{-1}, assuming a b-tagging efficiency of 50% and a $c\bar{c}$-to-$b\bar{b}$ acceptance ratio of 5% [Borden 1993a].

The above analysis has two limitations. One is that the resolved photon contribution to the continuum $b\bar{b}$ production may be important [Eboli 1993]. It can, however, be suppressed by choosing the center-of-mass energy such that m_H lies at the maximum $\gamma\gamma$ energy. The $b\bar{b}$ events produced by resolved photon contribution has typically much lower energy and hence can be suppressed using a visible energy cut. The other limitation is $b\bar{b}g$ or $c\bar{c}g$ final states [Borden 1994, Jikia 1994a]. They appear at higher orders in α_s, but do not have m_f^2/s suppression even in a $J = 0$ helicity combination. Still, suitable kinematical cuts eliminate most of the backgrounds from bbg and ccg [Borden 1994], requiring at least five tracks with a large impact parameter >4 sigma (with $\sigma \simeq 30\,\mu$m) to reject cs. It was also pointed out that the previous studies did not optimize the center-of-mass energy to reduce the backgrounds. By putting m_H on the top of the $s_{\gamma\gamma}$ spectrum, a measurement of $\Gamma(H \to \gamma\gamma)$ is possible with 6% accuracy 20 fb^{-1} [Watanbe 1995].

$\gamma\gamma \to H \to ZZ$

If the Higgs boson is heavier and decays predominantly into vector bosons WW or ZZ, the $b\bar{b}$ mode discussed above is not useful. One cannot use the WW mode either because of its huge tree-level production cross section of ~100 pb. Even the ZZ mode suffers from one-loop production via the W-loop [Jikia 1993], but it is manageable for $m_H \leq 350\,\mathrm{GeV}$. One can measure the partial width $\Gamma(H \to \gamma\gamma)$ at 10% level for small m_H, but the signal is lost for $m_H < 350\,\mathrm{GeV}$ [Borden 1993b].

B.2.2 Higgs CP Eigenvalue

A measurement of the Higgs boson property special at a $\gamma\gamma$ collider is to decide definitively whether a particular Higgs boson is CP even or odd [Grzadkowski 1992, Kramer 1994]. The basic idea is that a CP-even Higgs boson, H^0, couples to the photon with $\mathcal{L} \sim H^0(\vec{E}\cdot\vec{E} - \vec{B}\cdot\vec{B})$, while a CP-odd one, A^0, couples

with $\mathcal{L} \sim A^0 \vec{E} \cdot \vec{B}$, where $\vec{E}$ is the electric and $\vec{B}$ the magnetic field strength of photon. If the two colliding photon beams are linearly polarized, their polarizations have to be parallel to produce a CP-even state H^0 while they ought to be perpendicular to produce a CP-odd state A^0. Therefore, the asymmetry

$$A \equiv \frac{\sigma(\text{parallel}) - \sigma(\text{antiparallel})}{\sigma(\text{parallel}) + \sigma(\text{antiparallel})} \tag{B.1}$$

is $+1$ for H^0 and -1 for A^0. The studies in Refs. [Grzadkowski 1992, Kramer 1994] showed that an integrated luminosity of 100 fb^{-1} is enough to determine the CP eigenvalue if they decay dominantly into $b\bar{b}$.

B.2.3 Higgs Boson Search

An advantage of a $\gamma\gamma$ collider is that one can use full center-of-mass energy to produce Higgs bosons in s-channel, while one may need to produce them in pairs at the e^+e^- mode. For instance, the heavy CP-even Higgs H^0 and CP-odd Higgs A^0 in the minimal supersymmetric standard model (MSSM) are produced in an association $e^+e^- \to H^0A^0$, while their production with Z^0 (Z^0H^0 or Z^0A^0 final states) are suppressed if $m_{A^0} \gtrsim 300$ GeV. On the other hand, a $\gamma\gamma$ collider can produce A^0 and H^0 states with its full center-of-mass energy, and can be used as a discovery machine even if their threshold lies beyond the e^+e^- center-of-mass energy. Using basically the same strategy in looking for the Standard Model Higgs decaying to $b\bar{b}$, one can cover a substantial region of the parameter space. The final states $t\bar{t}$ or $H^0 \to h^0h^0$ can be used as well. The $t\bar{t}$ final state suffers from continuum background, and the $t\bar{t}g$ final state has been calculated [Kamal 1995]. Even though more studies are necessary, the detection seems to be feasible.

There is a potential problem with their supersymmetric decay modes. For instance, $A^0 \to \tilde{\chi}_1^0\tilde{\chi}_1^0$ may be open and dominate the decay branching ratio, which does not leave any visible signature [Gunion 1995].

For a light Standard Model Higgs boson decaying into $b\bar{b}$, the high-energy part of the broad-band photon energy spectrum from the γ-conversion does an excellent job for the discovery. With $\sqrt{s_{ee}} = 500$ GeV, 10 fb^{-1} and broad-band spectrum, one can observe Higgs bosons for $m_H = 110$–140 GeV [Baillargeon 1995]. Of course, with lower center-of-mass energy (*e.g.,* 350 GeV), discovery reach extends to lower mass (90 GeV). This capability is desired especially when the $\gamma\gamma$ collision operates at the second collision point of an e^+e^- collider and one cannot vary the center-of-mass energy freely.

For heavy Standard Model Higgs bosons decaying predominantly into WW and ZZ, one needs to go to WWH final state, and it requires a large luminosity. For instance, with $\sqrt{s_{ee}} = 1.5$ TeV and 200 fb^{-1}, one can observe up to 700-GeV Higgs bosons [Jikia 1994b, Cheung 1994].

B.2.4 Strongly Interacting Electroweak Sector

The study of the electroweak symmetry breaking sector is difficult if it is strongly interacting as it is for any other colliders, *e.g., pp* or e^+e^-. The main reasons for the difficulty are that there is no light degrees of freedom in the sector and the only signature is the tail of strong interaction among longitudinal W-boson or top quark above the TeV scale. Even though a $\gamma\gamma$ collider has a huge cross section to produce a W-pairs, they are predominantly transversely polarized and are not sensitive to the strong interactions.

There are discussions to study $WWWW$ or $WWZZ$ final states at $\gamma\gamma$ colliders [Jikia 1994b, Cheung 1994]. However, their study typically requires center-of-mass energy *higher* than their e^+e^- cousin, and probably

not of a main target of the first stage $\gamma\gamma$ collider. For instance, it was discussed that at $\sqrt{s_{ee}} = 2$ TeV, one needs a luminosity more than 200 fb^{-1} to observe strong interaction among the W_Ls [Jikia 1994b].

Another possible signature of the strongly-interacting electroweak sector is the energy dependence of the $t\bar{t}$ production cross section. Suppose the top quark mass is generated by an effective four-fermion interaction, $\mathcal{L} \sim \frac{1}{\Lambda^2} t\bar{t}Q\bar{Q}$, where Λ is the scale of extended technicolor or its analog, and Q is a techniquark which condenses to break electroweak symmetry. Due to a loop diagram of techniquarks Q, the $t\bar{t}$ production cross section can be significantly reduced [Asaka 1995]. A possible techni-eta meson may be observed at the $\gamma\gamma$ mode as well [Tandean 1995]. Clearly, more discussions and studies are necessary for the case of the strongly interacting electroweak sector.

B.2.5 Supersymmetry

If supersymmetry exists, charged superparticles can be produced at a $\gamma\gamma$ collider with reasonable cross sections. For many of them, W-pair is the main background. For instance, a pair of sleptons $\tilde{l}^+\tilde{l}^-$ can be produced which decays into $l^+\tilde{\chi}_1^0 l^-\tilde{\chi}_1^0$. While W-pairs can lead to the same signature, one can obtain a relatively clean sample of signals after suitable cuts [Kon 1993]. Mass measurement of sleptons and neutralinos can be done at a 5% level with 20 fb^{-1} [Murayama 1994]. Charginos suffer more from the W-pair background, and more studies are necessary.

The backscattered laser beam allows us to use the $e\gamma$ mode to extend the discovery reach of selectron $\tilde{e}$, and in the process $e\gamma \to \tilde{e}\tilde{\chi}_1^0$. A selectron can be produced even if the e^+e^- center-of-mass energy is below the threshold of its pair production, up to $m_{\tilde{e}} < \sqrt{s_{e\gamma}} - m_{\tilde{\chi}_1^0}$ [Kon 1992a].

B.2.6 Compositeness

If some of the particles in the Standard Model are a composite of more fundamental objects, they exhibit either (1) excited states decaying into the ground state by γ, Z, or g radiation, or (2) anomalous interactions at the low-energy limit of their form factors.

If the electron is a composite, one can look for its excited state e^* in the process $e\gamma \to e^* \to e\gamma$ [Kon 1992b].

If a W-boson is a composite, it may have an anomalous magnetic moment or electric quadrupole moment (assuming CP invariance). The huge W-pair production cross section from $\gamma\gamma$ allows us a precise measurement of such anomalous moments [Yehudai 1991, Gounaris 1995]. Another process $e^-\gamma \to \nu_e W^-$ can be also used [Yehudai 1990, Raidal 1995]. One can obtain constraints complementary to that from an e^+e^- mode.

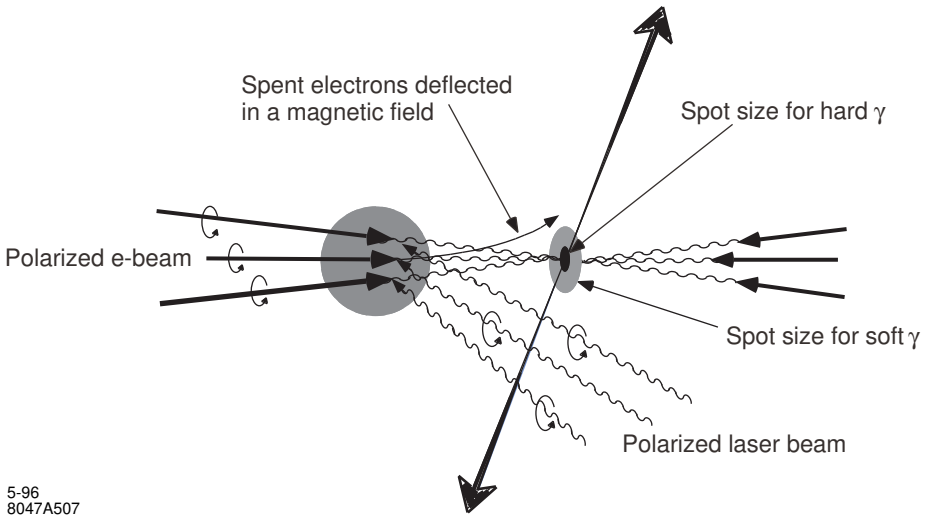

Figure B-2. *General scheme of $\gamma\gamma$ collision.*

B.3 Major Parameters

B.3.1 Basic Scheme

The basic scheme of the IR2 for $\gamma\gamma$ collisions is shown in Figure B-2. Two electron beams from their respective final-focus system (FFS) are heading toward the IP. At a location a short distance (5 mm for this design) upstream from the IP, referred to hereafter as the conversion point (CP), a laser beam is focused and Compton-backscattered by the electrons, resulting in a high-energy beam of photons. The photon beam follows the original electron motion (with a small angular spread of order $1/\gamma$) and arrives at the IP in a tight focus. It collides at the IP with an opposing high energy photon beam similarly produced by a second electron beam.

The spent electron beam, following its interaction at the CP, together with the photon beam will cause background γe^- and e^-e^- events as well as producing copious beamstrahlung photons, which will further increase the backgrounds, in interaction with the other electron beam. Extensive detector simulation is required to determine whether these background poses significant problem for a given experiment. One way to reduce the background is to place a bending magnet [Ginzburg 1983] between the CP and the IP, so that the spent beams miss each other. Implementing the sweeping magnet in the tight space in the IR2 is a challenging problem.

B.3.2 Laser Parameters

The laser beam must be chosen to optimize the generation of the gamma-rays via Compton scattering at the CP. The relevant laser parameters at the CP are summarized in Table B-1. The wavelength and the peak intensity of the required laser are similar to that available in the E-144 experiment at SLAC [Heinrich 1991].

Wavelength	$\lambda = 1.053\,\mu$m
Micropulse energy	$A = 1$ J
Repetition rate	The same as the electron beam pulse rate
	(90 micropulses separated by 1.4 ns repeating at 180 Hz)
Rayleigh length	$Z_R = 0.1$ mm
Rms spotsize at waist	$\sigma_{Lx} = \sigma_{Ly} = 2.90\,\mu$m
Rms angular divergence	$\sigma'_{Lx} = \sigma'_{Ly} = 28.9$ mr
Rms micropulse length	$\sigma_{Lz} = 0.23$ mm
Peak intensity	$\approx 1 \times 10^{18}$ W/ cm^2
Peak power	0.5 TW
Average power	16.2 kW
Transverse coherence	Near diffraction limited
Polarization	Fully polarized with helicity switching capability

Table B-1. *Laser parameters for a reference design at $E_{CM} = 500$ GeV.*

However, the average power is two orders of magnitude larger than what is currently available. In computing the laser spotsize, it is useful to remember the following correspondence between the electron beam and the light beam:

$$\epsilon_x, \epsilon_y \leftrightarrow \frac{\lambda}{4\pi} \tag{B.2}$$

$$\beta^*_x, \beta^*_y \leftrightarrow Z_R \tag{B.3}$$

The quantity Z_R is known as the Rayleigh length in optics literature. Thus, the rms spotsize $\sigma_{Lx} = \sigma_{Ly}$ and the cross section Σ at the focus are respectively given by

$$\sigma_{Lx} = \sqrt{\frac{\lambda}{4\pi} Z_R}, \tag{B.4}$$

$$\Sigma \equiv 2\pi\sigma^2_{Lx} = \frac{1}{2}\lambda Z_R \tag{B.5}$$

The considerations leading to the parameters in Table B-1 are given in B.4.

B.3.3 Electron Beam Parameters

The electron beam parameters for the reference design at 500-GeV CM energy are summarized in Table B-2.

The $\gamma\gamma$ or γe^- luminosity is approximately proportional to the e^-e^- geometric luminosity. Although we can in principle reexamine the design of the damping ring–linac complex from the point of maximizing the geometric e^-e^- luminosity, we have chosen for this initial design of the IR2 to use the same electron beam parameters before the IR1 for the e^+e^- collision. However, the beta-functions at the IP are chosen differently from the ones for the e^+e^- collision—with a relaxed β^*_y and a tighter β^*_x. This is due to the fact that the CP is separated from the IP (by 5 mm) to suppress the low-energy part of the $\gamma\gamma$ luminosity spectrum. The separation will introduce an increase in the spotsize of the gamma-ray photons at the IP due to their angular spread $\approx 1/\gamma$ relative to the electron beam. The vertical β^*_y could be larger than that in the case of the e^+e^- collision. It is necessary to reduce β^*_x to compensate the reduction in the luminosity when β^*_y is increased. With $\beta^*_x = \beta^*_y = 1$ mm, the geometric luminosity would be the same as in the case of the e^+e^- collision.

Luminosity goal	$\sim 10^{33}$ cm$^{-2}s^{-1}$ for 10 % BW
	$\sim 5 \times 10^{33}$ cm$^{-2}s^{-1}$ for broad band
Beam parameters before FFS	The same as e^+e^- design:
Electron energy	250 GeV
Rep. rate	90 bunches separated by 1.4 ns, 180 Hz
Particles per bunch	$N_e = 0.65 \times 10^{10}$
Normalized rms emittance	$\gamma\epsilon_x = 5 \times 10^{-6}$ mr, $\gamma\epsilon_y = 8 \times 10^{-8}$ mr
Beta function at the IP	$\beta_x^* = \beta_y^* = 0.5$ mm
Rms spotsize at the IP	σ_x^*/σ_y^* =71.5/9.04 nm
Rms spotsize at the CP	σ_x^c/σ_y^c =718./90.9 nm
Rms angular divergence	σ_x'/σ_y' = 143./18.1μrad
Rms bunch length	$\sigma_z = 0.1$ mm
Polarization	Fully polarized with helicity switching capability
Collision scheme	Vertical offset or sweeping magnet
CP–IP distance	b=5 mm
Crossing angle	$\phi_c \leq 30$ mr

Table B-2. *Electron beam parameters for a reference design at $E_{CM} = 500$ GeV*

The design goal for the FFS for the $\gamma\gamma$ collision is $\beta_x^* = \beta_y^* = 0.5$ mm. Note that, contrary to the e^+e^- case, there are no constraints on the beam profile at the IP arising from beamstrahlung effects.

The large crossing angle, 30 mr, is necessary in the collision scheme without a sweeping magnet, due to the large disruption of the low-energy electrons (coming from the high-order multiple scattering in the CP). The disruption is smaller when a sweeping magnet is employed.

A more detailed considerations leading to the parameters in Table B-2 are given in Section B.5.

B.4 CP Issues

B.4.1 Optimization of the Laser Parameters

Compton scattering of laser beam by relativistic electron beams is an efficient way to generate gamma-ray photons [Arutyunian 1963]. A review of the relevant kinematics can be found in [Telnov 1990].

The energy of the Compton-scattered photon is maximum when the scattered photon is in the direction of the incoming electron, *i.e.,* in the backscattering direction. The maximum energy is given by

$$\omega_{max} = \frac{x}{x+1} E_0, \tag{B.6}$$

where

$$x = \frac{4E_0\hbar\omega_0}{m^2c^4} \simeq 15.3 \left[\frac{E_0}{TeV}\right]\left[\frac{\hbar\omega_0}{eV}\right] \quad . \tag{B.7}$$

Here ω_0 is the laser frequency and E_0 is the initial energy of electrons. Hence, the energy of the backscattered photon increases with increasing value of the parameter x, but if x is larger than 4.8, high-energy photons

can be lost due to e^+e^- pair creation in collision with unscattered laser photons (Breit-Wheeler process). Thus, the optimum value is $x = 4.8$, corresponding to the maximum photon energy $\omega_{max} = 0.81E_0$. For $E_0 = 0.25$ TeV, this leads to a laser wavelength of about 1 μm. Thus it is convenient to choose the wavelength of Nd:Glass laser, 1.05 μm.

Neglecting multiple scattering, and assuming that the laser profile seen by each electron is the same, the "conversion" probability of generating high-energy gamma photons per individual electron can be written as

$$n_\gamma = 1 - \exp(-q) \quad . \tag{B.8}$$

If the laser intensity along the axis is uniform

$$q = \sigma_c \frac{N_L}{\Sigma} = \frac{\sigma_c A}{\hbar\omega_o \Sigma} = \frac{\sigma_c I \tau_L}{\hbar\omega_0} \quad . \tag{B.9}$$

Here σ_c is the Compton cross section, which for $x = 4.8$ is $1.75 \times 10^{-25}/cm^2$, N_L is the number of the laser photons, Σ is the transverse area of the laser spot, A is the the laser pulse energy, I is the laser intensity (power per unit area), and τ_L is the laser pulse length. The pulse energy corresponding to $q = 1$, *i.e.,* a conversion probability of 65%, is given by $A_0 = \hbar\omega_0\Sigma/\sigma_c \approx \hbar\pi c Z_R/\sigma_c$. The increase in the conversion probability with a laser pulse energy larger than A_0 is relatively small, and, furthermore, is expensive due to higher laser power requirements. Therefore we should choose $A \sim A_0$, *i.e.,* $q \sim 1$. Thus the pulse energy is minimized when the laser spot is focused tightly to match the electron pulse shape. However, the focusing may not be made arbitrarily strong: the laser intensity I could become so large that nonlinear QED effects may spoil the conversion process.

The nonlinear effect is characterized by the quantity

$$\eta = \frac{eE}{\omega_0 mc}, \ \eta^2 = 0.4 \left[\frac{I}{10^{18}\mathrm{W/cm}^2}\right] \left[\frac{\lambda}{1.054\mu\mathrm{m}}\right]^2 \tag{B.10}$$

When $\eta^2 \gtrsim 1$, two or more laser photons can be scattered at the same time. The the maximum energy of the backscattered high energy photon in the non-linear Compton scattering involving n laser photons is given by

$$\omega^n_{max} = \frac{nx}{1 + \eta^2 + nx} E_0 \quad . \tag{B.11}$$

For $n = 1$, which corresponds to the single photon process, the maximum photon energy is smaller than that given by the linear approximation, Eq. B.6. This is not desirable since the $n = 1$ photons are usually the most useful ones. Another effect, which is essentially quantum mechanical, is that the pair production can now proceed via multiphoton scattering with a gamma-ray photon, leading to a depletion of the gamma-ray flux. In this design the laser intensity I is kept below 1×10^{18} W/cm^2.

A formula for the conversion efficiency n_γ, neglecting the nonlinear effect and multiple scattering, but taking into account the fact that different electrons see different laser profiles during the interaction, is derived in Section B.4.3. Given the laser pulse energy A and the intensity I, Eq. B.21 can be used to find the optimum value of Z_R and σ_{Lz} corresponding to the maximum conversion efficiency. The case for $A = 1$ J, $I = 1 \times 10^{18}$ W/cm^2, and the rms electron pulse length $\sigma_z = 0.1$ mm is shown in Figure B-3. It is seen that a maximum conversion efficiency $n_\gamma = 0.68$ can be achieved with $Z_R = 0.1$ mm. The corresponding laser pulse length (rms) is $\sigma_{Lz} = 0.23$ mm(which is larger than σ_z for the electrons).

The peak power corresponding to $A = 1$ J and pulse length $\tau \sim 2\sigma_{Lz}/c \simeq 1.8$ ps is about 0.5 TW. With the NLC pulse format of 90 micropulses repeated at 180 Hz, the required average laser power is 16.2 kW, which

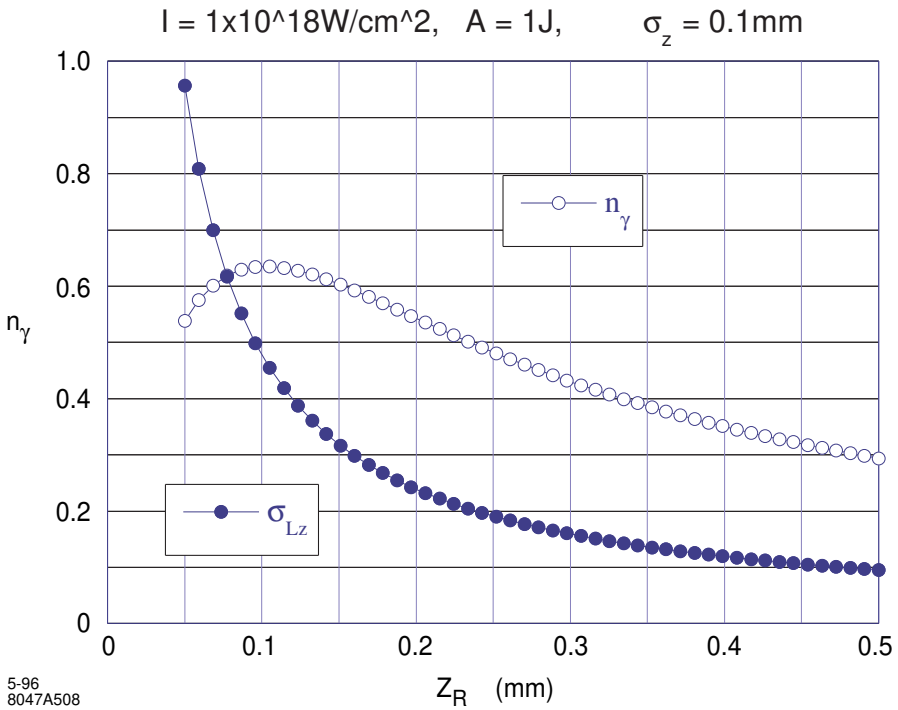

Figure B-3. *Compton Conversion efficiency as a function of z_r at fixed A and I.*

is rather high. The power can be reduced significantly if laser pulses can be reused by multipass optics or by storing the laser energy in an optical cavity.

With the laser intensity $I = 1\times10^{18} W/\text{ cm}^2$, the nonlinear effect is not negligible as we will see in Section B.6. To study the dependence of the conversion efficiency on A and I, we show in Figure B-4 the maximum conversion efficiency as a function of the laser pulse energy and the laser intensity. Figure B-5 and B-6 give respectively the corresponding Rayleigh length and the rms laser pulse length. Figure B-7 gives the contour line corresponding to the conversion efficiency $\eta_\gamma = 0.65$, showing that as the intensity is reduced the pulse energy must be increased to maintain the same conversion efficiency. As an example, with $A = 2$J and $I = 5\times10^{17} W/\text{ cm}^2$, one can obtain the maximum conversion efficiency $n_\gamma = 0.648$ with $Z_R = 0.201$ mm and $\sigma_{LZ} = 0.46$ mm. Another example is $A = 3J$ and $I = 3.3\times10^{17} W/\text{ cm}^2$ for which $n_\gamma = 0.65$, $Z_R = 0.347$ mm and $\sigma_{LZ} = 0.76$ mm. The non-linear effects in this case are smaller than the $A = 1J$, $I = 1\times10^{18} W/\text{ cm}^2$ example, but the pulse energy is higher. Since the laser power is expensive, we will adopt in this report $A = 1$J, $I = 1\times^{18} W/\text{ cm}^2$ as the reference case.

Transverse coherence of the laser beam is important in obtaining a diffraction-limited focal spot. Versatile polarization control is also important; the helicity of the laser light should be opposite to that of the electron beam to obtain a higher conversion rate and the γ photon spectrum peaked around ω_m. Controlling the γ photon polarization by controlling the laser photon polarization is an important technique for many $\gamma\gamma$ or γe^- experiments [Barklow 1990]. Switching of helicity is proposed to characterize all helicity components of the luminosities [Telnov 1995].

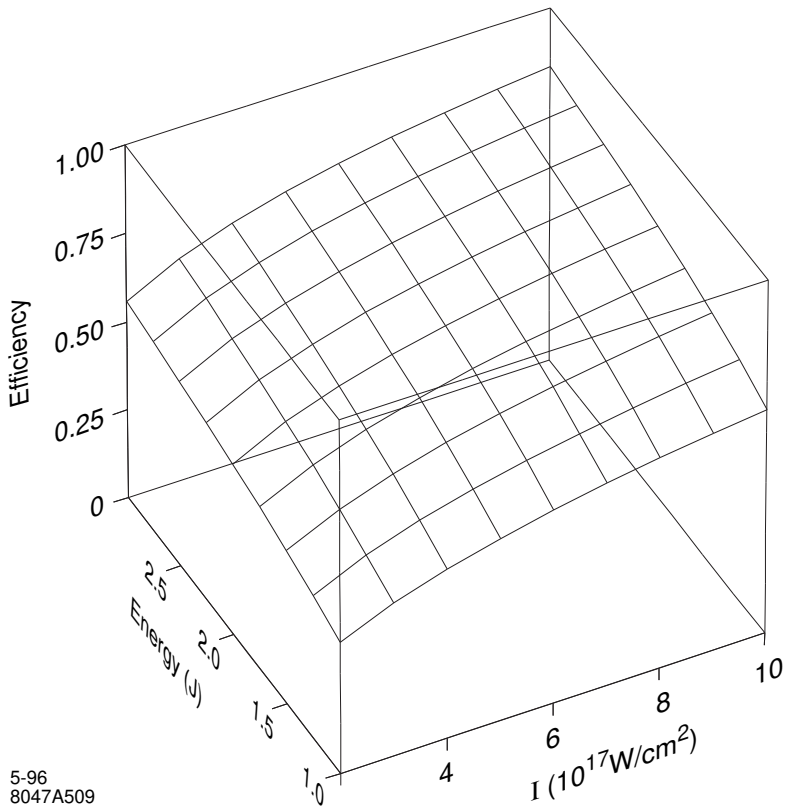

Figure B-4. *Optimized conversion efficiency as a function of pulse energy A and pulse intensity I.*

B.4.2 Low-Energy Electrons Due to High-Order Multiple Scattering

With the intense laser pulse required for an efficient conversion, the probability of multiple scattering is high, giving rise to soft electrons and photons. The multiple scattering process is roughly described by the Poisson distribution. A k-fold scattering has the probability

$$P_k \sim \frac{q^k e^{-q}}{k!} \quad , \tag{B.12}$$

and gives rise to a minimum electron energy E^k where [Telnov 1990]

$$E^k \sim \frac{E_0(1+\eta^2)}{1+\eta^2+kx} \quad . \tag{B.13}$$

For ten-fold multiple scattering, $k = 10$, the electron energy is about 2% of the incoming energy. There are about 1000 such particles, which could cause significant background signals if they are allowed to hit the quadrupole faces.

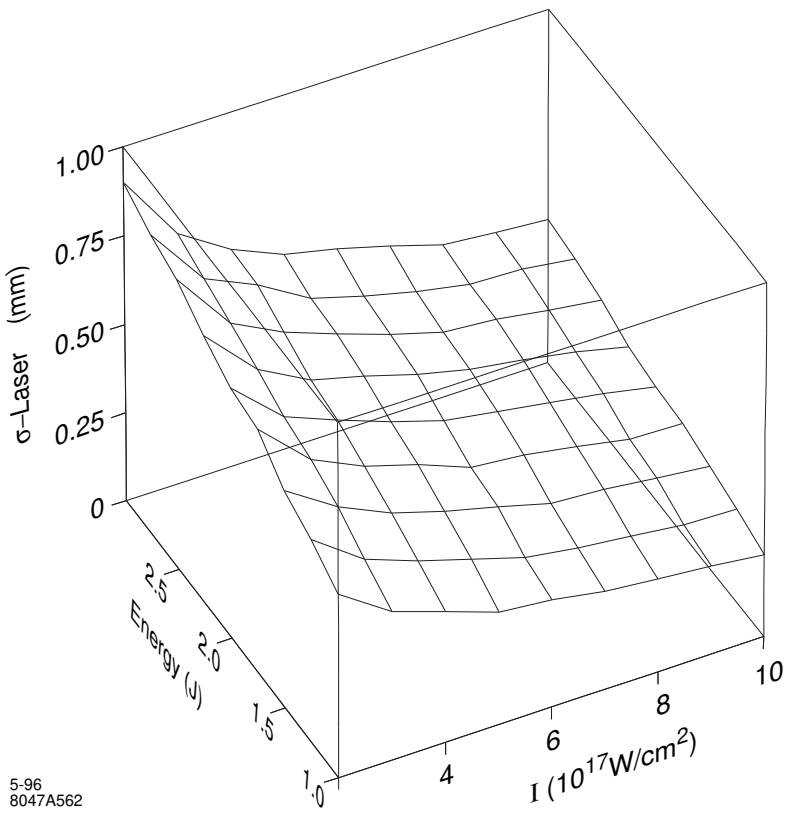

Figure B-5. *Optical pulse length corresponding to the optimized conversion efficiency.*

B.4.3 Compton Conversion Efficiency

Let an electron beam collide with a laser beam of density $n_L(\mathbf{x}, t)$. The density of the electron beam will be written as $n_e(\mathbf{x} - \mathbf{v}t, t)$ to indicate that the beam moves with velocity $\mathbf{v}$. The number of scatterings in the space-time element $d\mathbf{x}dt = d\mathbf{x}'dt$, where $\mathbf{x}' = \mathbf{x} - \mathbf{v}t$ is given by [Landau 1987]

$$d\nu = \sigma_c v_{rel} n_e(\mathbf{x}', t) n_L(\mathbf{x}, t) d\mathbf{x}' dt \quad . \tag{B.14}$$

Here σ_c is the Compton cross section, $v_{rel} = \sqrt{(\mathbf{v} - \mathbf{v}_L)^2 - (\mathbf{v} \times \mathbf{v}_L)^2}$ is the relative velocity, $\mathbf{v}_L = c\mathbf{n}$, and $\mathbf{n}$ is the direction of the laser propagation. Since we are interested in the case where the loss of the laser photons can be neglected, we may assume that the scattering does not change $n_L(\mathbf{x}, t)$. On the other hand, the probability of Compton scattering per electron is large, and the electron after producing a γ photon after scattering may be regarded as lost. The rate of the loss is given by Eq. B.14 and can be written as follows:

$$-dn_e(\mathbf{x}', t) d\mathbf{x}' = v_{rel} \sigma_c n_e(\mathbf{x}', t) n_L(\mathbf{x}' + \mathbf{v}t, t) d\mathbf{x}' dt \quad . \tag{B.15}$$

From this, we derive

$$\frac{\partial}{\partial t} n_e(\mathbf{x}', t) = v_{rel} \sigma_c n_e(\mathbf{x}', t) n_L(\mathbf{x}' + \mathbf{v}t, t) \quad . \tag{B.16}$$

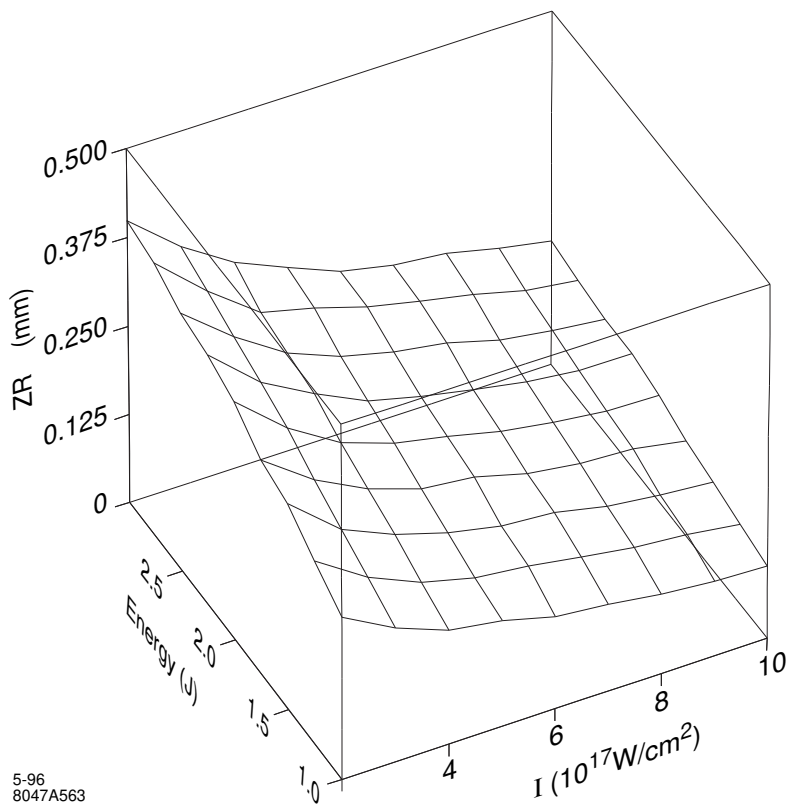

Figure B-6. *Rayleigh length corresponding to the optimized conversion efficiency.*

The solution of Eq. B.16 is

$$n_e(\mathbf{x}',t) = n_e^i(\mathbf{x}') \exp\left[-\int_{-\infty}^{t} v_{rel}\sigma_c n_L(\mathbf{x}'+\mathbf{v}t',t')dt'\right] \quad . \tag{B.17}$$

Here $n_e^i(\mathbf{x}')$ is the initial electron distribution. The total number of the γ photons generated is obtained by integrating the above equation:

$$N_\gamma = \int d\mathbf{x}' n_e^i(\mathbf{x}') \left(1 - \exp\left[-\int_{-\infty}^{\infty} v_{rel}\sigma_c n_L(\mathbf{x}'+\mathbf{v}t',t')dt'\right]\right) \quad . \tag{B.18}$$

The transverse dimension of the electron beam is usually much smaller than that of the laser beam. For an electron beam traveling at an angle θ with respect to the z-axis, we have $x' = x + ct\sin\theta$, $y' = y$, and $z' = z - ct\cos\theta$. The initial electron density can be written as

$$n_e^i(\mathbf{x}') = \frac{N_e}{\sqrt{2\pi}\sigma_z}\delta(x')\delta(y')\exp(-z'^2/2\sigma_z^2) \quad . \tag{B.19}$$

Here N_e is the total number of electrons in the bunch, and σ_z is the rms bunch length. The laser pulse propagating along the negative z-direction can be written as

$$n_L(x,y,z,t) = \frac{N_L}{(2\pi)^{3/2}\sigma_{Lz}} \frac{\exp\left(-\frac{1}{2}\left[\frac{x^2+y^2}{\sigma_{Lx}(z)^2} + \frac{(z+ct)^2}{\sigma_{Lz}^2}\right]\right)}{\sigma_{Lx}(z)^2} \quad . \tag{B.20}$$

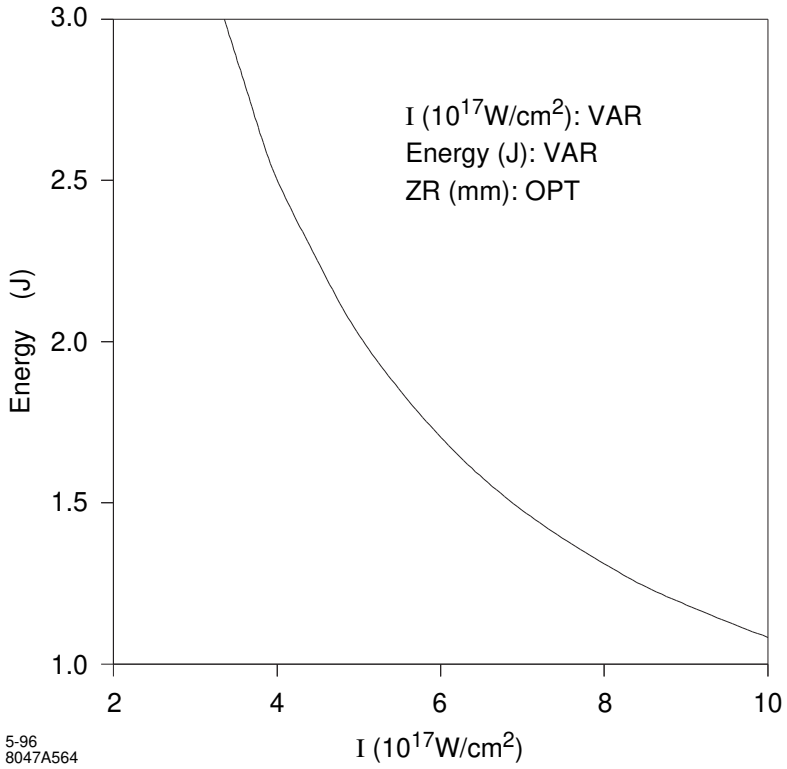

Figure B-7. *Optical pulse energy versus intensity at conversion efficiency = 0.65.*

Here N_L is the number of the laser photons in the pulse, σ_{Lz} is the rms length, $\sigma_{Lx}(z)^2 = \sigma_{Lx}^{*2}(1+(z/Z_R)^2)$, σ_{Lx}^* is the rms spotsize, and Z_R is the Rayleigh length. The last two quantities are related by $\sigma_{Lx}^{*2} = Z_R\lambda/4\pi$, where λ is the laser wavelength.

In the special case of head-on collision, $\theta = 0$, and one derives from the above formulas the result

$$n_\gamma \equiv \frac{N_\gamma}{N_e} = 1 - \frac{1}{\sqrt{2\pi}\sigma_z}\int dz \exp\left(-\frac{z^2}{2\sigma_z^2} - U(z)\right) \tag{B.21}$$

where

$$U(z) = \frac{4\sigma_c N_L}{\sqrt{2\pi}\lambda Z_R \sigma_{Lz}}\int ds \frac{\exp\left[-\frac{2(s-z/2)^2}{\sigma_{Lz}^2}\right]}{1+s^2/Z_R^2} \quad . \tag{B.22}$$

The spectrum of the photons is given by

$$\frac{dn_\gamma}{dy} = n_\gamma \frac{1}{\sigma_c}\frac{d\sigma_c}{dy} \tag{B.23}$$

where $y = \hbar\omega/E_o$, and $d\sigma_c/dy$ is the differential scattering cross section of the Compton process, given, for example, by Eq. 3 of Ref. [Telnov 1995].

Although we have neglected the multiple scatterings in the derivation here, Eq. B.23 is expected to be valid near $y \sim y_{max} = x/(1+x)$ even for a "thick" target. On the other hand, the effect of multiple scattering will be large in the soft photon region, $y \sim 0$.

B.5 IP Issues

B.5.1 Optimization of Spectral Luminosity

The total $\gamma\gamma$ luminosity is approximately given by $n_\gamma^2 \simeq 0.4$ times the geometric e^-e^- luminosity (with zero offset). However, the spectral luminosity of the $\gamma\gamma$ collision depends strongly on the distance b between the CP and the IP. This is because the energy of the gamma photon depends sensitively on the scattering angle, being maximum in the original electron direction and decreasing rapidly away from this direction. Introducing the parameter $\rho = b/\gamma\sigma_y^*$, where σ_y^* is the vertical rms electron beam size (assumed to be smaller than the horizontal size) in the absence of the CP, the spectral luminosity is broadly distributed as a function of the c.m. energy of the two-photon system when $\rho \ll 1$. As ρ is increased, the low-energy part of the luminosity spectrum becomes suppressed due to the larger spotsize occupied by low-energy photons. Thus, the luminosity spectrum develops a well defined peak at the high-energy end with a bandwidth of about 20% when $\rho \geq 1$. This region is also characterized by a high degree of polarization. For most applications, one would choose $\rho \simeq 1$ to obtain a narrow spectrum without suffering a large luminosity reduction. In our case, this corresponds to $b \sim 5\,\mathrm{mm}$. The spectral peak at the high-energy end of the invariant mass distribution accounts for about 20% of the total $\gamma\gamma$ luminosity, or about 10% of the geometrical e^-e^- luminosity.

For e^+e^- collisions, the beam spot at the IP is normally designed to be flat to minimize the beamstrahlung effect. In $\gamma\gamma$ collisions, the vertical beam size, which is determined by the condition $\rho \simeq 1$, is larger than that in the e^+e^- collisions for a reasonable value of the CP-IP distance b. The horizontal spotsize should be reduced in proportion to achieve a comparable luminosity. Thus the FFS for $\gamma\gamma$ collision must provide a value of β_x^* which is smaller and β_y^* which is larger than the corresponding values for the e^+e^- design. With $\beta_x^* = \beta_y^* = 1\,\mathrm{mm}$, the geometric luminosity would be the same as in the case of the e^+e^- collision. We therefore aim for $\beta_x^* = \beta_y^* = 0.5\,\mathrm{mm}$ for the $\gamma\gamma$ collision. In doing so, a proper account should be made of the Oide effect as well as the constraint that β_x and β_y be larger than the bunch length. A design of the FFS similar to that of the e^+e^- case, but with final quadrupoles reversed in x and y is presented in Section B.9.

B.5.2 Polarization

By varying the polarization of the electron and the laser beams, the polarization of the high-energy photon beams can be tailored to fit the needs of the individual experiment. Controlling the polarization is also important in sharpening the spectral peak in the $\gamma\gamma$ luminosity. Due to the polarization dependence of the Compton scattering, the spectral peak present in the case of $\rho \geq 1$ is significantly enhanced by choosing the helicity of the laser photons to be of the opposite sign to the helicity of the electrons.

B.5.3 Collision of the Spent Electron Beam

The background due to γe^- and e^-e^- collisions as well as the collision of the beamstrahlung photons is large if the spent electron beams are allowed to collide at the IP. The collisions of these particles would also produce positrons and minijets. These unwanted collisions give rise to the background events. Whether these backgrounds pose a significant problem will depend on the nature of the particular experiment, and can only be evaluated after detailed detector simulation.

Among the background events, the γe^- collisions appear to be the most significant, with a luminosity roughly equal to the $\gamma\gamma$ luminosity. The ee luminosity due to the collision of the "spent" electrons (*i.e.,* after Compton conversion) is suppressed significantly (by a factor of 5) due to the fact that the spectrum of the spent electron is broad, leading to a large disruption at the IP.

A way to avoid the collision of the electron beams would be to sweep the spent electrons away from the IP by an external magnetic field. The magnetic field should extend longitudinally to about 1 cm with a strength of about T. Such a magnet could in principle be designed either with a superconducting [Telnov 1990] or with a pulsed conductor [Silvestrov un]. Installing the sweeping magnet to the tight space in the interaction region with a minimum obstruction to the detector is a major challenge.

A plasma lens to overfocus the spent electron beam has also been proposed [Rajagopalan 1994]. This scheme must inject gases to produce plasma and also remove them from the interaction region. Another proposal is to arrange the electron beams to repel and miss each other entirely in "a heads-up" collision [Balakin 1994]. For this scheme to work, the electron beam intensity needs to be much higher than that contemplated in most linear collider proposals. We have not studied these options in detail in this study.

B.5.4 Disruption of Low Energy Electrons

A characteristic angle for the full-energy primary, disrupted electrons is [Hollebeek 1981]:

$$\theta_d \equiv \frac{2Nr_e}{\gamma\sigma_x} \quad . \tag{B.24}$$

Thus the main fraction of the electrons after the IP will be deflected into an angular cone given by θ_d in which γ is replaced by an average value. However, Eq. B.24 is valid only when the deflection angle is smaller than $4\sigma_x/\sigma_z$ (we assume $\sigma_x \ll \sigma_z$). For very low energy electrons for which $\theta_d\gamma e^-\sigma_x/\sigma_z$, the deflection angle is given by [Telnov 1990]

$$\theta \sim \sqrt{\frac{4\pi N r_e}{\gamma\sigma_z}} \quad . \tag{B.25}$$

Low-energy electrons are generated by high-order multiple scattering at the CP, as discussed in Section B.4.2. For our parameters, a ten-fold or higher multiple scattering generates about one thousand electrons with energy as low as 2–3% of their initial energy . These particles will be deflected up to an angle of about 10 mr due to collision with the opposing electron beam. Since there are about 1000 such particles, which will contribute to the background signals if they are allowed to hit the quadrupole faces, the crossing angle should be larger than 10 mr plus an additional angle to clear the quadrupole faces closest to the IP. In the case of e^+e^- collisions, the quadrupole clearance is taken to be 20 mr. We therefore take the crossing angle for the $\gamma\gamma$ collision to be 30 mr. Crabbing the electron beam is essential for a $\gamma\gamma$ collider. The effect of the solenoidal field on beam collisions with a large crossing angle also needs to be studied.

B.6 Luminosity Calculations

B.6.1 Simulation Code Development

The physical processes occurring in the CP and the IP are complex and diverse, including linear and nonlinear, single and multiple Compton scattering at the CP, beamstrahlung, coherent and incoherent pair production, Bethe-Heitler and Landau Lifshitz processes at the IP. A reliable prediction of the $\gamma\gamma$ and γe^- luminosities and the backgrounds can only be done with a numerical code simulating the entire complex of CP and IP physics. It is desirable that several independent codes are available so that simulation results can be cross-checked. At the same time, simple analytical estimates for the relative importance of these processes are also highly desirable.

Ideally code for a full simulation of $\gamma\gamma$ or γe^- collisions must incorporate the following features [Chen 1995a]:

- The CP physics:
  - Linear and nonlinear Compton scattering: $e^\pm + laser \to e^\pm + \gamma$.
  - Linear and nonlinear Breit-Wheeler scattering: $\gamma + laser \to e^+e^-$.
- Beam propagation from the CP to IP including the effects of external magnetic fields (solenoidal field, sweeping magnet) and plasma lens (if any).
- The IP Physics:
  - Disruption effects; interaction of $e^\pm$ with the field of the opposing beam.
  - Beamstrahlung and coherent pair production via interaction of γ and $e^\pm$ with the collective field the opposing beam.
  - Incoherent processes (Bremsstrahlung: $ee \to ee\gamma$; Breit-Wheeler: $\gamma\gamma \to e^+e^-$; Bethe-Heitler: $e\gamma \to ee^+e^-$; Landau-Lifshitz: $ee \to eee^+e^-$).
- Beam propagation from the IP to the exit line.

The ABEL code (Analysis of Beam-beam Effects in Linear colliders) simulates the beam-beam interaction including disruption and beamstrahlung effects [Yokoya, 1986]. The code has been subsequently modified to include incoherent pair creation in the equivalent photon approximation (ABELMOD) [Tauchi 1993]. These codes were originally written for e^+e^- collisions but have been modified to simulate the e^-e^- collisions.

There are several Monte-Carlo codes for simulating the Compton conversion process: A code written by Horton-Smith [Horton-Smith phd] in connection with the E-144 experiment at SLAC, which takes into account the non-linear effect fully but is only applicable for unpolarized electrons; a code written by Ohgaki and Yokoya [Ohgaki 1995], which is based on the Compton scattering in linear approximation but is applicable for arbitrary electron and photon polarizations; a code by Telnov [Telnov 1995], which is similar to the previous one with the further approximation that all electrons see the same laser profile ("same-profile" approximation); a code recently written by Yokoya [Yokoya 1996], which takes into account the non-linearity of the Compton scattering, and can handle circularly polarized electrons.

The codes for the IP and the CP are being combined to a varying degree of sophistication to calculate the $\gamma\gamma$ and γe^- luminosities. In our preliminary calculation, we have used Telnov's code extensively, which

includes the multiple Compton scattering effects in linear Compton approximation and the same-profile approximation at the CP, deflection by external magnetic field and synchrotron radiation in the region between the CP and the IP, the beamstrahlung and the coherent pair production at the IP. A similar code has been assembled by Takahashi [Takahashi 1996] based on Ohgaki's Compton conversion package and ABEL. A more refined code incorporating Yokoya's non-linear Compton conversion and the ABEL-MOD is being assembled as a collaborative effort between Hiroshima University, KEK, SLAC and LBL. This code is referred to as CAIN 1.1. Recently, Yokoya has written a new code, named CAIN 2.0, which does not share any subroutines with ABEL [Yokoya 1996].

A simpler code (named BERT) aimed at a careful study of the transport and disruption of the two opposing electron beams with arbitrary initial energy distributions is being developed by W. Fawley. Such a code will be useful, for example, in evaluating the heads-up collision scheme [Balakin 1994] to suppress e^-e^- collisions at the the IP. The results from these codes have been cross-checked where applicable, and are found to be in reasonable agreement with each other.

B.6.2 Simulation of the CP

Figure B-8 gives the γ-photon spectrum after the CP, using the electron beam parameters in Section B.3, and the laser parameters in Section B.4. They are obtained using the code written by Yokoya [Yokoya 1996]. The top, middle and the bottom graphs correspond respectively to the case $A = 3J$, $I = 3.3 \times 10^{17}$ W/ cm^2, the case $A = 2J$, $I = 5 \times 10^{17}$ W/ cm^2, and the case $A = 1J$, $I = 10^{18}$ W/ cm^2, For the top graph, the non-linearity is small, and the spectrum near the maximum photon energy agrees well with the theoretical formula, Eq. B.23. The non-linearity is visible but not pronounced for the middle graph. For the bottom graph however, the smearing of the spectral peak at the high-energy end of the photon is clearly seen.

B.6.3 Telnov's Simulation Results for $\gamma\gamma$, γe^- and e^-e^- Luminosities

This section summarizes the results of simulation calculations using Telnov's code. As discussed in the above, the code is valid under two assumptions: First, the laser profiles seen by all electrons are the same, and second, the non-linear effect can be neglected. The error introduced by the first assumption appears to be not significant in our parameter regime. The validity of the second assumption depends on the laser intensity as discussed in Section B.6.2: The non-linearity is negligible for the case $A = 3$ J, $I = 3.3 \times 10^{17} W/cm^2$, and significant for the case $A = 1J, I = 1 \times 10^{18} W/$ cm^2. Although the second case is adopted as the baseline design in this report, we use Telnov's simulation code in this section because it is the code currently fully debugged. The result of Telnov's simulation appears to be in general agreement with that calculated by Takahashi using the linear version of CAIN-1.

Table B-3 summarizes the main results. Here z = invariant mass of the colliding system/$2E_0$, where E_0 is the energy of the incoming electrons. The case (a) to (f) are for the collisions at various vertical offset Δy without the sweeping magnet. The case (d) is the same as (c) but suppressing the beamstrahlung at the IP. In the case (g), there is a 1-T sweeping magnet. The electron and the laser parameters are those given in Section B.3 and B.4, respectively. However, the distance between the CP and the IP is taken to be 7.8 mm for case (g), while it is 5 mm for all other cases.

Even without a sweeping magnet, the e^-e^- luminosity is significantly reduced, a factor of five already at a small offset, $\Delta y = 0.2\sigma_y$, and the reduction increases slowly as a function of the offset. The $\gamma\gamma$ luminosity

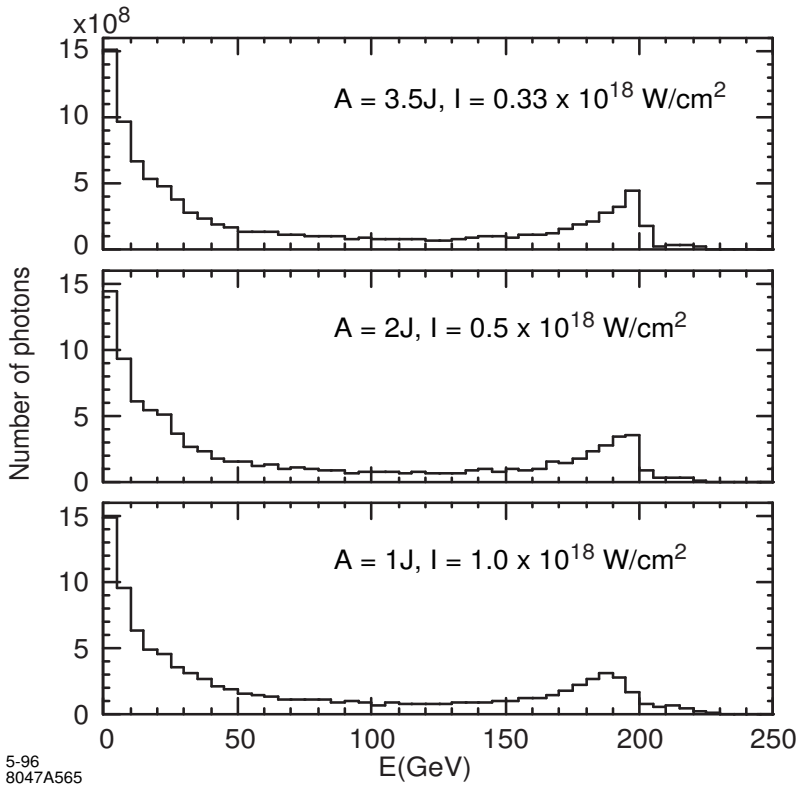

Figure B-8. *Spectrum of the γ-photons after the CP at different pulse energies and intensities.*

and γe^- luminosity are roughly equal to the geometric luminosity up to $\Delta y \approx 1\sigma_y$. The $\gamma\gamma$ luminosity at high energy end, $z > 0.65$, is about 10% of the geometric luminosity. A significant fraction of the total $\gamma\gamma$ luminosity is therefore in the low-energy region, and arises from the collisions of the beamstrahlung photons generated at the IP by the interaction of the spent electron beams. The low-energy $\gamma\gamma$ luminosity, as well as the γe^- luminosity, would pose a significant background problem in the collision scheme without the sweeping magnet.

From the table, it is apparent that the luminosity distributions are not a very sensitive function of the offset Δ_y. The $\gamma\gamma$ luminosity at high energy end ($z \geq 0.65$) is practically constant. The ee luminosity becomes smaller by a factor of 2 from $\Delta y = 0.25\sigma_y$ to $\Delta y = 1\sigma_y$. However the ee luminosity is already smaller than the γe^- luminosity by about a factor of five. Therefore the tolerance on Δy is rather relaxed; Δy up to about $1\sigma_y$ does not degrade the collision performance.

The column (g) in the table gives the result when a sweeping magnet is employed. Note that the high-energy $\gamma\gamma$ luminosity is about the same as before, but the background from the low-energy $\gamma\gamma$ or γe^- luminosities are significantly reduced.

The table also shows that the disruption angle for the low-energy particle ($E_{\min} = 3$ GeV) is ± 8 mr for collisions without a sweeping magnet. The low-energy particles are generated through multiple scattering at the CP. Analytical estimate shows that a ten-fold multiple scattering will generate of the order of one thousand particles with an energy of 2–3% of the initial electron energy (corresponding to about 5 GeV in

	(a)	(b)	(c)	(d)	(e)	(f)	(g)
$L_{ee}/L_{\rm geom}$	0.2	0.19	0.15	0.16	0.12	0.096	0
$L_{ee}(z>0.65)/L_{\rm geom}$	0.12	0.114	0.086	0.091	0.064	0.046	0
$L_{\gamma e^-}/L_{\rm geom}$	1.12	1.04	0.93	0.52	0.79	0.706	0.1
$L_{\gamma e^-}(z>0.65)/L_{\rm geom}$	0.26	0.24	0.2	0.22	0.18	0.143	0.017
$L_{\gamma\gamma}/L_{\rm geom}$	1.23	1.22	1.16	0.38	1.08	1.05	0.37
$L_{\gamma\gamma}(z>0.65)/L_{\rm geom}$	0.116	0.112	0.105	0.104	0.103	0.098	0.09
$L_{\gamma\gamma}(z>0.75)/L_{\rm geom}$	0.057	0.0545	0.0514	0.051	0.05	0.046	0.051
$\theta_{y,\rm max}$ (mr)	8	8	8	8	8	8	2.5
$E_{\rm min}$	3	3	3	3	3	3	3

[a] No magnet deflection, $\Delta_y = 0.25\sigma_y$
[b] " " " , $\Delta_y = 0.5\sigma_y$
[c] " " " , $\Delta_y = 0.75\sigma_y$
[d] " " " , $\Delta_y = 0.75\sigma_y$ without beamstrahlung
[e] " " " , $\Delta_y = 1\sigma_y$
[f] " " " , $\Delta_y = 1.25\sigma_y$
[g] With magnet deflection, $b = 0.78$ cm, $B = 10$ kGauss

Table B-3. *Luminosities in $\gamma\gamma$ collision (V. Telnov).*

the present case). These are deflected to an angular cone of about 10 mr. This implies that the crossing angle should be larger than 20 mr. The exit beam pipe must be designed to accept these particles to avoid the background events.

For the case (g) with a sweeping magnet, the disruption of the 3-GeV particle is much smaller, about 3 mr.

Figures B-9–B-11 give a more detailed picture for the collision with the vertical offset $\Delta y = 0.75\sigma_y$. Figure B-9 gives the luminosity distributions for $\gamma\gamma$, γe^-, and ee collisions. Figure B-10 gives the $\gamma\gamma$ luminosities, where the solid curve is the same as in Figure B-9 and the dashed curve is for the case where the beamstrahlung contribution is suppressed. Figure B-11 gives the energy distribution of the final electrons.

Figure B-12 shows that the $\gamma\gamma$ luminosities for different offsets between $0.25\sigma_y \le \Delta y \le 1.25\sigma_y$ are more or less the same with each other. Figure B-13 shows the distribution in the vertical angle of the disrupted electron beams at various separations. The shape of the angular disruption may be used to calibrate the offset distance experimentally.

Finally, Figure B-14 shows the luminosity distributions for the case where a sweeping magnet is used (the case (g) in Table B-3). The γe^- luminosity is significantly reduced, and the ee luminosity is entirely suppressed.

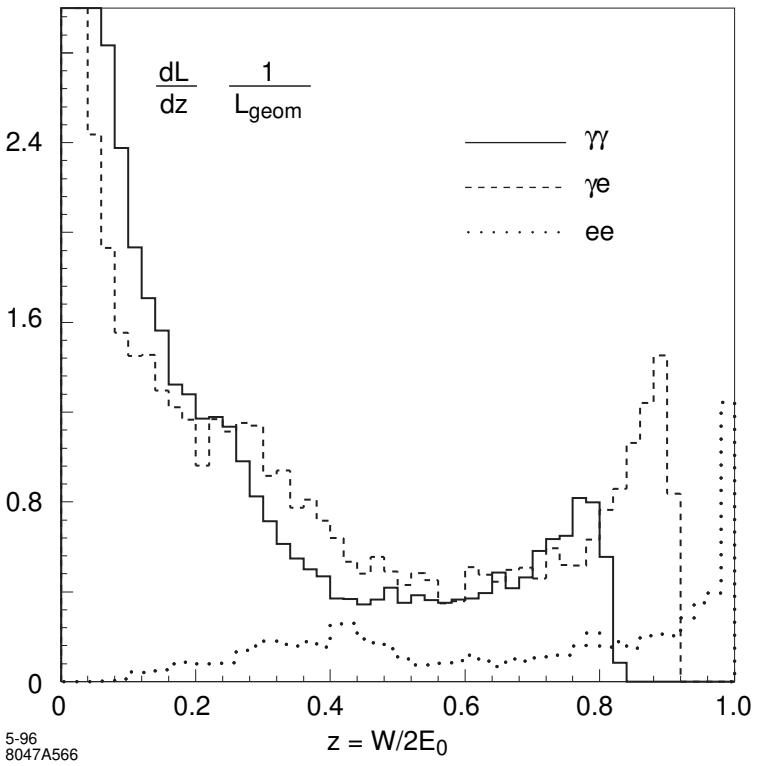

Figure B-9. *Luminosity distributions with $\Delta y = 0.75\sigma_y$ and no sweeping magnet.*

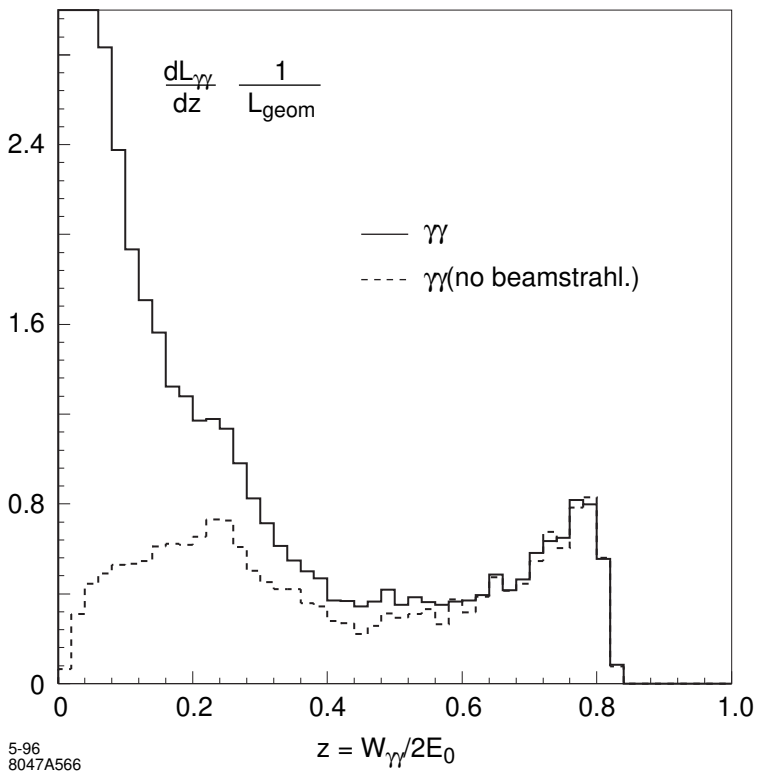

Figure B-10. *$\gamma\gamma$ luminosity for $\Delta y = 0.75\sigma_y$ and no sweeping magnet.*

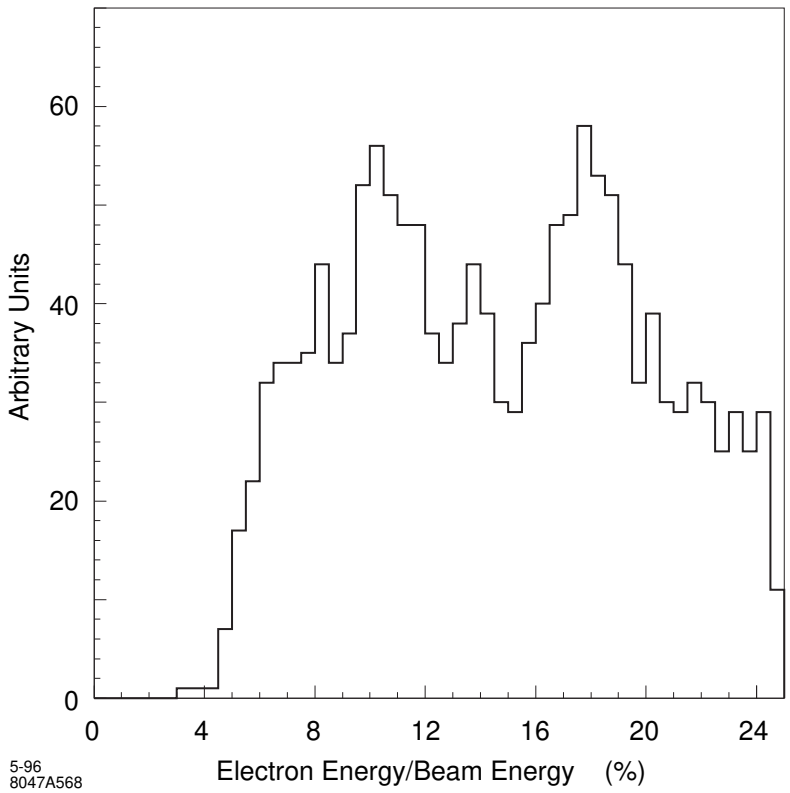

Figure B-11. *Energy distribution of final electrons for $\Delta y = 0.75\sigma_y$, no sweeping magnet.*

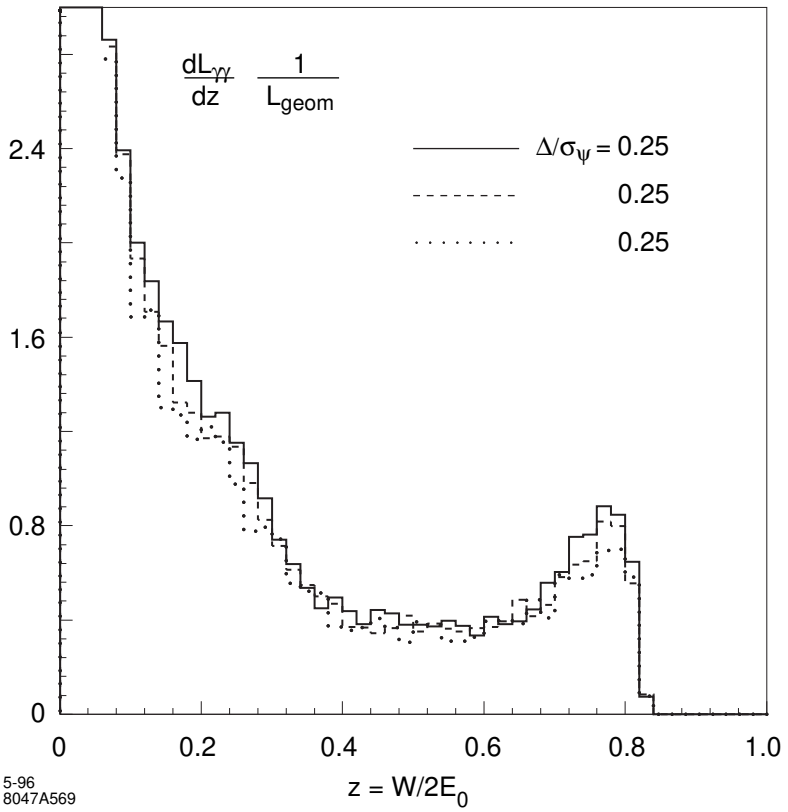

Figure B-12. *$\gamma\gamma$ luminosity distribution for various vertical separations, and no sweeping magnet.*

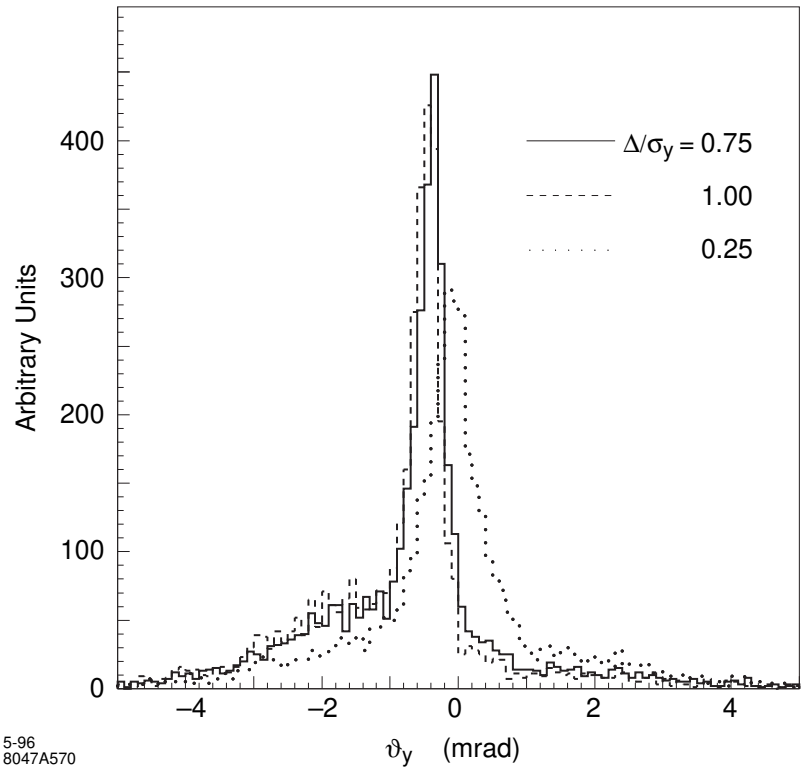

Figure B-13. *Distributions as a function of vertical angle for various vertical offset, and no sweeping magnet.*

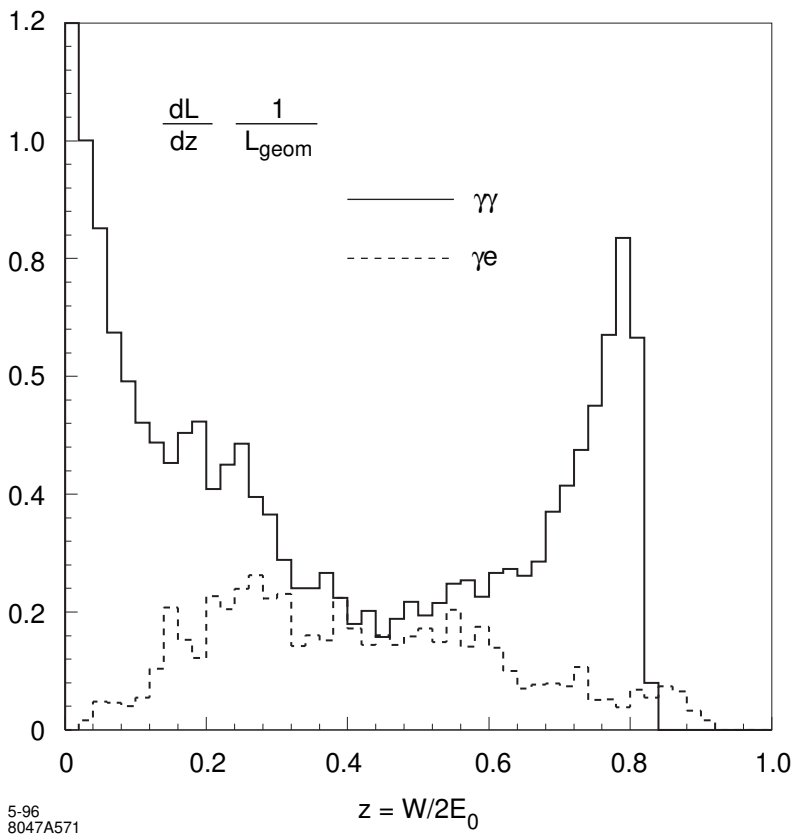

Figure B-14. *Luminosity distributions with magnetic deflection ($b = 0.78\ cm$, $B = 1\ T$).*

B.7 Backgrounds and Other Detector Considerations

B.7.1 Introduction

For the planned $\gamma\gamma$ physics program in IR2, the incoming polarized electron beams will be converted by an intense laser beam into hard photon beams. As a matter of routine operation in monitoring the incoming electron beam parameters, one or both of the beams will be left unconverted thus allowing high-luminosity studies of γe^- and e^-e^- collisions with the same detector. Given that the electron-photon CP will be located only a few millimeters from the IP, the resulting spent-electron beam background presents a significant challenge to the detector design for these interactions.

It is expected that the physics design criteria for the detector will be basically the same as those for the e^+e^- detector in IR1. Comprehensive, full solid-angle detectors are required to fully exploit the broad physics programs envisioned for both IRs, and the need for precision vertexing and excellent central tracking are identical for similar, specific physics reactions, such as Higgs production and detection in $\gamma\gamma \to H^0 \to b\overline{b}$ and $e^+e^- \to \nu\overline{\nu}H^0 \to \nu\overline{\nu}b\overline{b}$ through W fusion. The main differences expected in the IR2 design arise from the spent beam background and other detailed background differences, from the geometry of the laser optics and the luminosity monitoring systems, and from the unique physics opportunities offered by the different collision processes available.

In this section we detail the expected backgrounds for the $\gamma\gamma$ IR2 region and begin a discussion of detector design considerations. We provide a partial list of the unique physics requirements and a complete list of the machine-related backgrounds that are presently being considered. We review a set of detector geometry and performance parameters that are in use for the current level of simulation. Results of initial debugging runs of a detailed GEANT simulation and background analysis are also presented.

B.7.2 Physics Requirements

The Higgs $\gamma\gamma$ partial width measurement will be the central focus of the $\gamma\gamma$ physics program at a future linear collider. For a light mass Higgs, precision vertexing of b-quark jets will be essential in isolating a $H^0 \to b\overline{b}$ signal from charm and light quark backgrounds. For a larger mass Higgs, excellent electron and muon identification, and good jet energy measurements will be critical in identifying final state W bosons. In this case reasonable hermiticity would allow missing energy determination of neutrinos in the final state.

For detailed measurements of the photon structure function in γe^- collisions, good forward electron acceptance and energy measurements are required for accurate determination of q^2 and x. While in searches for singley produced supersymmetric (SUSY) particles, good electron and muon identification over the largest possible solid angle are important in testing various decay hypotheses.

In e^-e^- collisions, standard e^+e^- detector parameters are required in searches for new particles such as for a Z$'$. A comprehensive detector would be needed to explore fully any evidence for new physics, such as exotic doubley charged leptons or Higgses.

B.7.3 Backgrounds

Many of the background sources will be common to both the e^+e^- and $\gamma\gamma$ interaction regions. At this preliminary design stage, we rely heavily on the detailed background studies undertaken for the e^+e^- region as discussed in Chapter 12 of the main report.

The backgrounds from upstream sources such as the muon halo and quadrupole synchrotron radiation (QSR) backgrounds will be similar, but differing due to differences in beam parameters and collimation for the e^- beams needed for $\gamma\gamma$ collisions versus the very flat e^+e^- beams. Backgrounds from nearby sources, such as beam-gas scattering, should also be the same.

In the $\gamma\gamma$ interaction region, backgrounds due to the spent electron beams from the e^--γ conversion need particular attention. After the conversion, these charged beams are naturally deflected at the final focus by the long-range Coulomb interaction. This deflection will increase the angular divergence of the beams and also create beamstrahlung photons which will lead to additional backgrounds. As discussed in Section B.6, detailed simulations of the conversion process and interaction physics are being developed. A simple parameterization of this background is discussed below.

High-energy electron-positron pairs will be created due to nonlinear effects in the interaction of laser photons with high-energy photons at the conversion points. At the interaction point, beamstrahlung photons from the disrupted electron beams will interact with themselves, with the Weizsäcker-Williams virtual photons of the opposing e^- beam and with the oncoming high-energy photons to produce additional low-energy pairs. A display and simulation of the effect of these pairs are presented in a following section.

Physics backgrounds arise from the suppressed-luminosity collisions of the spent electron beams with each other and with high-energy photons, and from hadronic backgrounds from low-energy $\gamma\gamma$ interactions. Both backgrounds will add to the inherent backgrounds associated with any particular physics study. However, the backgrounds for $\gamma\gamma$ physics due to e^-e^- and γe^- collisions will provide in themselves additional physics opportunities, while the low-energy $\gamma\gamma$ interactions provide parasitic physics similar to what has been available at lower energy machines. More detailed simulation of the hadronic backgrounds from $\gamma\gamma$ interactions and studies of the background e^-e^- collisions are being planned.

B.7.4 Detector Considerations

For a comprehensive study of $\gamma\gamma$, γe^- and e^-e^- physics, the detector chosen for IR2 will be expected to provide precision vertexing for b-quark separation, and accurate momentum and energy measurements of electrons, muons, and jets up to the beam energy over its full solid-angle coverage. Particle identification of electrons and muons will be accomplished by the calorimeter and muon tracking systems, while a central tracker with dE/dx and other detection techniques would extend the electron-hadron separation over a larger solid angle. Excellent pattern recognition and fine segmentation is required to minimize the sensitivity to machine backgrounds.

Over a large rapidity (η) range, special consideration has to be given to monitoring both the total luminosity and the differential spin-dependent luminosity, $dL_J/d\sqrt{s}/d\eta$, for each of the processes, e^-e^- , γe^- , and $\gamma\gamma$. Detector issues arise from possible interference with the laser optics in the small angle region, and from the lower rates for particular interactions at larger angles which may allow only offline luminosity measurements. Small-angle Møller scattering would provide an excellent monitor of the colliding beams in the e^-e^- mode of operation. Placement of the luminosity detectors behind the laser optics should not limit online monitoring,

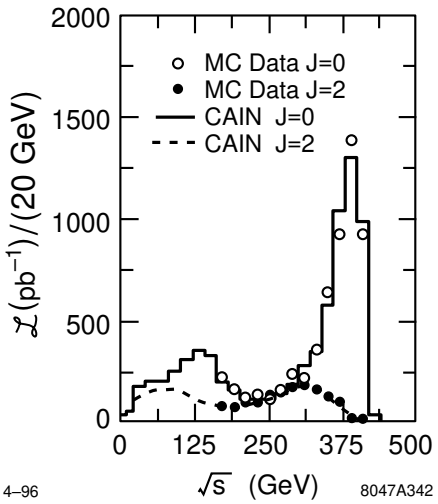

Figure B-15. *Comparison of measured and generated luminosity. The circles and asterisks are measured luminosity for $J = 0$ and $J = 2$ component while solid and dashed lines are generated luminosity for $J = 0$ and $J = 2$ respectively. The normalization corresponds to total integrated luminosity of $10\,fb^{-1}$.*

or precision offline measurements at the few per cent level. The two-photon processes, $\gamma\gamma \to e^+e^-$ and $\gamma\gamma \to \mu^+\mu^-$, allow online monitoring at small angles and precision measurements at intermediate angles for both the $\gamma\gamma$ and γe^- processes. The process of W pair production in two-photon reactions, $\gamma\gamma \to W^+W^-$, also provides an excellent measure of the $\gamma\gamma$ luminosity.

For a typical $\gamma\gamma$ collider luminosity distribution, the total weighted cross section for W pair production of about 50 pb and a selection efficiency of 15% for 4-jet reconstruction of the Ws yields 75K events per 10 fb^{-1} of integrated luminosity [Takahashi 1995]. For the spin-2 process $\gamma\gamma \to e^+e^-$ the corresponding total luminosity-weighted cross section with $\sqrt{s_{\gamma\gamma}} > 200$ GeV of 10 pb, and a detection efficiency of 70% yields 70 K events per 10 fb^{-1} [Takahashi 1995]. The spin-0 luminosity would be measured by flipping the electron and laser beam polarization simultaneously [Telnov 1993]. Figure B-15 compares the simulated $J = 0$ and $J = 2$ luminosity measurements with the generated luminosity spectra. The expected statistical errors in the W and lepton pair luminosity measurements are shown in Figure B-16.

In detailed GEANT Monte Carlo simulations of a generic detector, we have shared the basic geometry definitions for studies of both the e^+e^- and $\gamma\gamma$ interaction regions. The detector is taken to be 2 m in radius and ± 2.5 m along the beam with a 2-T solenoidal magnet field. At this stage, it consists of simple models of beam line elements and scoring planes only in the vertex and central tracking detector regions. The eventual calorimetry and muon tracking systems are not included, and the resulting detector self-shielding is not taken into account.

For the IR2 design studies, we increase the crossing angle from 20 to 30 mr as presently chosen for the laser optics design, and increase the acceptance of the outgoing quadrupoles from about $\sim$3 mr to $\sim$10 mr to transport the spent electron beam outside of the interaction region.

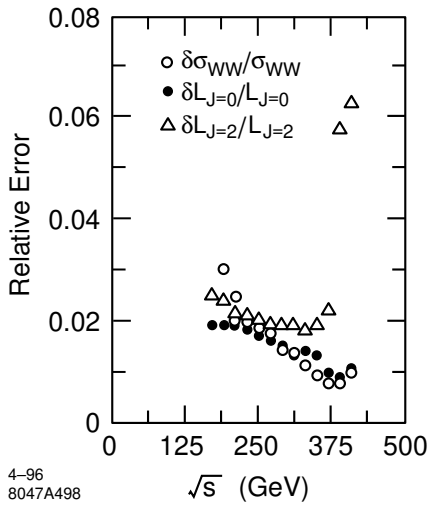

Figure B-16. *The statistical error in W pair production cross-section and luminosity measurement with integrated luminosity of* $10 fb^{-1}$. *The circles are for W measurement while the asterisks and stars are for luminosity measurement for* $J = 0$ *and* $J = 2$ *component.*

B.7.5 Initial Simulations

A GEANT drawing of the detector with an expanded vertical scale is shown in Figure B-17. At the center of the drawing are the scoring planes used in the vertex detector region from 2–10 cm in radius and ±20 cm in length. On either side are the final-focus (FF) quadrupole magnets and beam line masking chosen to minimize backscattering into the detector. For display purposes only, we plot 100 low-energy electron and positron tracks from a simulation of the beam-beam interaction in e^+e^- collisions. (We expect that the electron-positron pairs produced in the conversion and interaction points of the $\gamma\gamma$ region will be similar in energy and angular distributions.) The pairs were generated only in the forward direction of one of the beams. These tracks radiate photons as they spiral along the strong magnetic field lines to the face of the inboard FF quadrupole magnets. Secondary backgrounds are produced from electrons and photons that backscatter into the detector. Figure B-18 displays the hits in the central tracking chamber due to this background source for the $\simeq 10^4$ pair tracks expected to be produced at each bunch crossing. Earlier simulations of a conventional e^+e^- detector with an approximate crossing angle geometry indicated that this background should be tolerable [Ronan 1993].

To obtain an initial estimate of the spent electron beam backgrounds, we generate in our simulation electrons originating from the interaction point with a flat energy spectrum from 15 to 85% of the incoming beam energy. The generated angular spread of these electrons is parameterized by two Gaussian fits to independent detailed simulations of the conversion process. The fitted distributions in both transverse dimensions have a central component and a broader tail with angular spreads of ∼1 mr and ∼3–4 mr, respectively. On a highly expanded vertical scale, Figure B-19 displays 100 such spent electron tracks exiting through the downstream quadrupole magnets. More detailed simulations of the conversion process and tracking of the spent electrons through the interaction region are in progress. Also, realistic modeling of the fields within the quadrupole magnets are needed in the GEANT simulations to take account of the spent beam as it is transported out of the interaction region.

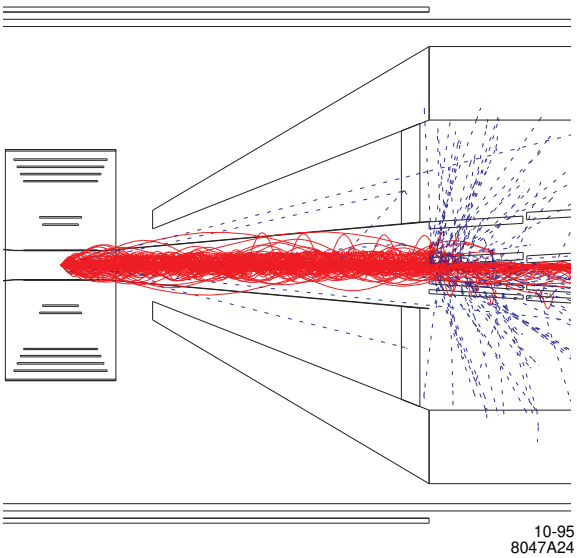

Figure B-17. *Low-energy electron-positron pair background tracks hitting the the face of downstream quadrupole magnets. Only 100 such tracks are shown.*

B.7.6 Conclusions

We are just beginning to understand the relevant design issues and parameters for a detector which could perform the physics anticipated at a future electron linear collider. We welcome volunteer help and encourage international collaboration in the development of simulation tools and eventually in the conceptual design of a detector for $\gamma\gamma$, γe^- and e^-e^- physics.

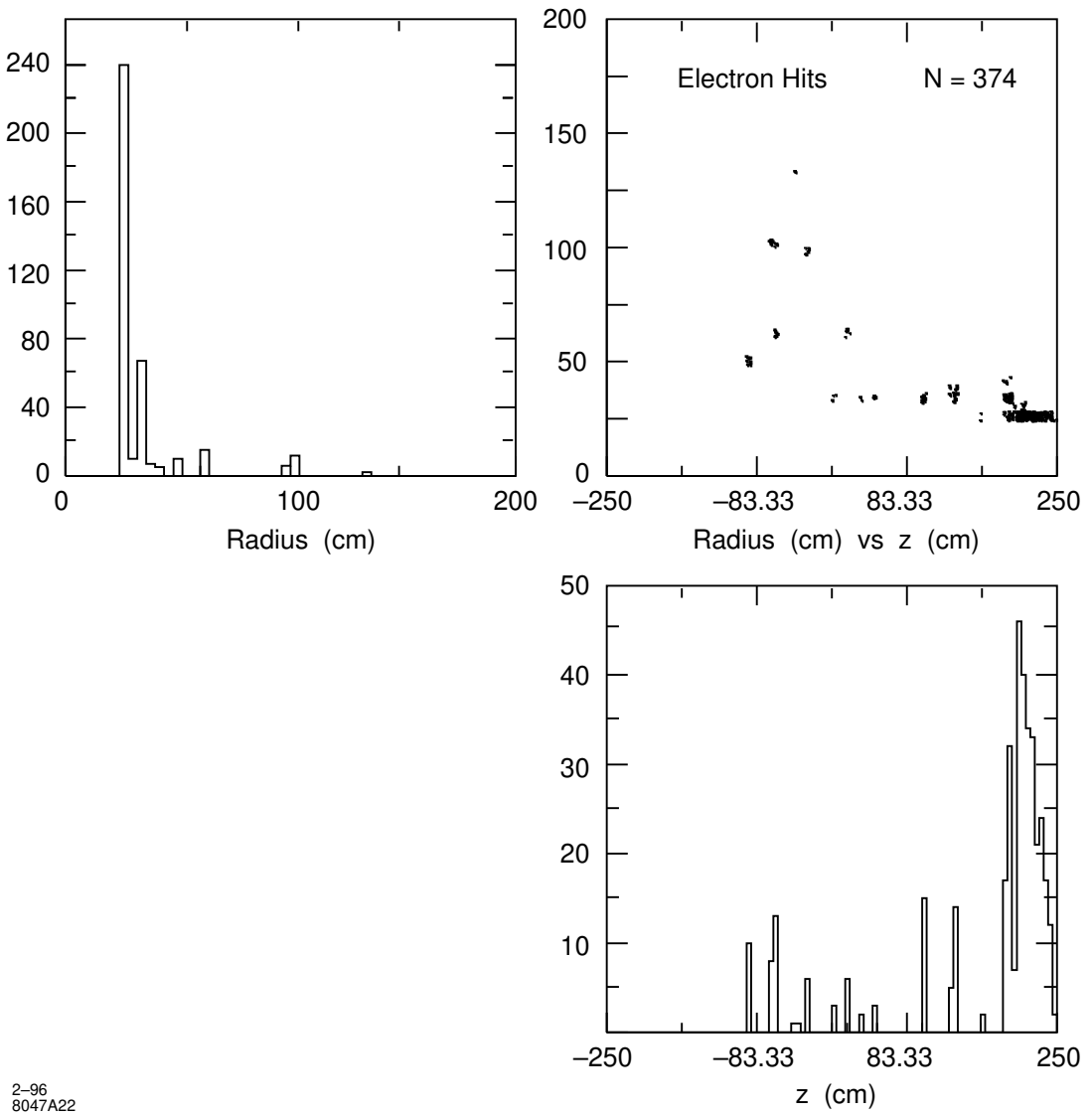

Figure B-18. *Scatter plot (2b), and radial and axial projections (2a,2c) of secondary background hits in central tracker from pair background.*

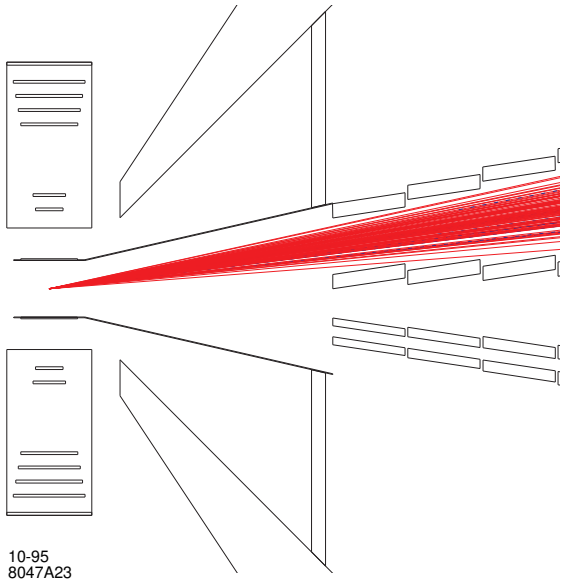

Figure B-19. *Spent electron beam exiting through downstream beam-line magnets. Only 100 rays are shown.*

B.8 Laser Optical Path in IR

B.8.1 Single-Pass Scheme

This section considers some of the practical issues in actually bringing the laser beams into (and out of) an interaction point centered in a HEP detector of the sort that is described in the previous section. A solution is shown in Figure B-20. The case considered here is the simplest one. Each electron beam has an opposing laser beam which is backscattered from it immediately prior to the interaction point. The laser beam, which is essentially unaltered in the process, is then disposed of. The beams are brought in from opposite sides and follow very similar (but not identical) paths along opposite directions. Before discussing the scheme in more detail, it is worthwhile to explain some of the constraints that are encountered in this problem.

- Because of the extremely high intensities involved, transmissive optics are, for the most part, not feasible. This occurs because in the final analysis, the index of refraction of all optical materials is a function of the intensity of the laser light in it. These nonlinearities give rise to a filamentation instability if the total length of material in the system is sufficiently large. The limitation from this so called "B-integral" problem [Siegman 1986] means that such devices as lenses, Pockels cells, and polarizers may not be used after the gratings in the compressor. In fact, the limitations on the design of the optical path produced by this problem are probably such as to just allow a pair of quartz windows for the beam to enter and leave the vacuum system of the accelerator. Beyond these two windows, all optical elements will presumably be reflective; *i.e.,* dielectric mirrors. This limitation also implies that the laser beam will be transported in vacuum.

- Focusing of the beam must be optimized to produce the desired peak intensity (limited by nonlinear effects in the backscattering process as discussed above) and a sufficiently long length of such intensity that most of the electron bunch is converted into photons. This optimization was discussed above. The practical consequence of this is that the "$\mathrm{f}_{\#}$" of the laser focusing will be fixed by this optimization. The $f_{\#}$ is defined roughly as the ratio of the focal length to the diameter of the focusing mirror, as illustrated in Figure B-21, assuming that the mirror is uniformly illuminated. For Gaussian beams, the diameter of the focusing mirror is somewhat arbitrary, but we will take it as the intensity $1/\mathrm{e}^2$ diameter. With this definition, one can show that $f_{\#} = 1/4\sigma_{x'}$, where $\sigma_{x'}$ is the rms angular divergence of the focussed laser beam. In the current design, we have $\sigma_{x'} \approx 27.9\,\mathrm{mr}$ and $f_{\#} = 8.65$.

- Effective use of the laser requires that the optical axis of the laser beam be parallel with the direction of the electron beam to within an angle small compared to the aspect ratio of the laser bunch. The degradation in the general case is given by [Xie 1995] (We do not consider the possibility of "crabbing" the laser beam here.)

$$\frac{L(\theta)}{L(0)} = \frac{1}{\sqrt{1+(\theta/\theta_0)^2}}, \quad \text{where} \quad \theta_0 = \sqrt{\frac{\sigma_{x1}^2+\sigma_{x2}^2}{\sigma_{z1}^2+\sigma_{z2}^2}} \quad , \tag{B.26}$$

  The σ_xs are the transverse sizes of the two crossing beams and the σ_zs are the longitudinal sizes. In our case, the expression for θ_0 is dominated by the size of the laser beam and reduces to $\theta_0 = \sigma_x/\sigma_z$. From the discussion above, one can infer that the aspect ratio of the laser is approximately $4\mathrm{f}_{\#}$. Since the angle between the optical axis and the electron beam is $1/2\mathrm{f}_{\#}$, the minimum degradation if the disrupted beam does not pass through the mirror is $1/\sqrt{5}$. Because of this degradation, a through-the-lens design has been implemented.

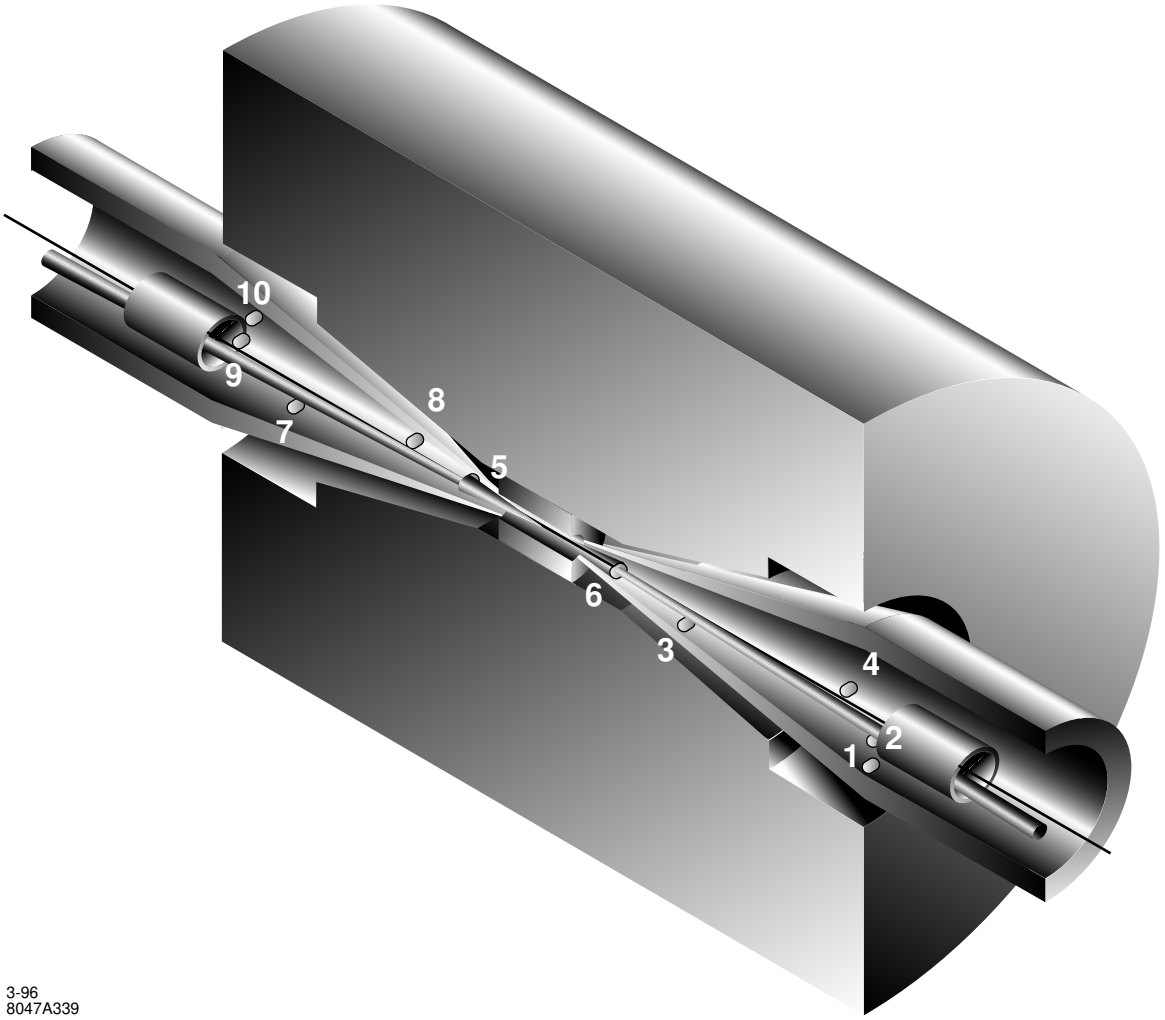

Figure B-20. *The layout of laser optical path in the IR2. The paths followed by the various beams are described in the text. The mirrors have an elliptical shape due to the overlap of the two circular beams. The shapes shown for the mirrors represent the outer edge of the flattop beams. While no provisions are shown for the edges of the mirrors or for mirror supports, space appears to be available.*

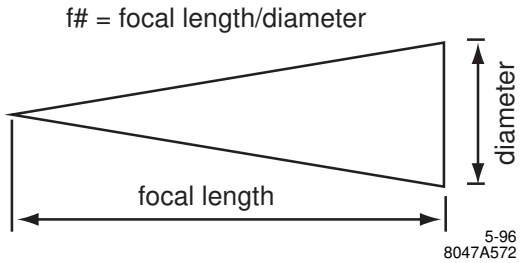

Figure B-21. *The definition of the $f_{\#}$ of an optical system.*

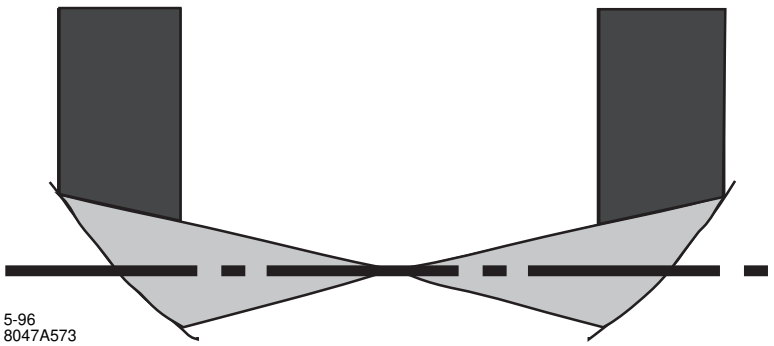

Figure B-22. *The off-axis paraboloid is both difficult to align and sends the beam path through space better occupied by the detector.*

- Given both the high peak and average power involved, it is almost certainly necessary to transport the "spent" laser beam out of the IR to an external dump. This also allows external monitoring of the optical quality of the beam after it has gone through focus.
- The two electron beams cross at only a small angle. This angle is limited by the creation of synchrotron radiation in the B-field of the detector. It must be greater than zero in order that the disrupted beam from the opposite side has a separate path by which to exit the detector. Since this angle, which in the current design is 30 mr, is small compared to the half angle associated with the focusing of the laser beam ($1/2f_{\#} \approx 57.8$ mr), it follows that the "used" beam from one side will land on the focusing optic for the other side.
- The two conversion points are separated (1 cm) in space so that softer photons (which are produced at larger angles) will diverge before the interaction point and not interact. This will introduce a "walk" into the paths of the two laser beams so that at a large distance from the IP the beams eventually separate.
- If the two beams share the same mirrors at some point (and this seems inevitable), then the mirrors probably should not be located at the points in space where the two pulses (one from each direction) overlap in time as this will significantly increase the peak intensity on the mirror.
- At first glance, there might seem to be advantages to bringing in the laser beam using an off-axis paraboloid as shown in Figure B-22. Such schemes suffer, however, both from difficulties in alignment and from a need to direct the beam through a region which is naturally occupied by the detector.
- Damage to the dielectric coatings on both the flat and curved mirrors used to transport the laser is an issue. Ultimately, this sets a limit on how close the closest optic can come to the interaction point.

The design for the laser-optical path is shown in Figure B-20. The central cylinder represents a vertex chamber. The more-or-less cylindrical object outside of that represents the rest of a generic cylindrical detector. A previous proposal [Miller 1995] in which the laser beam focuses twice has been implemented. This makes it possible to maintain near-normal incidence on all the optics in the system, and keep the laser beams in the vicinity of the conversion points inside a cylinder which is roughly defined by the outer radius of the final focusing optic used. The incident electron beams are shown as thin lines on the far side of the detector. The disrupted electron beams are shown as cones slightly offset from the incident beams. The axis of the detector is located between the incoming and outgoing electron beams.

As was mentioned above, the two laser beams enter from opposite sides of the detector and trace similar, but not identical, paths in opposite directions. These paths are distinct because the incoming electron beams make a small angle with each other, and because the conversion points are offset from each other by 1 cm.

The path followed by the laser beam incident from the right in Figure B-20 is as follows. A round and collimated (*i.e.,* parallel) beam incident upon the right (far) side of mirror 1 is reflected vertically onto mirror 2. It is, in turn, reflected in a more-or-less horizontal direction onto the right side of mirror 3. This mirror reflects the beam onto the right side of mirror 4. At this point the beam is still parallel. Mirror 4 focuses the beam to a point over the center of mirror 6. This is done to minimize the clear region which must be provided as the beam is brought onto mirror 5 (the final focusing mirror for this side). After passing through this focus, the beam diverges and lands on the left side of mirror 5. Mirror 5 focuses the beam to a diffraction limited spot 0.5 cm past the interaction point where it backscatters from the electron beam which entered the detector from the same side.

At this point, the only task left is to extract the beam from the inside of the detector. Mirrors 6–10 are used to bring in the second laser beam to convert the second electron beam. Because of the very small angle between the two electron beams, and because the final focusing optic has its axis coincident with the electron beam, the "spent" beam will follow a path out of the IR which is nearly coincident with that of the other incoming beam. These paths are not exactly coincident because of the 20 mR angular offset of the two electron beams. This offset of laser beams is what produces the requirement for oval (as opposed to circular) mirrors.

After passing through the conversion point, the original laser beam diverges and strikes mirror 6. Mirror 6 will refocus the beam to a point just under mirror 5, from which it will diverge and land on mirror 7. Mirror 7 will recollimate the beam and send it onto mirror 8. After leaving mirror 7 the beam is once again parallel. It is then reflected from mirrors 9 and 10 in a manner similar to that by which is entered on the opposite side.

It must be noted that because mirrors 6–10 will be optimized to produce a diffraction-limited spot for the beam entering on that side, and because the beam exits at a slightly different angle, the optical path on exit will introduce aberrations into the beam. Whether or not these aberrations can be corrected subsequently so that the beam may be diagnosed after exiting the detector is an open question.

The mirrors in this scheme have been located where one finds the luminosity monitor in a conventional e^+e^- detector. Since there does not appear to be an analog of Bhabha scattering in $\gamma\gamma$ collisions, this is presumably not a major difficulty. If this region needs to be instrumented (to ensure, for instance, maximum hermiticity of the detector), then the material associated with the mirror is probably tolerable. A typical mirror will have a thickness of $\frac{1}{6}$ of its diameter. This will produce 10% of a radiation length of fused quartz over some fraction of the azimuth.

B.8.2 Optical Beam Focusing

Previous work [Meyerhofer 1995a] has sometimes assumed that Gaussian laser beams would be used at a $\gamma\gamma$ collider. This is not optimum for a couple of reasons. High-power lasers such as will be needed for this project are typically build with flattop beams to achieve the maximum fill factor. The idea is roughly the following. The cost of the laser depends on both the aperture and the peak intensity within that aperture. Having paid for both of these, the maximum energy is extracted by uniformly filling the aperture; *i.e.,* maximum fill factor. Since, as is explained below, it is probable that the disrupted electron beam will pass through the middle of the final laser focusing optic, a beam profile which peaks in the center is not optimum. Figure B-21

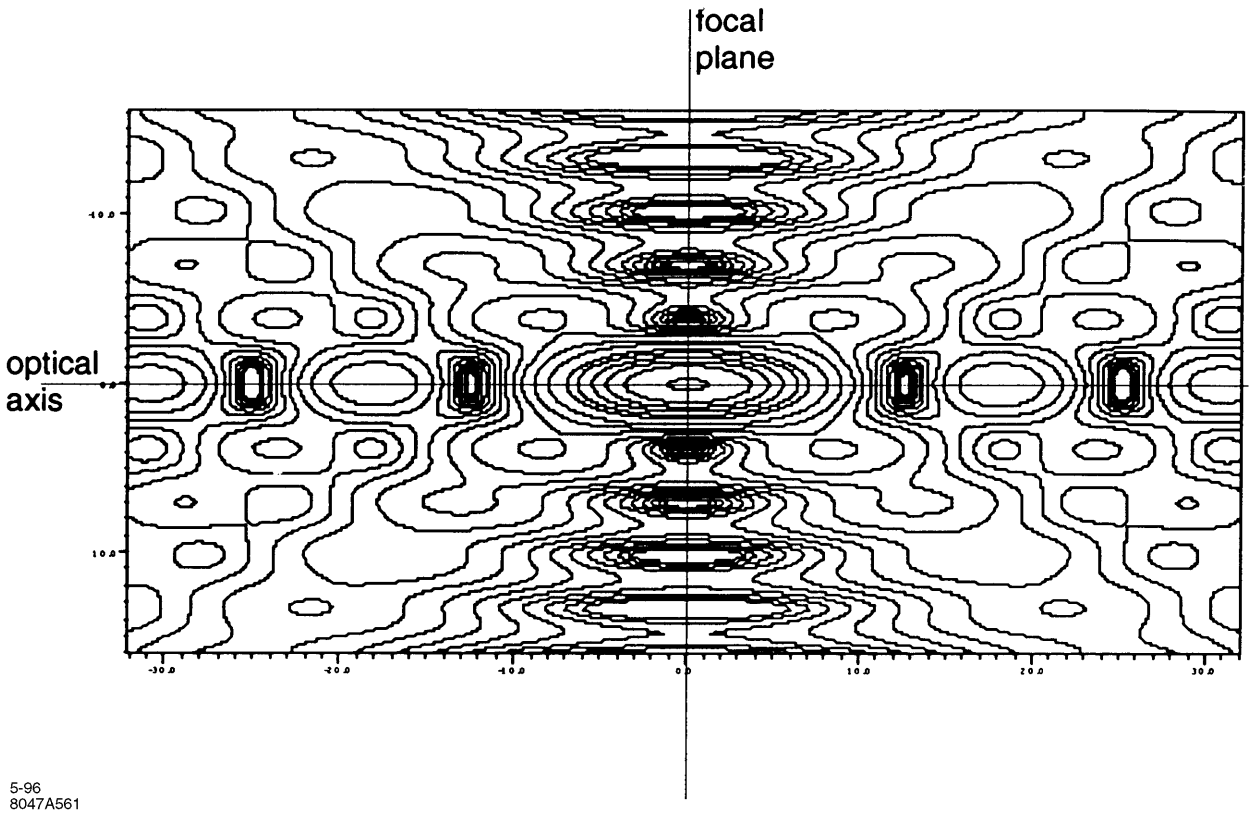

Figure B-23. *The behavior near best focus from a flattop beam.*

shows the definition of the $f_{\#}$ of a focused beam. The resulting properties of the beam at the best focus are given in Table B-4. It is seen that while the Gaussian profile provides simple analytical expressions near best focus, the flattop beam produces a much more complicated pattern as shown in Figure B-23.

Because the optimization has been done for Gaussian beams, a comparison has been made between the focal spots for the two cases. This is shown in Figure B-24. A flattop beam requires a slightly larger beam (smaller $f_{\#}$) to produce a similar spot. The exit hole required to let the disrupted beam pass through produces only a 2% energy loss in this case. Table B-5 gives a summary of the laser and electron beam parameters. Table B-6 is a summary of the parameters relevant to the laser optics design.

B.8.3 Laser Damage of Optics

The particular optics used in this design are not expensive. They are neither extremely large, nor are the surfaces expected to be particularly complicated. On the other hand, their reliability will remain a critical issue if a $\gamma\gamma$ collider is to operate successfully. Definitive statements on this subject can not be made at this time because no data exists on the damage threshold for multilayer surfaces for the particular time structure of the laser pulse which would be required in this case. Data exists for the case of single picosecond scale

	Flattop	Gaussian
$I(r, z=0)$	$I_0 \left[\frac{2J_1(r/s)}{r/s}\right]^2$	$I_0 \exp\left(-2\frac{r^2}{w^2(z)}\right)$
	$s = \frac{f_\# \lambda}{\pi}$	$w(z) = w_0 \left[1 + \left(\frac{z}{z_R}\right)^2\right]^{1/2}$
$I(r=0, z)$	$I_0 \left[\frac{sin(z/z_0}{z/z_0}\right]^2$	$I_0 \left[1 + \left(\frac{z}{z_R}\right)^2\right]^{-1}$
	$z_0 = \frac{8}{\pi} f_\#^2 \lambda$	$z_R = \frac{4}{\pi} f_\#^2 \lambda$
Effective area	$\frac{f_\#^2 \lambda^2}{\pi}$	$\frac{\pi w_0^2}{2} = \frac{2 f^2 \lambda^2}{\pi}$

Table B-4. *The beam parameters at focus for Gaussian and flattop beams.*

Electron beams:	
μ-pulse / macro-pulse	90
repetition rate	180 Hz
angular offset	±15 mR
spent beam divergence	±10 mR
Laser beams:	
wavelength, λ	1.05 μm
beam profile	5-cm diam. flattop
energy	1 J / pulse
length	1.8 psec
μ -bunches	90 at 1.4 ns
repetition rate	180 Hz
power (per beam)	16 kW

Table B-5. *Beam parameters used in this study.*

Optics:	
$f_\#$ (flattop)	7 (±71 mr)
Distance to first mirror	35 cm
Area of first mirror	20 cm^2
Fractional area of first hole	2%
Fluence	0.05 J/cm^2/*pulse*
Vertex chamber:	
Inner radius/solid angle	4 cm/ 0.986
Outer radius/solid angle	12 cm/ 0.894
Total length	48 cm
Distance to first quad.:	200 cm
Masking:	100–150 mr

Table B-6. *Parameters of the design proposed in this study.*

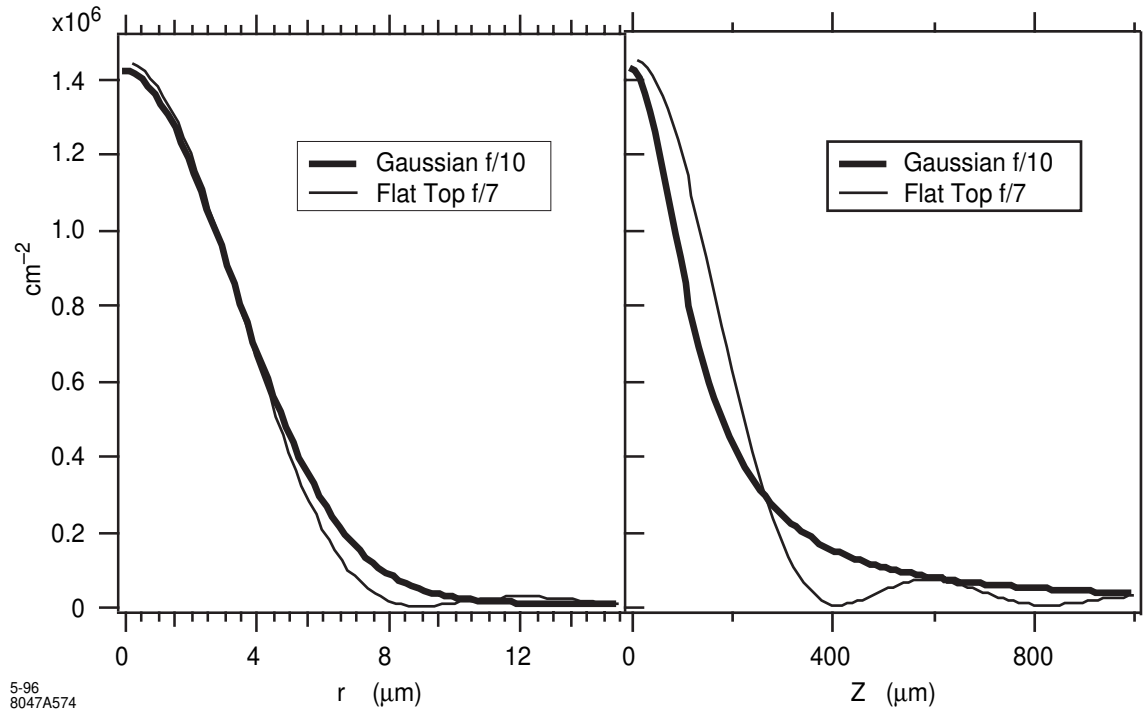

Figure B-24. *A comparison of the radial and axial dependence of the intensity for Gaussian and flattop beams. Similar sizes are obtained when the $f/\#$ of the flattop beam is about 0.7 times that of the Gaussian beam.*

pulses. Extensive data exists for much longer length pulses (nanosecond time scales), and for collections of nanosecond scale pulses which produce very high average powers. The three limits are considered below.

- On the time scale of a single pulse (1.8 ps), measurements have recently been made at LLNL on commercial multilayer surfaces [Stuart 1995a]. Damage thresholds in the range of 0.7 to 2 J/cm^2 have been observed. This is more than a factor of four above the anticipated fluence of $0.05\,J/cm^2$.
- On nanosecond time scales, the situation is less clear. The anticipated fluence is $4.5\,J/cm^2$ spread over 126 ns. The damage threshold for continuous pulses of this length is 100 to 200 J/cm^2. While this is well above the anticipated operating point, the validity of this averaging has not been demonstrated. No data exists for collections of picosecond pulses separated by a few nanoseconds and which accumulate to fluences of this magnitude.
- The average flux on the final optic is $0.83\,kW/cm^2$. Since this is below the levels of 3 to $5\,kW/cm^2$ which are routinely used in the laser isotope separation program (AVLIS) at LLNL, it does not appear to be a problem.

It is worth noting that the overall scale of the optics, masking, and vertex chamber is set by the inner radius of the vertex chamber and by the damage threshold of the first optical element. If fluences higher than the design fluence are possible (and this certainly cannot be ruled out at this point), then all dimensions can be scaled down if it is desired to place the vertex chamber at a smaller radius.

At this point there is a clear need for a detailed optical design of the elements involved here. This would determine the particular surfaces required on the focusing elements to verify that a defraction-limited spot can be produced. It would also make it possible to determine the magnitude of the aberration introduced on the exit path and to determine if it is possible to correct these aberrations externally. Such corrections would be needed to use the transmitted beam to verify the quality of the focal spot.

There are also questions about the damage thresholds of the optics as well as questions about the optics resistance to damage by radiation.

The optical design here has been based on Table B-1, with A =1 J and $I = 1 \times 10^{18}$ W/cm^2. As discussed elsewhere, the non-linear effect in Compton conversion is not negligible. the non-linearity can be avoided by increasing A to 3 J and decreasing I by a factor of three. This will increase the requirement on the laser power, as well as power on the mirror by a factor of 3. The focusing optics also changes from f/7 to f/10, with the result that the mirrors are located a little further out from the IP.

B.8.4 Ideas on Relaxing Average Laser Power Requirement Via Multipass Optics

In a gamma-gamma collider, a high-energy electron bunch is converted into a burst of gamma rays by Compton scattering with an intense laser pulse. Assuming the laser source has the same pulse structure and repetition rate as that of the electron beam and assuming that each laser pulse is used only once, the required average laser power would be around 20 kW, three orders of magnitude higher than what has been achieved with any laser having TW peak power. However, the required average power can be significantly reduced if the laser pulses can be reused, because the laser pulse suffers little loss in energy after each scattering. In this section, we explore the possibilities of reusing the laser pulses with specially designed optics.

There are two approaches to this problem. The first one is a multipass approach in which a laser pulse is made to pass through the conversion point a finite number of times before being thrown away. In this way, the average power is reduced by reducing the number of pulses needed. The second approach may be called pulse stacking in which a train of weaker laser pulses are stacked up in an optical cavity to make a stronger pulse for intracavity conversion. In designing optics for both approaches, using transmissive optical elements should be avoided if possible to minimize the nonlinear transverse and longitudinal pulse distortion at high power.

To illustrate the idea, an example of multipass optics based on all reflective elements is schematically shown in Figure B-25, in which a laser pulse is made to pass through a CP eight times, four in each direction. This is done by using two mirror banks each with eight individual mirrors. Each individual mirror is placed in the numbered order along the optical pass according to the sequence the laser pulse is kicked. Such a kicking pattern guarantees the same pass length for each round trip the laser pulse makes passing through a CP. With some modification, the scheme in Figure B-25 can also be made to accommodate two conversion points separated by a few mm while requiring laser pulses to pass through the two conversion points in opposite direction.

The reduction factor in the required laser average power for the multipass approach is limited because the number of mirrors that can be utilized is limited due to the tight space near the interaction region, and due to the build-up of aberration. To make better use of the limited space, it is desirable to have laser pulses bounced back and forth along the same pass, thus forming a cavity mode. By stacking up weaker externally injected pulses inside a cavity, the factor of reduction in average power could be up to the cavity Q.

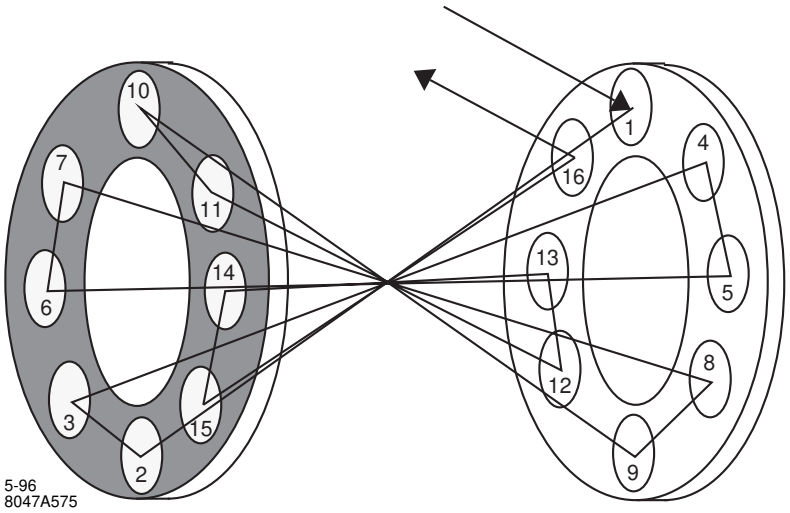

Figure B-25. *Multipass optics with reflecting mirrors.*

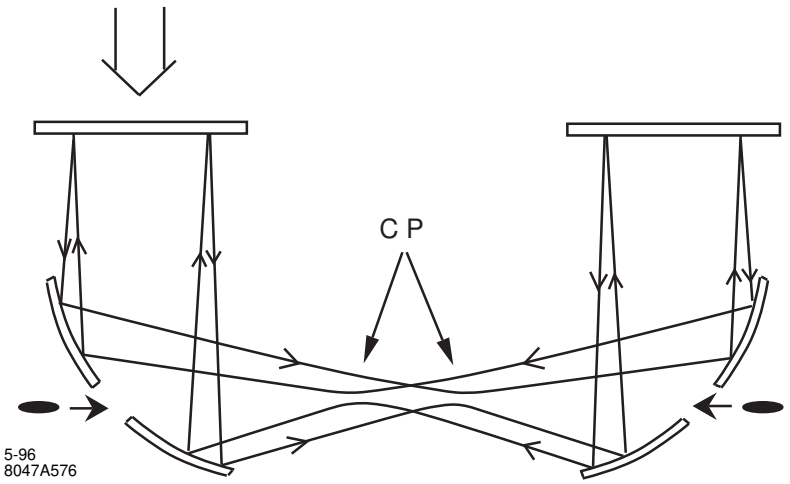

Figure B-26. *A double confocal resonator.*

For gamma-gamma colliders the desirable cavity mode should have certain characteristics. The double confocal resonator seems to be an ideal choice for this purpose. A double confocal resonator is effectively made of two usual confocal resonators. The usual confocal resonator is formed by two curved mirrors separated by a distance equal to the radius of curvature of the mirrors. Putting two confocal resonators together, one gets a ring resonator with four identical mirrors separated by equal distance. Folding such a ring resonator with two flat mirrors one gets the double confocal resonator shown in Figure B-26.

The double confocal cavity has several advantages:

- A dominant cavity mode can be made to have a central peak at each focal point and an annular shape at each mirror location.
- The focal spotsize or Rayleigh range is determined by the limiting intracavity apertures and are therefore easily adjustable.
- The annular mode distribution on the cavity mirrors allows large holes on the mirrors for electron beam and debris passage without sacrificing cavity Q.
- The annular shape on the mirrors also gives larger mode sizes thus reducing the power loading.
- With proper external mode for injection, two focal points can be formed each opposing to an incoming electron beam.
- In addition to these advantages, only one unavoidable transmissive window is used in Figure B-26 to couple laser pulse into the cavity in the vacuum system. Because a weaker pulse is needed for stacking, the power going through the window can be quite small compared to other approaches requiring full peak power injection.

The excitation of the desired mode in the cavity is largely dependent on the external mode preparation. Roughly speaking, the injection mode should have an annular amplitude distribution and a nearly flat phase front at the location of the transmissive window. If the external mode exactly matches the desired cavity mode, the cavity mode can be established right away, otherwise the resulting mode deterioration and slower intracavity power build-up could affect collider performance. There are ways to convert the usual Gaussian mode from a laser into an annular shape, for example by using an axicon or a profiled transmissive element. Fortunately, all these can be done outside the crowded interaction region and high-vacuum environment.

B.9 Gamma-Gamma Final Focus System

The goal of the FFS for the IR2 is to produce $\beta_x^* = \beta_y^* = 0.5\,\mathrm{mm}$, as explained in Section B.3.3. However, the current version of the $\gamma\gamma$ final focus system has $\beta_x^* = 0.9\,\mathrm{mm}$ and $\beta_y^* = 0.7\,\mathrm{mm}$. This is not accidental because with these beta functions at the IP the chromaticity of the final focus doublet is the same as in the e^+e^- case. Efforts to find smaller β^* values resulted in higher x and y chromaticities, implying a greater sensitivity to the quadrupole placement tolerance and also a greater complexity and length of the FFS. The current solution of the FFS for the IR2 has a similar complexity as that for the IR1, being essentially an adaptation of the already existing solution for e^+e^- case to the new regime of the $\gamma\gamma$ collision.

B.9.1 Beam Parameters

Table B-7 lists the electron beam parameters necessary for a discussion of a final focus system of a $\gamma\gamma$ interaction region. Note that beta-functions at the IP are optimized differently from the ones for the e^+e^- collision—with a relaxed β_y^* and a tighter β_x^*. The following considerations are behind this choice: High-energy γ quanta appearing in a conversion of photons on electrons are emitted within the angular spread $1/\gamma$ towards a direction of the parent electron.

Thus, a spotsize of the high-energy γ beam at the IP reflects a spotsize of the electron beam plus additional contribution due to the angular spread of the γ quanta at the CP. This contribution, $\delta\sigma_{x,y}^*$, depends from a

E (gev)	250
ϵ_x (m×rad)	1×10^{-11}
ϵ_y (m×rad)	1×10^{-13}
β_x^* (mm)	0.9
β_y^* (mm)	0.7
Horizontal beam size at the IP (nm)	96
Vertical beam size at the IP (nm)	8.5

Table B-7. *Beam parameters*

distance b from the CP to the IP

$$\delta\sigma_{x,y}^* = b/\gamma \quad . \tag{B.27}$$

We would like to have

$$\delta\sigma_{x,y}^* \lesssim \sigma_{x,y}^* \quad . \tag{B.28}$$

Therefore,

$$b \lesssim \sigma_{x,y}^* \gamma \quad . \tag{B.29}$$

Thus, it is more convenient to have larger β_y^* and, correspondingly, larger σ_y^* because it allows the CP to be placed further away from the IP. At the same time, it is necessary to reduce β_x^* to compensate the reduction in the luminosity when β_y^* is increased. Note that, contrary to the e^+e^- case, there are no constraints on the beam profile at the IP arising from the beamstrahlung effects.

B.9.2 Final Focus Doublet

For linear colliders, the chromaticity is defined as the change in the IP waist position when the particle has an energy unequal to the design energy. A change in the horizontal or vertical waist position is characterized by the presence of a term x'^2 or y'^2 in the beam line Hamiltonian, which is precisely the terms in the Hamiltonian of a drift. The horizontal or vertical chromaticity is thus characterized by the presence of terms $\delta x'^2$ or $\delta y'^2$, where δ is the fractional energy error. Since the change in the horizontal or vertical IP position due to the these terms is given by

$$\Delta x = \frac{\partial H}{\partial x'} \qquad \text{or} \qquad \Delta y = \frac{\partial H}{\partial y'} \tag{B.30}$$

and the derivative of a quadratic function introduces a factor of 2, it is usual to define a horizontal and vertical chromatic length L_x^c and L_y^c as the coefficient of $\delta x'^2$ or $\delta y'^2$ respectively.

The spread in spotsize from spread in incoming angle can be written

$$\frac{\Delta x}{\sigma_x^*} = \delta\xi_x \frac{x'}{\sigma_{x'}^*} \quad , \quad \text{where} \quad \xi_x \equiv \frac{L_x^c}{\beta_x^*} \quad . \tag{B.31}$$

The quantity ξ_x is called the chromaticity. It is a dimensionless number. A value of one would indicate that the chromatic aberration gives a contribution to the beam size equal to the linear term. the contribution to this term coming from the final doublet can be calculated by the formula

$$\int ds\ k_x(s)\beta_x(s) \quad . \tag{B.32}$$

	Length, (m)	Gradient, (kg/mm)	Bore radius, (mm)	Beam-stay-clear
F-quad	1.43	4.50	3	$11\sigma_x$, $50\sigma_y$
D-quad	1.16	−3.38	4	$19\sigma_x$, $41\sigma_y$

Table B-8. *Doublet parameters*

since the phase advance from the IP to elements of the doublet is very close to $\pi/2$.

It is well known that the chromaticity of a lattice with only quadrupoles will be non zero, and to compensate the chromaticity one must add sextupoles to the beam line. To minimize sextupole strength, one first seeks the quadrupole configuration that minimizes the chromaticity.

The minimum chromaticity from quadrupoles occurs by placing strong quadrupoles as close to the IP as possible, without interfering with the function of the detector. Doing this in both planes of course requires a doublet. The rays on the IP side of the doublet will be focused to the IP. The divergence of the rays on the upstream end of the doublet will have a divergence that is characterized by the length of typical beam line modules of phase advance $\pi/2$ or π. Thus the function of the doublet is to focus parallel rays to the IP.

Thus the doublet design can be separated from the beam line design. One first seeks the double giving the minimum chromaticity parameters, taking into account detector requirements, constraints of materials available for quadrupole fabrication, tolerances on quadrupole position and field strength, and synthrotron radiation within the doublet.

As a first attempt to design the final focus system for $\gamma\gamma$ collisions, we decided to keep chromaticity of the final focus doublet close to the chromaticity of the e^+e^- final focus. Thus, with $L^* = 2\,\mathrm{m}$, the minimum beam-stay-clear requirement of $10\sigma_{x,y}$, and the maximum pole-tip field in the permanent magnet quadrupoles of 1.35 T, we arrived at the doublet parameters described in the Table B-8. Note, that the quadrupole nearest to the IP is of the F-type and the length of the drift space between the F and D quadrupoles is 0.3 m. This doublet has an x-plane chromaticity $\xi_x = 3100$ and y-plane chromaticity $\xi_y = 24500$. These values are to be compared with $\xi_x = 1100$ and $\xi_y = 23000$ in the e^+e^- case.

The size of these chromaticities indicate the precision with which the chromatic correction must be made. This has, of course, direct implications for the system tolerances. It also places constraints on the synchrotron radiation allowed in the system, because the change of particle energy within the system implies a failure of the chromatic balance built into the optics. However, for the present design of the doublet, the increase of the beam spotsize at the IP due to the Oide effect is negligible.

B.9.3 Chromaticity Compensation

We follow a standard approach to the chromaticity compensation of the final focus doublet. Similar to the e^+e^- final focus system, the $\gamma\gamma$ final focus system consists of the five modules. These are, in order of their location beginning from the IP: final transformer (FT), vertical chromaticity correction section (CCY), beta-exchanger (BX), horizontal chromaticity correction section (CCX) and beta-matching section (BMS). All modules have exactly the same functions as in the e^+e^- case. Figure B-27 shows the beta and the dispersion functions along the final focus system from the entrance of the BMS to the IP. The total distance from the entrance of the BMS to the IP is about 1600 m.

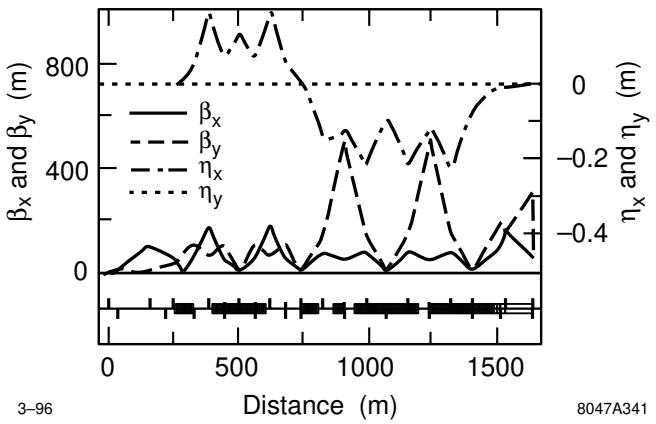

Figure B-27. *Horizontal and vertical beta functions from BMS to IP for 1600 m-long $\gamma\gamma$ final focus system at 500 GeV.*

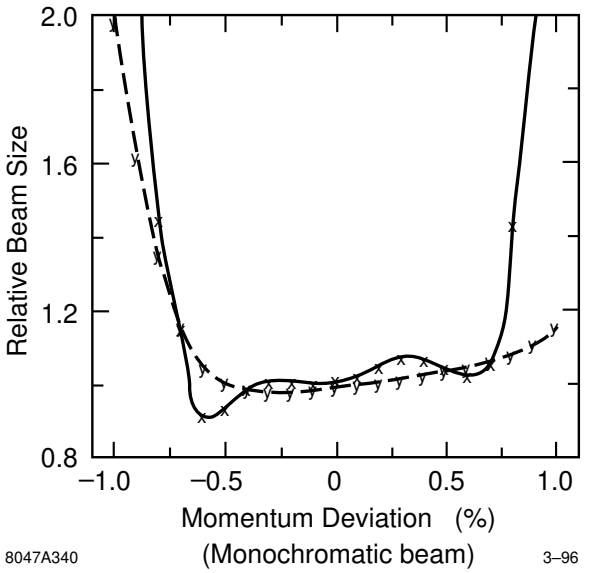

Figure B-28. *Relative increase of spotsizes as a function of momentum offset Δ of a monoenergetic beam.*

Figure B-28 shows the vertical and horizontal beam size as a function of the momentum offset Δ of a monoenergetic beam. The spotsizes are given in units of the values for zero momentum offset. The momentum bandwidth for a 10% blow-up of either spotsize is $\pm 0.6\%$.

It was recently shown (Dick Helm) that by increasing the overall length of the Final Focus section to 1750 m one can have $\beta_x^* = \beta_y^* = 0.5\,\mathrm{mm}$ with the energy bandwidth about $\pm 0.5\%$.

B.10 Extraction and Diagnostic Line

The extraction line has the important functions of optimizing luminosity, characterizing beam properties at the IP and transporting beams from the IP to a dump with minimal background in the particle detector from this or any secondary function along the way. Beam characterization includes measurements of current, position, profile, energy, polarization, and low-order correlations on a bunch-to-bunch basis for feedback and stabilization. A prototype optical and diagnostic layout will be developed that provides such functions. In many respects it will be similar to the corresponding e^+e^- dump line that was presented in Section 11.8.

One presumed difference with that line is the difficulty of disposing of the high-power photon beam. We note that the outgoing beamstrahlung power approaches 10% of the incident, primary beam power for the e^+e^- IR. This was dealt with by implementing a common dump for both leptons and photons. The main question to be answered here is what distance is then available and whether it is reasonable from the standpoint of detector backgrounds and the various secondary functions that one would like to implement.

To accomplish all of the various tasks, we need to know the detailed composition and characteristics of the outgoing beam(s) under different, possible circumstances. Clearly, these characteristics depend on those assumed for the incoming beam. Based on some assumed set of incoming beam parameters, the transport optics, and the CP and IP conditions, we can then make predictions for the outgoing beams that are used to guide the design of the outgoing, beam line optics. Typically, the outgoing beams have a significant number of pairs as well as the primary, degraded electrons from the Compton conversion and more photons than leptons from multiple scattering within the strong laser conversion field.

Thus, the primary difference for this IP is the degraded electron beam that is highly disrupted but also necessarily includes a significant fraction of electrons with their full incident energy.

Clearly, the detector fields begin to have a serious influence on the incoming and outgoing beam characteristics with such large crossing angles. Thus, if background simulations for the detector imply an unacceptable situation, this procedure has to be iterated until a consistent solution is achieved. This is just now being done for the e^+e^- channel as described in Chapter 12.

While our overall goal is to optimize the luminosity while disposing the various beam components into their respective dumps, it is also important to provide any monitoring and feedback that can optimize the usable collision rate at the IP. Thus, beyond simply dumping the beam, there are other functions that run from the absolutely necessary to the desirable that will be considered as part of the dump line in roughly descending order of importance:

- Beam control and stabilization.
- Diagnostics and monitoring—including luminosity and polarization.
- e, μ, n, γ secondary beams and parasitic experiments.
- Polarized sources for γ, μ and e^+ beams.
- Energy recovery.

Separate discussions on these possibilities can be found in Section 11.8 of the ZDR for the e^+e^- channel. While the outgoing line is more difficult here, it can be accomplished in a similar way to that discussed in Section 11.8 because that design was made to be compatible with such a possibility there.

Energy per micropulse	1 J
Pulse duration	1.8 ps
Focusing f-number	7
Wavelength	0.8-1 μm
Pulse structure	90 micropulses(1.4-ns separation)
	180-Hz macropulse rate
Average power	16 kW

Table B-9. *Laser requirements for NLC γ-γ option*

B.11 Laser Technology I: Solid State Lasers

As we have seen in Section B.3.2, the optical beam for $\gamma\gamma$ or γe^- colliders consists of a sequence of TW micropulses, each a few ps long, with an average power of tens of kW. The requirements are summarized in Table B-9. Unless multipass optics can be used in the interaction region, these are the requirements for the lasers. Solid state lasers meeting the requirements would probably be available for the colliders to 500 $\times$ 500 GeV, but FEL would be used for higher energy colliders.

The solid state lasers for the $\gamma\gamma$ colliders have been discussed in two recent articles [Meyerhofer 1995a, Clayton 1994, Clayton 1995]. There will be two of these laser systems, one each for each colliding electron beam. While the energy, pulse duration, and focusing can be met with currently operating lasers, [Perry 1994a], these lasers have not yet met the average power requirements. The average power of high peak power systems has, however, been increasing rapidly recently, driven by activities such as the Isotope Separation program at LLNL and facilitated by the development of high power laser diode pump sources. The system requirements could also be reduced by using a multipass conversion point. It is expected that the system requirements will be met with a series of 1-kW, diode-pumped, solid-state, chirped pulse amplification laser systems. These unit cells will be fed by a single, phase-locked oscillator to insure timing stability.

Many of the components of the required laser system can be achieved with technology which is currently being developed for applications other than the $\gamma\gamma$ collider. As a result, a single unit cell prototype laser module could be developed over the next few years.

B.11.1 Laser Materials

Although both dye and excimer laser systems can easily meet the short-pulse requirement of the NLC, achieving the energy and beam quality requirements with lasers based on these materials would be difficult and expensive. The difficulty is associated with the low saturation fluence (energy storage) of these materials. The saturation fluence and upper state lifetime limit the amount of energy which can be stored and extracted per unit area (volume) from a laser material. Pulse energies on the order of one J would require laser apertures of approximately 500 cm^2 for dye- and excimer-based systems. Solid-state lasers offer an increase in saturation fluence between two and three orders of magnitude greater than dye or excimer lasers. This makes possible the development of extremely compact, high-energy lasers based on solid-state lasing media. Unfortunately, the high saturation fluence of solid-state materials cannot be accessed directly with short-pulses due to limitations on peak power imposed by the nonlinear refractive index.

In principle, production of a 1-J, 1-ps laser pulse could be accomplished by producing a low-energy 1-ps, 1.053-μm laser pulse and directly amplifying it in a Nd:Glass laser chain. Because of the high saturation fluence, the final amplifier cross section could be less than $1\,\mathrm{cm}^2$. The extracted power density would be in excess of $1\,\mathrm{TW/cm}^2$, close to the damage threshold of most materials [Stuart 1995a]. A second, more severe limitation on the amplification chain is provided by the nonlinear index of refraction in the material [Siegman 1986]. Self-focusing and filamentation of the laser pulse can occur when the accumulated nonlinear phase (B-integral) exceeds π,

$$B = \frac{2\pi}{\lambda}\int_0^L n_2 I(t)dz = \frac{2\pi}{\lambda} n_2 I_{\mathrm{peak}} L \quad , \tag{B.33}$$

where n_2 is the nonlinear index of refraction and L is the length of the medium. The power density in a medium is thus limited by the B-integral. For a given length amplifier, the peak intensity must satisfy $I_{\mathrm{peak}} < \lambda/2\mathrm{n}_2 L$. For a 10-cm-long Nd:Glass laser amplifier, the peak intensity must be less than $2\,\mathrm{GW/cm}^2$. For a pulse length of 1 ps and an energy of 1 J, the cross-sectional area must be greater than $A_L > E/I_{\mathrm{peak}}\tau = 500\,\mathrm{cm}^2$, which is to be compared with the $> 1\,\mathrm{cm}^2$ estimated from the saturation fluence. One solution to keeping the B-integral small is to use a larger diameter amplifier. Unfortunately, the use of a large diameter amplifier for short-pulse amplification eliminates the advantage of solid-state media.

B.11.2 Chirped-Pulse Amplification

This problem can be overcome by the use of Chirped-Pulse Amplification (CPA) [Strickland 1985]. This technique allows smaller amplifiers to be used, which reduces the cost and increases the repetition rate. Chirped-Pulse Amplification circumvents self-focusing by temporally stretching the pulse before amplification and recompressing it afterwards. This reduces the B-integral in the lasing medium by the compression ratio, the ratio of the stretched to compressed pulse durations. While optical fibers and prisms can be used to stretch or compress a pulse, the simplest technique involves a grating pair. A grating pair can be used to impart a positive [Martinez 1987] or negative [Treacy 1969] chirp to a short pulse. The sign of the chirp is defined by the time derivative of the frequency.

The CPA concept is shown in Figure B-29. A short, low-energy pulse is generated in an oscillator. The pulse is then stretched by a factor greater than 1000 in grating pair. To obtain a positive chirp a telescope is used between the grating pairs to invert the sign of the natural negative chirp associated with grating dispersion. To limit the size, complexity and cost of the telescope, a positive chirp is generated when the beam size and energy are low (before amplification). The pulse is now long enough for safe amplification to high energy. The pulse is recompressed in a second, grating pair (no telescope), generating a high-energy, ultrashort laser pulse.

The initial grating pair imparts a phase delay proportional to the frequency. This produces a pulse which has different frequencies spread out in time (chirped pulse). The second grating pair imparts a phase delay which is the inverse of the first grating pair, thereby removing the chirp and recovering the short pulse. Ideally, with the amplifiers placed between the two sets of gratings, the only change in the chirped pulse is its amplitude and the temporal characteristics of the pulse at the input and output are the same. Unfortunately the amplifier can modify both the amplitude [Perry 1990a, Chuang 1993] and phase [Chuang 1993] structure of the pulse. The amplitude changes include gain narrowing and pulling [Perry 1990a]. The primary phase change is self-phase modulation of the chirped pulse in the amplifier chain [Chuang 1993, Perry 1994b]. All of these effects must be minimized in order to obtain optimal pulses upon compression.

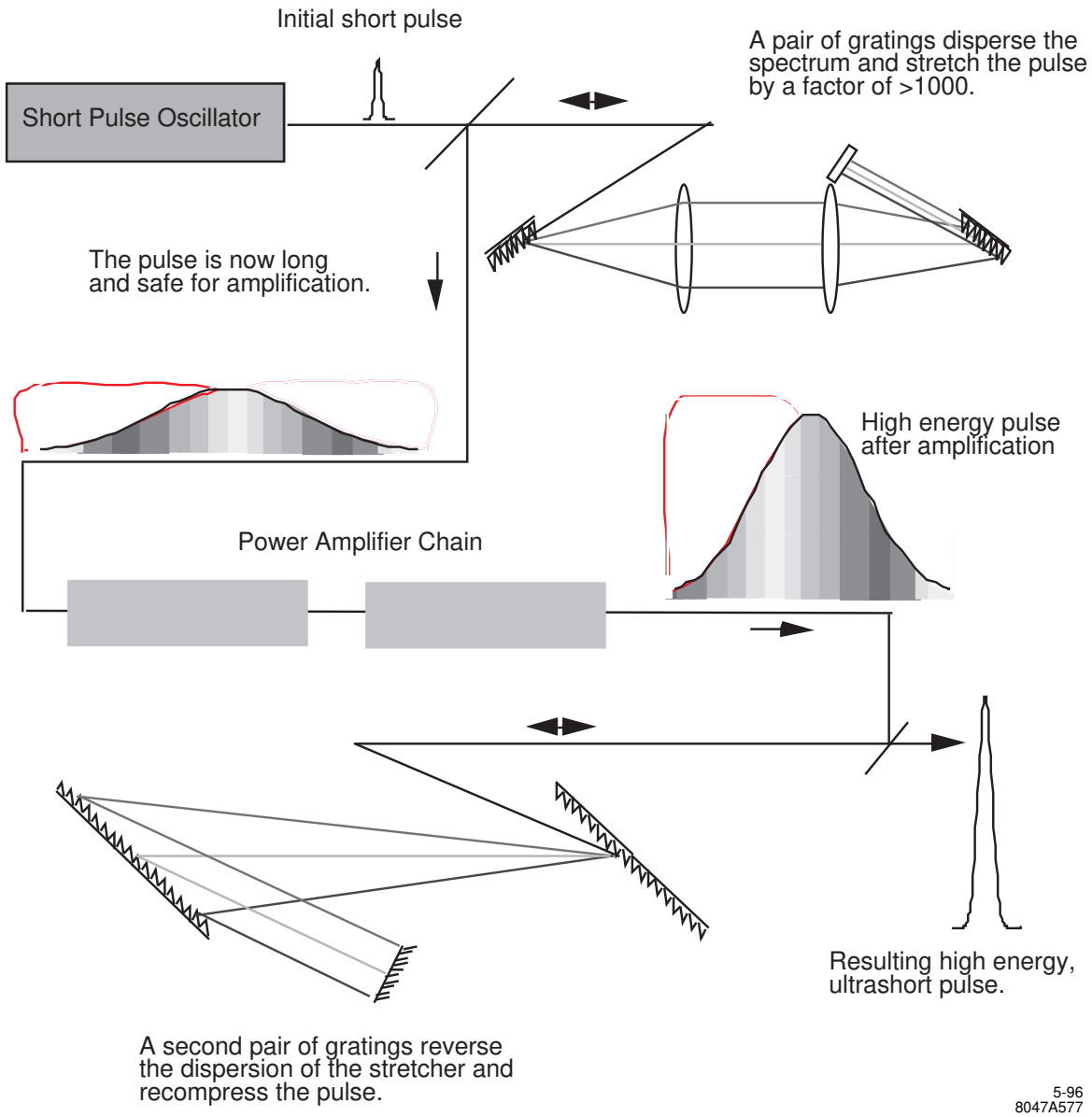

Figure B-29. *Chirped-pulse amplification concept.*

B.11.3 High-intensity, Short-pulse Laser Systems

There have been very dramatic advances in the technology and application of chirped-pulse amplification technology in the past five years [Perry 1994a]. Original CPA systems employed conventional mode-locked Nd:YAG or Nd:YLF oscillators producing transform-limited 50–100 ps pulses. The bandwidth necessary to achieve picosecond pulses was obtained by passing the 50–100-ps output of the oscillator through long (50–1000 m) lengths of single-mode fiber. Self-phase modulation in the fiber produced a chirped pulse with increased bandwidth. The pulse duration was increased from the original 50–100 ps by group-velocity dispersion in the fiber or the addition of a grating-pair pulse stretcher as mentioned previously. This method for obtaining stretched, chirped pulses has been rendered obsolete by the development of Kerr lens mode-locked oscillators which directly produce transform-limited 10–1000 fsec pulses. These pulses are then directly stretched in time by factors on the order of 10^4 by the grating stretcher. Elimination of the complex nonlinear interaction in the fiber is one of the many important advances which have led to the rapid and widespread acceptance of chirped-pulse amplification lasers.

The pulse exiting the stretcher has an energy of 0.10-1 nJ and a duration of ~1 ns. In the power amplifier section, the pulse must be amplified by a factor of 10^9 to the Joule level. This is typically achieved through the use of a multipass regenerative amplifier and a series of single or double pass amplifiers. In a regenerative amplifier, a pulse is switched into a cavity and makes multiple passes through an amplifier and is subsequently switched out. The regenerative amplifier brings the energy to the few milliJoule level (an increase of seven orders of magnitude) while the single and double pass amplifiers provide the remainder of the gain. Because of the losses inherent in the amplifiers, the total gain is of order 10^{10}–10^{11}.

After amplification, the pulse is compressed back to a short pulse by a pair of compression gratings. The damage threshold of these diffraction gratings is one of the most important limits on CPA lasers. The gratings must exhibit high damage threshold for both the long duration of the stretched pulse (ns) and the short duration of the compressed pulse (ps). Since the physical mechanism of optical damage changes from the nanosecond to picosecond regime [Stuart 1995a], producing high-damage threshold diffraction gratings is both a scientific and technical challenge. Commercially-available metallic gratings exhibit damage thresholds as high as 250 mJ/ cm^2 for ps pulses. Recent advances in grating technology [Boyd 1995] have increased the damage threshold of metallic gratings to over 400 mJ/ cm^2 for pulses in the range 0.1 to 50 ps. While these gratings do enable a factor of two increase in the peak power density achievable with most CPA systems, they will not be useful for the combined high average and high peak power requirement of the NLC. A new concept in diffraction gratings based on multilayer dielectric materials [Perry 1996] can, in principle, meet both the average power and peak power requirements of the NLC. These gratings have achieved a damage threshold of 600 mJ/ cm^2 for 100 fsec pulses [Perry 1995]. They should exhibit a significantly increased threshold for average power damage relative to thin-film metallic gratings, however this is yet to be demonstrated.

One must also be concerned about power density of the compressed pulse in transporting it to the interaction point. If the intensity exceeds 10^{12} W/ cm^2 it may cause plasma formation on solid surfaces [Stuart 1995a]. In addition, the nonlinear index of refraction of the pulse in air, in any windows, and in the focusing elements will destroy the beam quality of the pulse and make it impossible to focus. For example a 10^{12} W/ cm^2 pulse passing through a 1-cm-thick glass window ($n_2 = 3 \times 10 - 16\,\mathrm{cm}^2/\,\mathrm{W}$) the B-integral is 6π so that significant self-focusing would occur. The output diameter of the TW pulse must be large enough so that the cumulative B-integral in the transport line is limited to less than approximately π. This means that in practice, the intensity of the compressed pulse should be kept below 10^{11} W/ cm^2 before focusing, implying that the beam cross section must exceed 10 cm^2.

B.11.4 Synchronization and Repetition Rate

Two additional topics are important in the design of the laser system for a $\gamma\gamma$ collider. The laser beam must be synchronized to the electron beam to a fraction of the laser pulse duration and the repetition rate of the laser system must be matched to the repetition rate of the linac. The laser can by synchronized to the electron beam by driving the laser oscillator at a subharmonic of the linac rf. The phase relationship between the rf and the laser pulses can be maintained by electronic feedback [Rodwell 1986, Rodwell 1989]. Subpicosecond timing jitter has been demonstrated using these techniques [Rodwell 1986, Rodwell 1989]. A typical mode-locked oscillator operates with a driving frequency of 35–60 MHz, producing a 70–120-MHz pulse train. The length of the cavity is matched to driving frequency to produce the mode-locked, short duration, pulse train. The pulse train is detected with a fast photo-diode. The photo-diode signal is mixed with the input rf and error signal is used to phase shift the rf driving the mode-locker [Rodwell 1989]. It is important to note that to maintain the synchronization, the oscillator must be actively mode-locked. In addition, the path length of the laser after the oscillator, through the laser system and through the transport must be stable to less than the pulse duration, 0.3 mm for a 1-ps laser pulse.

B.11.5 1-ps, 1-J Laser System for Nonlinear QED Experiments

Recently a 0.5-Hz repetition rate, 1-μm, 1-ps, 1-J, chirped-pulse amplification (CPA) laser system has been demonstrated using a flashlamp-pumped, Nd:glass, zig-zag slab amplifier [Bamber 1995]. The system has been installed at the Stanford Linear Accelerator Center as part of the E-144 experiment to study nonlinear QED [Bula 1992] in collisions with 50-GeV electrons. With the exception of repetition rate and pulse format, many of the performance parameters required for $\gamma\gamma$ colliders are being examined with this system. In addition to demonstrating the laser energy, and pulse width, the jitter of the laser pulse with respect to the linac rf is currently less than 2 ps [Bamber 1995]. Compton-scattered gammas and recoil electrons due to multiphoton Compton scattering have been observed [Bula 1995]. Unfortunately, the average power of this laser system is four orders of magnitude less than required for the NLC $\gamma\gamma$ collider.

B.11.6 Average Power

As mentioned previously, the single pulse laser requirements for converting the NLC e^+e^- collider into a $\gamma\gamma$ or γe^- collider can be met by solid-state lasing materials. A number of different solid state materials are used for short-pulse, high-intensity, laser systems [Kmetec 1991, Perry 1991, Ditmire 1993, Beaudoin 1992, Salin 1991, White 1992] Both Ti:Sapphire [Salin 1991, Stuart 1995b] and Nd:Glass [Strickland 1985] have been used to generate high-intensity, ultrafast, laser pulses with wavelengths in excess of 1 μm. The advantage of using Ti:Sapphire is that its larger gain bandwidth allows shorter pulses to be generated and amplified, whereas a pure Nd:Glass system is limited to pulse durations of order 1 ps, which is sufficient for this application. The saturation fluence of Nd:Glass is approximately an order of magnitude higher than Ti:Sapphire, making Nd:Glass an attractive candidate for the NLC. Unfortunately, the thermal conductivity and thermal shock limit are low for glasses. As a result, although conventional Nd:glasses can meet the peak power requirements of the NLC, they cannot meet the average power requirements. The relevant properties of Nd:Glass are listed in Table B-10.

New glass hosts currently under development offer a nearly factor of two increase in the thermal shock limit. These glasses could, in principle, make possible a diode-pumped Nd:Glass based NLC laser. No laser has

Central wavelength	$1.053\,\mu$m
Gain bandwidth	$\sim$200 Å
Saturation fluence	$5\,\mathrm{J/cm^2}$
Nonlinear index, n_2	$6 \times 10^{16}\,\mathrm{cm^2/W}$

Table B-10. *Selected properties of Nd:phosphate glass lasing materials.*

yet been constructed from these advanced glasses. However, two kilowatt-class (long pulse) lasers are under development at LLNL utilizing these new glasses. Performance data from these lasers will be invaluable in analyzing the suitability of glass-based systems for the NLC.

In addition to developments in laser glass, recent advances in crystal hosts are also encouraging for NLC options. New crystals which have been "engineered" for diode-pumping and high average power operation are now emerging. One attractive candidate is Yb:S-FAP. This is a fluroapatite crystal host for the Yb lasing ion. The material functions well as a laser near 1 μm and has sufficient bandwidth to support pulses of 2–5 ps in duration. It has thermo-mechanical properties which are substantially better than even the advanced glasses. Furthermore, it has a long upper-state lifetime ($\approx$1 ms) and an absorption band at 900 nm which make it nearly ideal for diode pumping with efficient AlGaAs diodes. The Yb:S-FAP crystal can not yet be grown in sufficient sizes to meet NLC requirements. However, a large amount of effort is currently being devoted to further developing S-FAP and related crystal hosts. It is reasonable to expect that large scale crystals would be available within one to two years.

In short, there are several options for meeting the average power requirements of the NLC. These options include: 1) direct, diode-pumped Nd:Glass based lasers incorporating advanced athermal glass, 2) direct, diode-pumped, broad-bandwidth crystals (*e.g.,* Yb:S-FAP or others) and, 3) two-stage laser-pumped lasers such as a long pulse ($\approx$10 ns) neodymium based laser pumping a short-pulse Ti:Sapphire laser. We have not yet performed an optimization study for the NLC laser which would compare the performance and cost of these various options. Such a study would be part of the conceptual design of the NLC $\gamma\gamma$ collider.

In addition to requiring advances in high average power laser materials, advances in diode laser technology are also required to meet the NLC specifications. However, there are major efforts on advancing diode laser technology already underway as part of both military- and civilian-led projects. High average power diode laser arrays which would meet the requirements of the NLC are already under development at LLNL and elsewhere. Current high peak power diode arrays have generated 1.45-kW average power [Beach 1994]. The continued development of diode laser technology and the associated thermo-mechanical systems will be only moderately influenced by the approval of the NLC. Instead, the NLC will reap the benefit of substantial development effort which is expected to produce diode packages which can meet the NLC requirements well in advance of the NLC construction schedule.

B.11.7 NLC Laser Concept

The proposed laser system for the NLC $\gamma\gamma$ option consists of two $\sim$16-kW laser systems built out of 1-kW unit cells. A schematic of the unit cell is shown in Figure B-30. All of the cells are fed by a single, phase-stabilized oscillator, ensuring synchronization of all of the laser pulses with the electron beam. Each of the unit cells consists of a series of diode-pumped, solid-state, laser amplifiers. The pulses are subsequently compressed in a grating pair and stacked into a single pulse train.

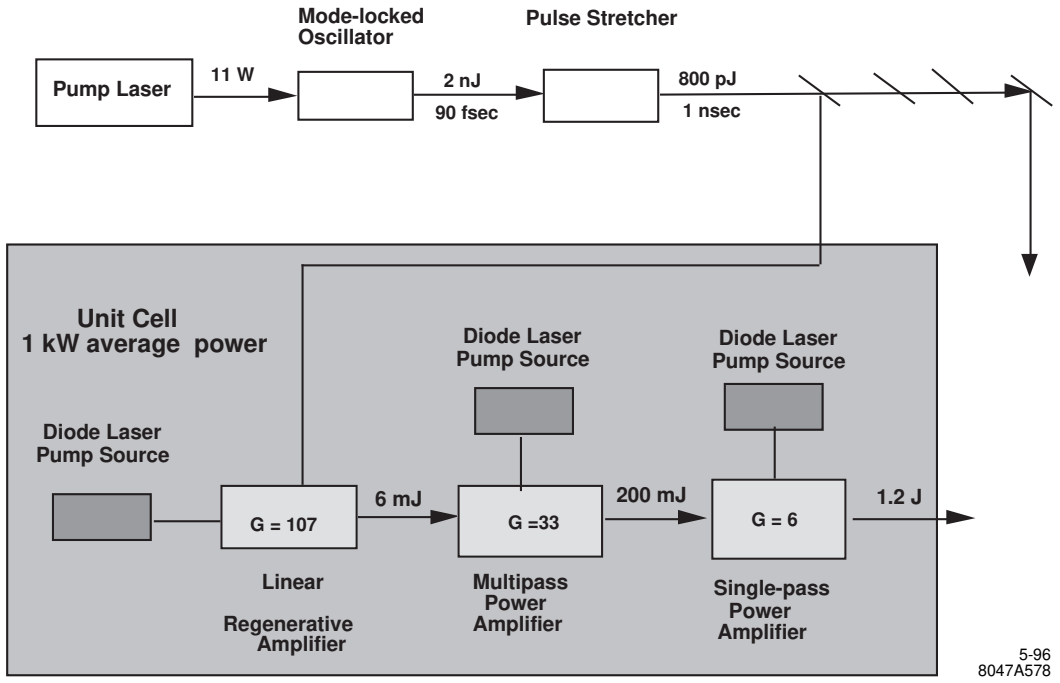

Figure B-30. *1-kW average power unit cell.*

Pulse stacking from individual unit cells into a single pulse train occurs via polarization switching as shown in Figure B-31. The output of a single unit cell is a small pulse train which is s-polarized (linearly polarized out of the paper in the figure). These pulses are reflected along the primary axis by a thin film polarizer. These polarizers are designed to reflect s-polarized light with greater than 99% efficiency while simultaneously transmitting p-polarized light with similar efficiency. Light from the first unit cell passes through a Pockels cell which has an applied voltage sufficient to provide a half-wave retardation. This rotates the polarization of the pulse 90° from s-polarization to p-polarization (linearly polarized in the plane of the paper). This p-polarized light now passes through the next thin film polarizer. The s-polarized pulses from the next unit cell are reflected from the thin-film polarizer. Combined with the pulses from the first unit cell, we have two sets of orthogonally polarized pulses incident on the next Pockels cell. The Pockels cell is initially held at ground while the p-polarized pulses from the first unit cell pass. After these pulses pass, the Pockels cell voltage is switched to half-wave voltage. The s-polarized pulses from the second unit cell are rotated to p-polarization upon transmission through the Pockels cell. The result is now a combined train of p-polarized pulses along the same optical axis. The procedure is repeated for each subsequent cell. In this scheme, the pulse-compression gratings probably should be placed after the pulse stacking so that all of the pulses will be compressed in the same grating pair and to keep the B-integral down.

B.11.8 A Ring Configuration for Multiplexing and Polarization Control

The baseline design would be to use each pulse once, with a single pass through a Pockels cell for polarization control. However, we will explore during the design the possibilities of re-using the pulse, thus significantly reducing the average laser power requirements, and hence cost. This was discussed in Section B.8.4. Here we

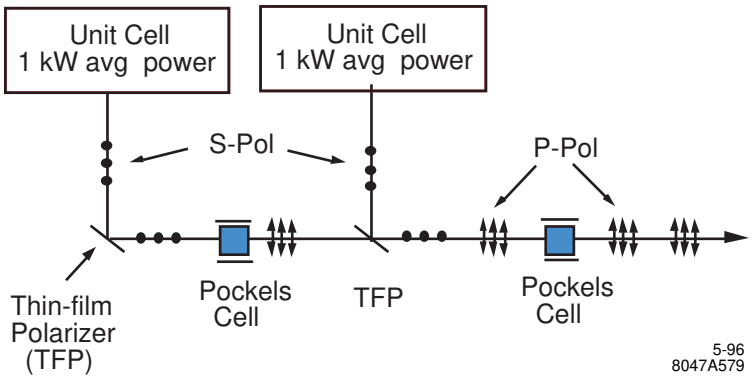

Figure B-31. *Pulse stacking/combination from individual unit cells onto a single optical axis is accomplished with electro-optic polarization switching.*

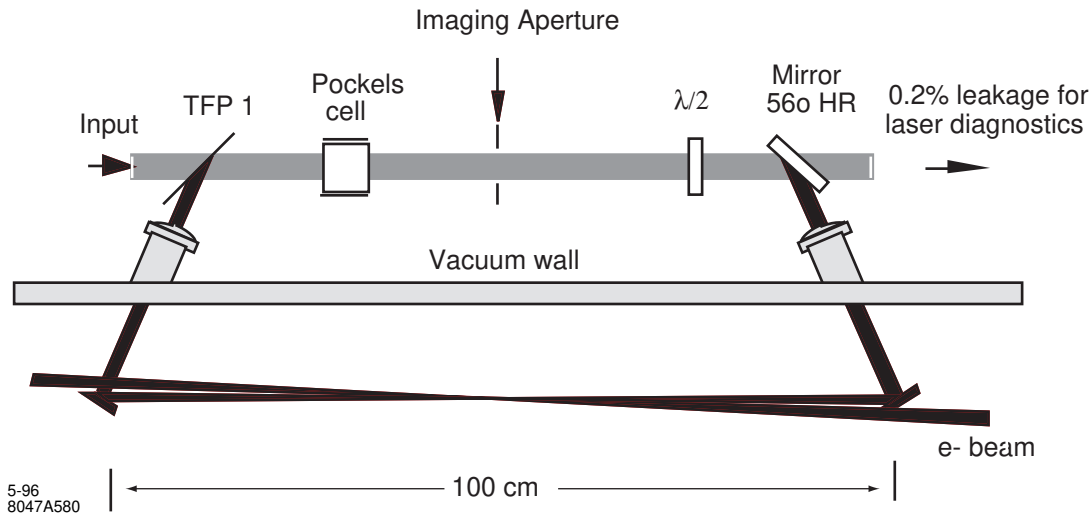

Figure B-32. *Relay imaged ring regenerative cavity.*

discuss in detail an example of such schemes based on a ring regenerative device first demonstrated at LLNL in 1990 [Perry 1990b]. The regenerative ring (Figure B-32) is a photon recirculator which is based on the original ring regenerative amplifier concept. The pulse is initially p-polarized (from the pulse stacker) and enters the cavity through a thin-film polarizer, TFP 1. The Pockels cell is initially at ground providing no phase retardation. The half-wave plate ($\lambda/2$) rotates the polarization 90° (now s-polarized, out of the plane of the paper). The s-polarized pulse reflects off of the high reflector and enters the vacuum chamber through a window. The laser beam is directed to the IR in the manner described in Section B.8.1 and directed out of the IR through a second window, before striking the original polarizer (TFP 1). The s-polarized pulse now reflects off of the polarizer and passes on its original path through the Pockels cell. However, the Pockels cell is now switched to half-wave voltage providing a 180° phase retardation which rotates the polarization back to the plane of the paper (p-polarization). The pulse is now trapped in the cavity and retraces its original path. Beam quality (focusabilty) is maintained by constructing the cavity either as a relay-imaged ring or as a TEM_{00} resonator.

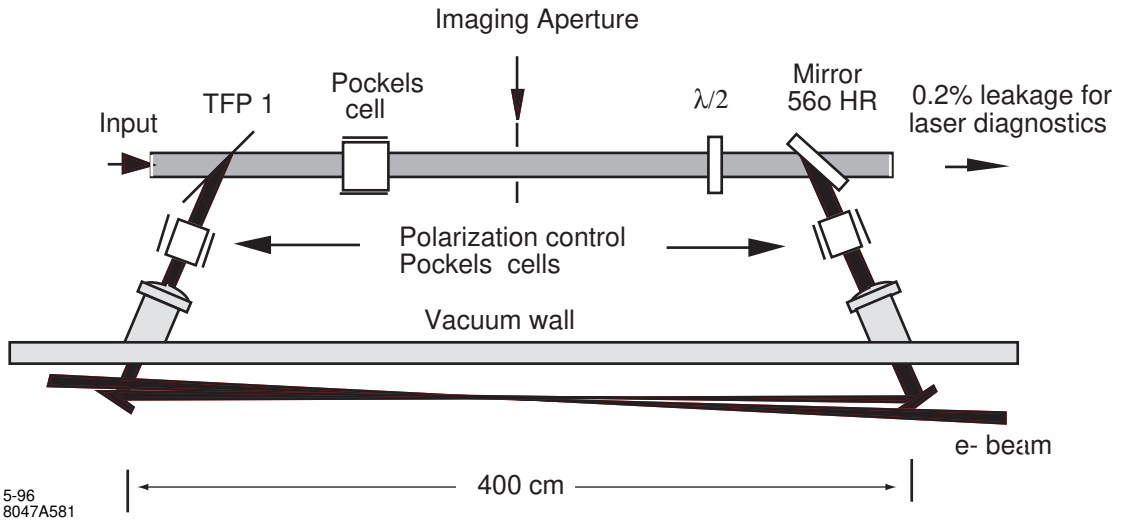

Figure B-33. *Laser photon recirculator and polarization control at the interaction point.*

The ring is constructed such that its cavity length exactly matches a multiple of the separation between microbunches of the electron beam. In this case, each time the laser pulse traverses the ring, it strikes a new electron microbunch at the IP. This effectively multiplies the repetition rate of the laser by the number of passes around the ring. A typical cavity round-trip time is 10 ns corresponding to a 3-m cavity. However, this can easily be adjusted to match the optimum electron bunch spacing as dictated by the rf accelerator. We have constructed rings for a round-trip time as short as 3 ns to over 30 ns.

The pulse will slowly decay in energy with each pass of the ring (ring down). The rate of decay is determined by the optical quality and reflectivity of the cavity optics. We have achieved a net cavity loss as low as 4% in a ring cavity of a design similar to Figure B-32. With extremely high quality optics as are commonly used in the Atomic Vapor Laser Isotope Separation (AVLIS) program, we should be able to achieve a cavity loss lower than 2%. With a 2% loss, 80 round trips drops the pulse energy to 20% of the original input. Even with only moderate quality optics, we routinely achieve 70 round trips in existing systems.

For the picosecond pulses envisioned for the $\gamma\gamma$ collider, self-focusing and self-phase modulation will limit the number of round-trips achievable for the standard design of Figure B-32. These problems can be overcome by incorporating a passive pulse stretcher/compressor into the ring and/or using all reflective focusing of the beam to the interaction point. Optimization of these designs and the effect on system performance is an important development task.

B.11.9 Polarization Control at the Interaction Point

Helicity control is a unique requirement of the laser system for the $\gamma\gamma$ collider. The desire to change the polarization from linear to circular and back on either a macrobunch or several macrobunch time scale in order to investigate the helicity dependence of various $\gamma\gamma$ reactions is a complicating factor to the laser design. The strong polarization dependence of the laser amplifier section, pulse compressor and pulse stacker demand that all helicity manipulation be performed after the pulse has left these elements. The use of the

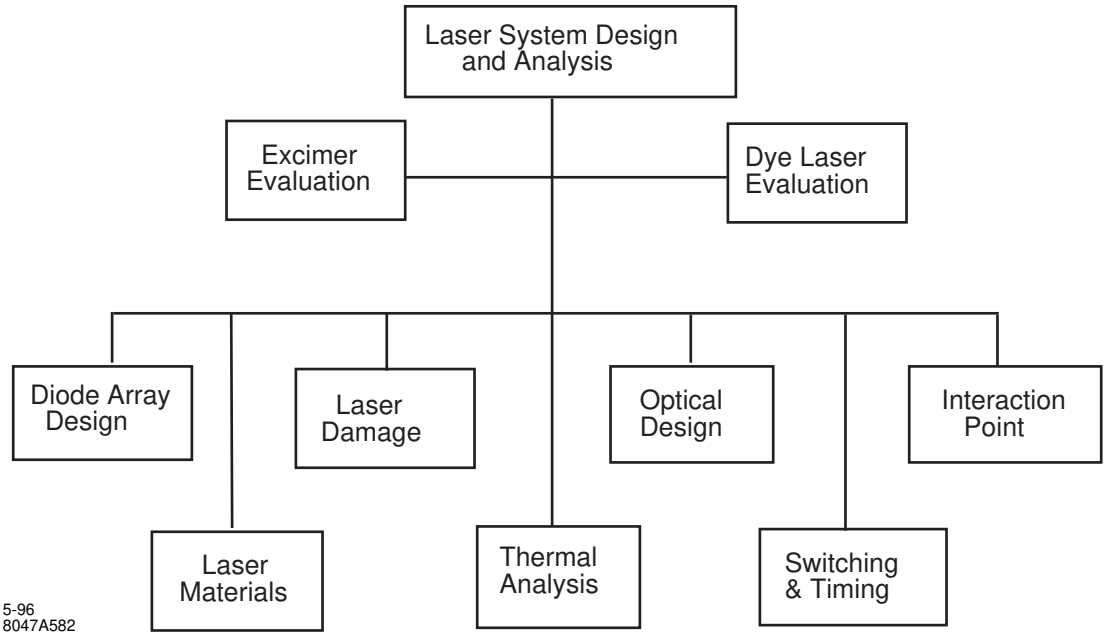

Figure B-34. *Conceptual design organization for NLC $\gamma\gamma$ collider laser system.*

photon recirculator of Figure B-32 is amenable to polarization control by addition of two additional Pockels cells as shown in Figure B-33. Before entering the vacuum chamber, the pulse passes through a Pockels cell which is either held at ground to produce no phase retardation and leaves the polarization unchanged (linearly polarized) or is switched to quarter-wave voltage to produce circularly polarized light. This Pockels cell can be easily switched at a 5-ms repetition rate (180 Hz) to enable switching between linear and circular polarization at the interaction region on alternating macropulses.

The ring scheme for reusing the laser beam and polarization control requires an extensive R&D. It should be demonstrated that there is the necessary space around the detector and that the B-integral in the Pockels cells, or the large cross-sectional areas of the cells, does not pose a problem.

These laser concepts should be considered preliminary at this time. Substantial conceptual design and optimization is yet to be done. A schematic of the conceptual design organization and issues to be addressed is shown in Figure B-34.

B.11.10 Conclusion

In summary, many of the technological advances required for the NLC $\gamma\gamma$ option have recently been achieved. The $\gamma\gamma$ collider portion of the NLC benefits substantially from the large national efforts which are devoted to the development of high peak power and high average power laser systems. While substantial design, optimization and development still needs to be done, our preliminary study suggests that within the next few years, many of the required laser components will be demonstrated and a prototype NLC laser module could be developed.

B.12 Free-Electron Lasers

Free-electron lasers (FEL) are another option for photon colliders, and they are especially interesting for higher energy colliders, where the required wavelength of the laser is longer than $\sim$1 μm, for which solid-state lasers do not presently exist. Several schemes have been proposed based on different combinations of FEL oscillators, amplifiers, and optical switching techniques. A scheme based on the chirped pulse amplification and compression, similar to the technique used in solid state lasers but replacing the amplifier with an FEL driven by an induction linac, is another attractive option.

B.12.1 An FEL Scheme Using Induction Linac and Chirped Pulse Amplification Technique

With the usual high-gain FEL amplifiers, it is difficult to produce the laser pulses of the characteristics outlined in this section. This can be readily understood if we note that the saturation power in high-gain FELs is given approximately by $P_{\rm sat} \sim \rho P_{\rm beam}$ where ρ is the FEL scaling parameter [Bonifacio 1984] and $P_{\rm beam}$ is the electron beam power; $P_{\rm beam} = EI$, where E and I are the beam energy and current respectively. Suppose we require the pulse energy $A = P_{\rm sat}\tau$ to be about 1 J. Assuming $\rho \sim 10^{-2}$, $I \sim 1$ kA, and $\tau = 2$ ps, we find that E needs to be about 50 GeV. On the other hand, producing $\lambda = 1\,\mu$mFEL with such a high-energy electron beam requires a strong and long (100-m) wiggler magnet.

The discussion above also points to the solution of the problem. Namely if the pulse length were much larger, about 1 ns, then the required electron beam energy becomes $E = 100$ MeV, which is quite reasonable for a 1-μm FEL. Thus the solution is to amplify the 1-ns pulse and later compress it to a few ps. A laser pulse can be compressed if it is chirped. Thus we are led to the idea of employing the chirped pulse amplification technique to FEL [Telnov 1991] extensively developed for solid-state lasers [Perry 1994a].

The scheme is schematically illustrated in Figure B-35. A solid-state laser produces a sequence of 1.8-ps, 0.14-mJ micropulses, with the same time structure as the collider beam, with an average power of 2.3 W. The micropulses are stretched (and hence chirped) to slightly less than 1.4 ns by means of a dispersive element schematically represented by a grating pair in the figure. The resulting optical beam which becomes amplified in a high-gain FEL driven by an induction linac producing $1.4 \times 90 = 130$-ns-long electron pulses at a 180-Hz repetition rate. The energy of each induction linac pulse may be modulated to match the chirped optical beam as indicated. Each amplified micropulse contains a few Joules of energy. The micropulses are compressed by another dispersive element to 1.8 ps. Of course, these optical components must designed to withstand high peak power (as is already true in SS laser compression systems) and high average power.

The electron beam and wiggler parameters required are shown in Table B-11.

A design of the induction linac producing the required electron beams is challenging but within the current state-of-the-art, and will be discussed in Section 9.2.3. The FEL consists of two sections, a 7.2-m-long uniform section in which the power gain length is about 1 m, and the input peak power of 100 kW is amplified to 140 MW. It is followed by a 7.2-m-long tapered section to further amplify the power to 1.6 GW. Thus, the energy contained in each micropulse is 1.6 GW $\times$ 1.4 ns $\simeq$ 2.24 J, which is larger than 1 J required for a conversion efficiency of 68%.

A scheme to amplify chirped pulses, similar to the one discussed here, but based on a regenerative FEL amplifier driven by an rf linac, was independently proposed recently by an LANL group [Chan 1995]. The

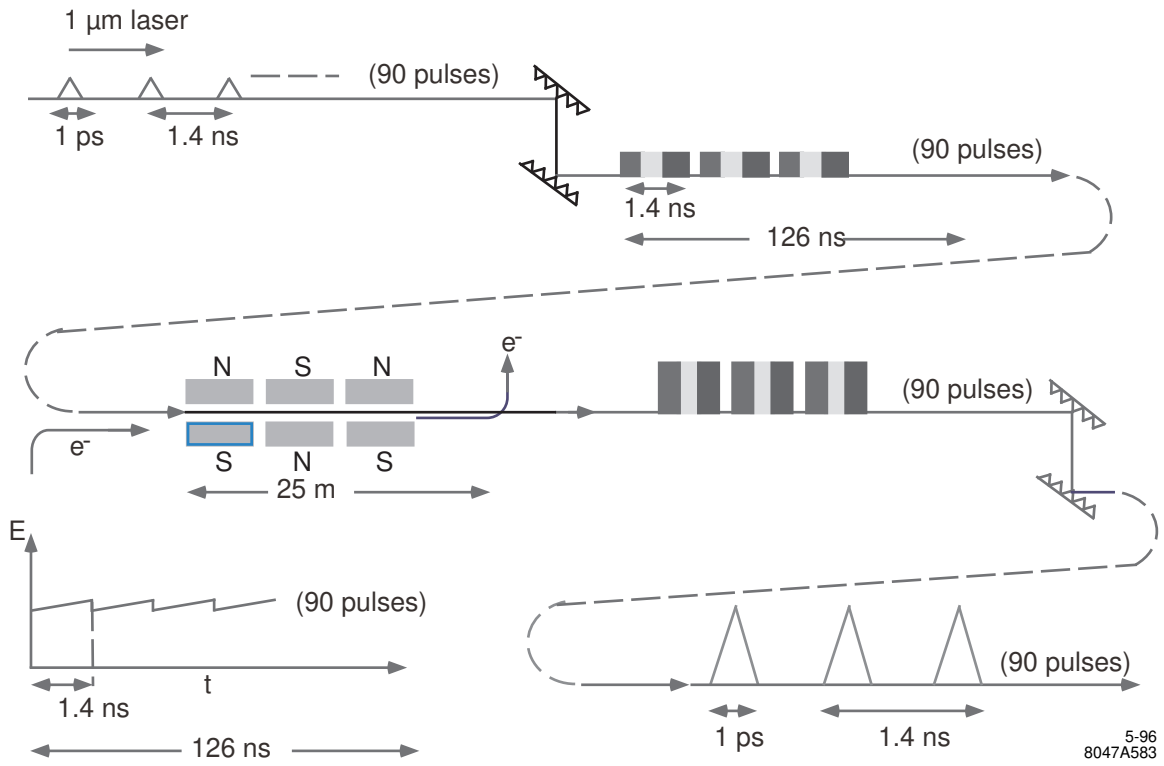

Figure B-35. *FEL pulse stretching/amplification/compressing scheme.*

Electron Beam Parameters:	
I	1 kA
E	100 MeV
$\Delta E/E$	10^{-3}
Rms normalized emittance (ϵ_N)	50×10^{-6} m-rad
Betatron wavelength (λ_β)	11.3 m
Undulator Parameters:	
λ_W	4.0 cm
K	1.4
Length of uniform section	7.2 m
Length of tapered section	10 m
Micropulse FEL Power:	
Input power	100 kW
Power after uniform section	140 MW(power gain length = 1 m)
Power after tapered section	1.6 GW
Energy per micropulse	1.6 GW × 1.4 ns = 2.24 J

Table B-11. *Parameters for an FEL Pulse Compression Scheme.*

scheme requires the use of intracavity optical switches operating in a high-power environment and focusing mirrors operating at a peak power density of 1 GW/ cm^2.

B.12.2 Chirping Requirement and Tolerance

The compression of the input pulse with electric field amplitude $E_i(t)$ to the output amplitude $E_f(t)$ can be represented by the linear transformation

$$\begin{aligned} E_f(t) &= \frac{1}{\sqrt{2\pi}} \int G(t-t')E_i(t')dt', \\ G(t) &= \frac{1}{\sqrt{\tilde{\mu}}} \exp\left(\frac{it^2\tilde{\mu}}{2} - i\omega_0 t\right) \end{aligned} \tag{B.34}$$

where $1/\tilde{\mu}$ is the time delay per unit frequency interval introduced by the dispersive element. An input chirped pulse may be represented by

$$E_i(t) = \exp\left(-i\left[\omega_0 t + \frac{\mu}{2}t^2\right] - \frac{t^2}{4\sigma_{\tau i}^2}\right) \quad , \tag{B.35}$$

where $\sigma_{\tau i}$ is the rms pulse length, and μ is the frequency change per unit time interval (chirping rate). Inserting Eq. B.35 into Eq. B.34, we find that the output pulse is also Gaussian, with the rms pulse length

$$\sigma_{\tau f} = \sqrt{\frac{1}{4\sigma_{\tau i}^2\tilde{\mu}^2} + \sigma_{\tau i}^2\left(\frac{\mu}{\tilde{\mu}} - 1\right)^2}. \tag{B.36}$$

Thus, if the grating is designed so that $\tilde{\mu} = \mu$, then $\sigma_{\tau f} = 1/2\mu\sigma_{\tau i}$. If $\sigma_{\tau i} = 1.4$ nsand $\sigma_{\tau f} = 1.8$ ps, then we require $\tilde{\mu} = 2 \times 10^{20}/\mathrm{s}^2$. The total frequency chirping over the uncompressed pulse is $\Delta\omega \equiv= 2\mu\sigma_{\tau i} = 5.6 \times 10^{11}/$ or for 1 μm radiation $\Delta\omega/\omega = 2.8 \times 10^{-4}$. This is well within the gain bandwidth of the FEL. Therefore, it may not be necessary to modulate the electron beam energy.

There may be jitter introduced by the FEL amplification process. The jitter must be small so that $\sigma_{\tau i}^2(\mu/\tilde{\mu} - 1)^2 \ll 1/4\sigma_{\tau i}^2\tilde{\mu}^2$ or $\mu - \tilde{\mu} \ll 1/2\sigma_{\tau i}^2$. Thus the frequency error over the pulse must satisfy $\Delta\omega/\omega \ll 1/\omega\sigma_{\tau i} = 3.8 \times 10^{-7}$. To see the implication of the above requirement, we consider a high gain FEL in the exponential growth regime. The phase error due to a fluctuation $\Delta\rho$ in ρ is $\Delta\phi \sim 2\pi\Delta\rho L_W/\lambda_W$, where L_W is the length of the wiggler. Since ρ is proportional to $I^{1/3}/\gamma$, we have $\Delta\rho/\rho \sim (\Delta I/3I - \Delta\gamma/\gamma)$. Hence, $\Delta\omega/\omega = \Delta\phi/\omega\sigma_{\tau i} = (\lambda/c\sigma_{\tau i})(L_W/\lambda_W)\rho(\Delta I/3I - \Delta\gamma/\gamma)$. Taking $L_W = 20$m, $\lambda_W = 4$ cm, λ =1 μm, $\rho = 2 \times 10^{-3}$, we obtain $\Delta\omega/\omega \sim 10^{-5}(\delta I/3I - \Delta\gamma/\gamma)$. Therefore, if the fluctuations in $\Delta I/I$ and $\Delta\gamma/\gamma$ are a few percent, then the compression requirement is satisfied. Such a tolerance should be achievable.

B.12.3 Induction Linac Driver

The $\gamma\gamma$ induction linac driver beam parameters required for driving the FEL are listed in Table B-12 with beam parameters of several other induction linacs. The ATA was used to drive the Paladin FEL [Orzechowski 1990], the ETA II was used to drive the Intense Microwave Prototype (IMP) FEL [Allen 1992], and the TBNLC is a proposed induction accelerator driven relativistic klystron for powering the NLC [Caporaso 1995]. The $\gamma\gamma$ Induction Linac Driver will require significant improvement in the areas of beam

Parameter	$\gamma\gamma$ Induction Linac Driver	ATA (Paladin)	ETA II (IMP)	TBNLC Injector/main
E_b (MeV)	100	45	7	$2.8/10^a$
I_b (kA)	1	0.8	2.4	1.2/0.6
ε_N(edge)	300	650(300 A)	900	400/800
(mm-mr)		1,116 (2.7 kA)		
$B_N(A/m^2 - r^2)$	2.2×10^9	1.4×10^8 (300 A) 4.6×10^6 (2.7 kA)	4×10^8 (1.5 kA) (2.5 MeV)	$1.5 \times 10^9/2 \times 10^8$
Flattop	150	>20	40	200
Pulse Length (ns)				
ΔE/E	$\pm$ 0.1%		$\pm$1%	$\pm$0.2%

[a] Final beam energy without rf power extraction would be 90 MeV.

Table B-12. *Comparison of the $\gamma\gamma$ Induction Linac Driver to other induction accelerators.*

brightness (B_N) and energy flatness (ΔE/E) with respect to measured values for ATA or ETA II. Note that the electron beam of the last induction linac built at LLNL (ETA II) had a measured brightness 1/5 of that required. ETA II, however, had much better beam quality than the earlier ATA. Thus, although induction linacs built to date have not produced the beam quality required for the $\gamma\gamma$ induction linac driver, it is reasonable to expect that improved computer modeling of induction injectors will lead to designs with higher beam brightness meeting the FEL requirements for $\gamma\gamma$ colliders. The use of photocathodes in induction injectors could also be explored to achieve the required beam quality.

ATA and ETA II represent about 10-year-old induction accelerator technology. A program to construct a prototype induction linac for the TBNLC is in progress at LBNL. Simulations have shown that the induction linac injector can produce a B_N of about $1.5 \times 10^9\ A/m^2 - r^2$ for a 1.2-kA, 2.8-MeV beam. A demonstration of this brightness will be significant to the $\gamma\gamma$ induction linac driver as its injector represents the largest source of brightness degradation (emittance growth). Energy regulation to achieve a ΔE/E of $\pm$0.2% is planned for the prototype, and will determine the feasibility of a ΔE/E of $\pm$0.1% for the $\gamma\gamma$ driver.

Beam energy is primarily a cost issue. Induction modules can be added to provide the desired beam energy. However, as the length of the induction linac increases, transverse instability of the beam motion can become a difficulty. The beam tube radius of the induction cells can be increased to lower the growth in the transverse instability as described below. The larger inner radius will lead to a larger induction core volume increasing the core cost and reducing efficiency. The transverse instability mechanism is well understood for induction linacs [Capporaso]. Assuming constant acceleration ($\gamma = \gamma_0 + \lambda z$) and a solenoid focusing field proportional to the beam energy, a figure of merit for transverse instability is given by the product of the betatron phase advance (φ_β) times the number of e-folds (f_e) of gain:

$$\varphi_\beta f_e = \frac{2}{\lambda^2}\frac{(\omega_0 Z_\perp)}{L_g}\frac{I}{I_0}\left(\sqrt{\gamma_f} - \sqrt{\gamma_0}\right)^2 \quad , \tag{B.37}$$

where I is the beam current, $I_0 = 17.03$ kA, L_g is the separation between induction module gaps, $(\omega_0 Z_\perp)$ is the transverse impedance of the gaps, and λ is the gap energy increase ($\Delta\gamma$) divided by L_g. The transverse impedance scales approximately as:

$$(\omega_0 Z_\perp) = \eta\frac{4w}{b^2} \quad , \tag{B.38}$$

where w is the gap width, b is the inner radius, and η is a design factor of order unity ($\eta = 1.3$ for ATA).

Three e-folds of gain ($f_e = 3$) in an accelerator length of about 16 betatron wavelengths ($\varphi_\beta = 100$) would be a reasonably conservative design for controlling transverse instability. Assuming a maximum field stress in the gap of 100 kV/ cm ($\Delta\gamma = 0.196$ and w = 1.0 cm), gap spacing of 30.0 cm, injector voltage of 1.5 MV, and $\eta = 0.7$ ("good" design), Eqs. B.37 and B.38 are used to find b $\geq$ 11.2 cm. The focusing field will increase from 183 G at 1.5 MeV to 1.3 kg at 100 MeV. The linac will have approximately 1,000 induction modules and be over 300 m in length.

Induction cells with 11-cm beam pipe radius will have about twice the core volume of the TBNLC cells (pipe radius = 5 cm). This volume increase will not only lead to added cost for core material, but also require an appreciable increase in the number of pulse power units than that of the TBNLC design. Although the design parameters have not been optimized, the $\gamma\gamma$ Induction Linac Driver is expected to cost significantly more per unit length than the TBNLC induction linac and have lower wall plug to beam power conversion efficiency.

References

[Allen 1992] S.L. Allen and E.T. Scharlemann, "The ETA II Linear Induction Accelerator and IM Wiggler: A High-Average-Power Millimeter-Wave Free-Electron-Laser for Plasma Heating", *Proc. 9th Intl. Conf. on High Power Part. Beams*, Washington, DC, (1992).

[Arutyunian 1963] F.R. Arutyunian and V.A. Tumanian, *Phys. Lett.* **4** 176 (1963); R. H. Milburn, *Phys. Rev. Lett.* **10** 75 (1963).

[Asaka 1995] T. Asaka, N. Maekawa, T. Moroi, Y. Shobuda, Y. Sumino, TU-483, May 1995, talk given at 5th Workshop on Japan Linear Collider (JLC), Tsukuba, Japan, 16-17 Feb 1995; e-Print Archive: hep-ph/9505371.

[Baillargeon 1995] M. Baillargeon, G. Belanger, and F.Boudjema, *Phys. Rev.* **D51**, 4712 (1995).

[Balakin 1994] V. Balakin, A. Sery, *Proc. of Workshop on Gamma-Gamma Colliders*, Berkeley CA, USA, (1994); *Nucl. Instr. Methods A* **355** 157 (1995).

[Bamber 1995] C. Bamber, T. Blalock, S. Boege, J. Kelly, T. Kotseroglou, A.C. Melissinos, D.D. Meyerhofer, W. Ragg, and M. Shoup III, *Opt. Lett.* submitted (1995).

[Barklow 1990] T. Barklow, SLAC–PUB–5364 (1990).

[Barletta 1993] W. Barletta *et al.*, (Plasma Lens Collaboration), "Proposal for Plasma Lens Experiments at the Final Focus Test Beam", SLAC–Proposal–E–150 (April 1993).

[Beach 1994] R. Beach *et al.,* Conf. on Lasers and Electro-optics (CLEO), Anaheim, CA (1994).

[Beaudoin 1992] Y. Beaudoin, C.Y. Chien, J.S. Coe, J.L. Tapi, and G. Mourou, *Opt. Lett.* **17** 865–867 (1992).

[Ben-Menachem 1993] S. Ben-Menachem and P. Chen, SLAC–436, in *Proc. of the 5th Int. Workshop on Next-Generation Linear Colliders*, 426 (1993).

[Berestetskii 1982] V.B. Berestetskii, E.M. Lifshitz, L.P. Pitaevskii, *Quantum Electrodynamics*, Section 101 (Pergamon Press 1982).

[Berkeley 1995] *Proc. of Workshop on Gamma-Gamma Colliders*, Berkeley CA, USA, 1994; *Nucl. Instr. Methods A* **355**, 1–194 (1995).

[Billhardt 1993] F. Billhardt, M. Kalashnikov, P.V. Nickles, and I. Will, *Opt. Commun.* **98**, 99–104 (1993).

[Bonifacio 1984] R. Bonifacio, C. Pellegrini and L.M. Narducci, *Opt. Commun.* **50**, 373 (1984).

[Borden 1993a] D.L. Borden, plenary talk presented at Workshop on Physics and Experiments with Linear e^+e^- Colliders, Waikoloa, Hawaii, 26–30 April 1993, ed. F.A. Harris, S.L. Olsen, S. Pakvasa, and X. Tata, (World Scientific, Singapore, 1993).

[Borden 1993b] D.L. Borden, D.A. Bauer, D.O. Caldwell, *Phys. Rev.* **D48**, 4018 (1993).

[Borden 1994] D.L. Borden, V.A. Khoze, W.J. Stirling, J. Ohnemus, *Phys. Rev.* **D50**, 4499 (1994).

[Boyd 1995] R.D. Boyd, J.A. Britten, D.E. Decker, B.W. Shore, B.C. Stuart, M.D. Perry, and L. Li, *Appl. Opt.* **34**, 1697–1706 (1995).

[Brodksy 1994] S. Brodsky, P. Zerwas, *Proc. of Workshop on Gamma-Gamma Colliders*, Berkeley CA, USA (1994); *Nucl. Instr. Methods A* **355**, 19 (1995).

[Bula 1992] C. Bula *et al.,* Study of QED at Critical Field Strength at SLAC, E-144 proposal (1992).

[Bula 1995] C. Bula *et al., Phys. Rev. Lett.* , submitted (1995).

[CAIN] CAIN (Conglomérat d'ABEL et d'Interactions Non-Linéaires) being developed by P. Chen, G. Horton-Smith, T. Ohgaki, A. Spitkovsky, A.W. Weidemann, and K. Yokoya.

[Caporaso 1995] "Relativistic-Klystron Two-Beam Accelerator Based Power Source for a 1-TeV Center-of-Mass Next Linear Collider: Preliminary Design Reports", LBID–2085 and UCRL–ID–119906, (Feb. 1995); G.J. Caporaso and A.G. Cole, "High Current Electron Transport", in *AIP Conference Proceedings* 249, The Physics of Particle Accelerators, eds. M. Month and M. Diens, AIP, NY, 1662–1672.

[Capporaso] G.J. Caporaso and A.G. Cole, "High Current Electron Transport", in AIP Conference Proceedings 249, The Physics of Particle Accelerators, eds. M. Month and M. Diens, 1662–1672, (AIP, NY).

[Chan 1995] K.C.D. Chan, J.C. Goldstein, D.C. Nguyen, and H. Tekeda, "A Chirped Pulse Regenerative - Amplifier FEL for the Gamma-Gamma Collider", LANL preprint, LA–UR–95–1502, presented at the 1995 Part. Acc. Conf., Dallas, TX (1995).

[Chanowitz 1994] M. Chanowitz, *Proc. of Workshop on Gamma-Gamma Colliders*, Berkeley CA, USA (1994); *Nucl. Instr. Methods A* **355** 42 (1995).

[Chen 1989] P. Chen, V. Telnov, *Phys. Rev. Lett.* **63** 1796 (1989).

[Chen 1995a] P. Chen, G. Horton-Smith, T. Ohgaki, A.W. Weidemann, K. Yokoya, *Nucl. Instr. and Methods* **A35** 107 (1995).

[Chen 1995b] P. Chen, D. Bullock and D. Yu, *Proc. of Workshop on Gamma-Gamma Colliders*, Berkeley CA, USA, (1994); *Nucl. Instr. Methods A* **355** 130 (1995).

[Cheung 1994] Kingman Cheung, *Phys. Rev.* **D50**, 4290 (1994).

[Chien 1995] C.Y. Chien, G. Korn, J.S. Coe, J. Squier, G. Mourou, and R.S. Craxton, *Opt. Lett.* 20, 353-355 (1995).

[Chuang 1991] Y.-H. Chuang, D.D. Meyerhofer, S. Augst, H. Chen, J. Peatross, and S. Uchida, *J. Opt. Soc. Am.* B 8, 1226–1235 (1991).

[Chuang 1993] Y.-H. Chuang, L. Zheng, and D.D. Meyerhofer, *IEEE J. Quantum Electron.* **29** 270–280 (1993).

[Clayton 1994] C. Clayton, N. Kurnit, and D. Meyerhofer, *Proc. of Workshop on Gamma-Gamma Colliders*, Berkeley CA, USA (1994).

[Clayton 1995] C.E. Clayton, N.A. Kurnit, and D.D. Meyerhofer, *Nucl. Instr. and Methods* **A355**, 121–129 (1995).

[Corkum 1988] P.B. Corkum, F. Brunel, N.K. Sherman, and T. Srinivasan-Rao, *Phys. Rev. Lett.* **61**, 2886 (1988).

[Ditmire 1993] T. Ditmire and M.D. Perry, *Opt. Lett.* **18** 426 (1993).

[Eboli 1993] O.J.P. Eboli, M.C. Gonzalez-Garcia, F. Halzen, D. Zeppenfeld, *Phys. Rev.* **D48**, 1430 (1993); O.J.P. Eboli, talk given at Workshop on Gamma-Gamma Colliders, Lawrence Berkeley Laboratory, Berkeley, CA, USA (March 28–31, 1994).

[Fawley 1980] W.M. Fawley and E.P. Lee, "Modelling of Beam Focusing and Kink Instability for Colliding Relativistic Electron and Positron Beams", LLNL report *UCID–18584*, (1980).

[Fawley 1987] W.M. Fawley and E.P. Lee, E.P. "Modelling of Beam Focusing and Kink Instability Particle in Cell Simulations of Disruption", in *Proc. New Developments in Par. Accel. Techniques*, ed. S. Turner, **CERN 870-11**, **ECFA 87/110**, 605–609 (1987).

[Ferray 1990] M. Ferray, L.A. Lompre, O. Gobert, A. L'Huillier, G. Mainfray, C. Manus, A. Sanchez, and A.S. Gomes, *Opt. Commun.* **75**, 278 (1990).

[Ginzburg 1981] I. Ginzburg, G. Kotkin, V. Serbo, V. Telnov, *Pizma ZhETF* **34** 514 (1981); *JETP Lett.* **34** 491 (1982); *Prep. INF* 81–50, Novosibirsk, in English (Feb. 1981).

[Ginzburg 1983] I. Ginzburg, G. Kotkin, V. Serbo, V. Telnov, *Nucl. Instr. and Methods* **205**, 47 (1983); *Prep. INP* 81–92, (Novosibirsk, Aug. 1981).

[Ginzburg 1984] I. Ginzburg, G. Kotkin, S. Panfil, V. Serbo, V. Telnov, *Nucl. Instr. and Methods* **219**, 5 (1984).

[Ginzburg 1994] I. Ginzburg, *Proc. of Workshop on Gamma-Gamma Colliders*, Berkeley CA, USA (1994); *Nucl. Instr. Methods A* **355**, 63 (1995).

[Gounaris 1995] G.J. Gounaris, J. Layssac, F.M. Renard, PM–95–11, May 1995. 23 pp.; e-Print Archive: hep-ph/9505430

[Grzadkowski 1992] B. Grzadkowski and J.F. Gunion, *Phys. Lett.* **B294**, 361 (1992).

[Gunion 1993] J.F. Gunion and H.E. Haber, *Phys. Rev.* **D48**, 5109 (1993).

[Gunion 1995] J.F. Gunion, J.G. Kelly, J. Ohnemus, *Phys. Rev.* **D51**, 2101 (1995).

[Heinrich 1991] J.G. Heinrich, C. Lu, K.T. McDonald, C. Bamber, A.C. Melissinos, D. Meyerhofer, Y. Semertzidis, Pisin Chen, J.E. Spencer, R.B. Palmer, "Proposal for a Study of QED at Critical Field Strengths in Intense Laser–High-Energy Electron Collisions", SLAC–Proposal–E–144 (October 1991).

[Heinz 1989] P. Heinz and A. Laubereau, *J. Opt. Soc. Am.* **B 6**, 1574 (1989).

[Hiramatsu 1995] S. Hiramatsu, S. Hashimoto and Y. Ishida, *Proc. of Workshop on Gamma-Gamma Colliders*, Berkeley CA, USA (1994); *Nucl. Instr. Methods A* **355**, 133 (1995).

[Hollebeek 1981] R. Hollebeek, "Disruption Limits for Linear Colliders", *Nucl. Instr. and Methods* **184**, 333 (1981).

[Horton-Smith phd] G. Horton-Smith, Ph.D. Thesis, SLAC.

[Injean 1994] H. Injean *et al.,* "Diode array, kilowatt laser development", Conference on Lasers and Electro-Optics (CLEO), pp. CThC1 (Anaheim, CA, 1994).

[Jikia 1993] G.V. Jikia, *Phys. Lett.* **B298**, 224 (1993); *Nucl. Phys.* **B405**, 24 (1993).

[Jikia 1994a] G. Jikia and A. Tkabladze, invited talk at Workshop on Gamma-Gamma Colliders, Berkeley, CA, 28-31 (Mar 1994).

[Jikia 1994b] G. Jikia, IFVE-94-77, 34 pp. (Jul 1994); e-Print Archive: hep-ph/9407393.

[Kamal 1995] B. Kamal, Z. Merebashvili, A.P. Contogouris, *Phys. Rev.* **D51**, 4808 (1995).

[Kim un] K.-J. Kim, A. Sessler, M. Xie, report al LC95, to be published.

[Kim 1994] Prepared by K.-J. Kim, P. Pierini, A. Sessler, V. Telnov at LC95, KEK, Japan, (March 1994).

[Kmetec 1991] J.D. Kmetec, J.J. Macklin, and J.F. Young, *Opt. Lett.* **16**, 1001–1003 (1991).

[Kon 1992a] T. Kon and A. Goto, *Phys. Lett.* **B295**, 324 (1992); F. Cuypers, G.J. van Oldenborgh, R. Rückl, *Nucl. Phys.* **B383**, 45 (1992).

[Kon 1992b] T. Kon, I. Ito, and Y. Chikashige, *Phys. Lett.* **B287**, 277 (1992).

[Kon 1993] T. Kon, *Phys. Lett.* **B316**, 181 (1993); F. Cuypers, G.J. van Oldenborgh, R. Rückl, *Nucl. Phys.* **B409**, 144 (1993).

[Kondratenko 1983] A. Kondratenko, E. Pakhtusova, E. Saldin, *Dokl. Akad. Nauk* **264**, 849 (1982).

[Kramer 1994] M. Kramer, J. Kuhn, M.L. Stong, and P.M. Zerwas, *Z. Phys.* **C64**, 21 (1994).

[Landau 1987] L.D. Landau and E.M. Lifshitz, "The Classical Theory of Field", Course of Theoretical Physics 2, (Pergamon Press, 1987).

[Martinez 1987] O.E. Martinez, *IEEE J. Quantum Electron.* **QE-23**, 59–64 (1987).

[Meyerhofer 1995a] D. Meyerhofer, *Proc. of Workshop on Gamma-Gamma Colliders*, Berkeley CA, USA (1994); *Nucl. Instr. Methods A* **355**, 113–120 (1995).

[Meyerhofer 1995b] D.D. Meyerhofer, *Nucl. Instr. and Methods* **A355** 113-120 (1995).

[Miller 1995] D.J. Miller, *Nucl. Instr. and Methods* **A355**, 101 (1995).

[Morton 1995] P. Morton and S. Chattopadhyay, *Proc. of Workshop on Gamma-Gamma Colliders*, Berkeley CA, USA (1994); *Nucl. Instr. Methods A* **355**, 138 (1995).

[Murayama 1994] H. Murayama, talk at Workshop on Gamma-Gamma Colliders, Berkeley, CA (28-31 Mar 1994).

[Norem 1995] J. Norem, *Proc. of Workshop on Gamma-Gamma Colliders*, Berkeley CA, USA (1994); *Nucl. Instr. Methods A* **355**, 166 (1995).

[Ohgaki 1995] T. Ohgaki and X. Yokoya, to be published.

[Orzechowski 1990] Reference on Paladin–T.J. Orzechowski at 1990 USPA School.

[Perry 1990a] M. Perry and F. Patterson, *Opt. Lett.* **15**, 381 (1990).

[Perry 1990b] M.D. Perry and F.G. Peterson, LLNL Internal Documents (1990); M.D. Perry, T. Ditmire, and D. Strickland, *Opt. Lett.* **17**, 601 (1992).

[Perry 1991] M.D. Perry and R. Olson, *Laser Focus World* bf 27, 69-74 (1991).

[Perry 1994a] For a review, see M. Perry and G. Mourou, M.D. Perry and G. Mourou, *Science* **264**, 917-924 (1994).

[Perry 1994b] M.D. Perry, T. Ditmire, and B.C. Stuart, *Opt. Lett.* **19**, 2149 (1994).

[Perry 1995] M.D. Perry, R.D. Boyd, J.A. Britten, D. Decker, B.W. Shore, C. Shannon, and E. Shults, *Opt. Lett.* **20**, 940–942 (1995).

[Perry 1996] M.D. Perry, J.A. Britten, R.D. Boyd, H. Nguyen, B.W. Shore, U.S.Patent Pending.

[Raidal 1995] M. Raidal, *Nucl. Phys.* **B441**, 49 (1995).

[Rajagopalan 1994] S. Rajagopalan, D. Cline and P. Chen, *Proc. of Workshop on Gamma-Gamma Colliders*, Berkeley CA, USA (1994); *Nucl. Instr. Methods A* **355**, 169 (1995).

[Rajagopalan 1996] S. Rajagopalan, D.B. Cline, P. Chen, "Application of a Plasma Lens to $e^-\gamma$ Colliders", these Proceedings.

[Richard 1995] F. Richard, *Proc. of Workshop on Gamma-Gamma Colliders*, Berkeley CA, USA (1994); *Nucl. Instr. Methods A* **355**, 92 (1995).

[Rodwell 1986] M.J.W. Rodwell, K.J. Weingarten, D.M. Bloom, T. Baer, and B.H. Kolner, *Opt. Lett.* **11**, 638-640 (1986).

[Rodwell 1989] M.J.W. Rodwell, D.M. Bloom, and K.J. Weingarten, *IEEE J. Quantum Electron.* **25**, 817–827 (1989).

[Ronan 1993] M. Ronan, *Proc. of Workshop on Phys. and Exper. with Linear Colliders*, Waikoloa, Hawaii, US (1993).

[Salin 1991] F. Salin, C. Rouyer, J. Squier, S. Coe, and G. Mourou, *Opt. Commun.* **84**, 67 (1991).

[Saldin 1995] E. Saldin *et al.,* Preprint JINR E-9-94-74, Dubna,1994, Submitted to Particle and Accelerators; *Nucl. Instr. Methods A* **355**, 171; DESY 94-243,1994 (1995).

[Siegman 1986] A.E. Siegman, *Lasers* (University Science, Mill Valley, Ca, 1986).

[Silvestrov un] G. Silvestrov, V. Telnov (unpublished).

[Squier 1991] J.A. Squier, F. Salin, J.S. Coe, P. Bado, and G.A. Mourou, *Opt. Lett.* **15**, 85 (1991).

[Strickland 1985] D. Strickland and G. Mourou, *Opt. Commun.* **56**, 219 (1985); P. Maine, D. Strickland, P. Bado, M. Pessot, and G. Mourou, *IEEE J. Quantum Electron.* **QE-24**, 398 (1988).

[Stuart 1995a] B.C. Stuart *et al.,* submitted to JOSAB, UCRL–JC–120, 225.

[Stuart 1995b] B. Stuart, S. Herman, and M.D. Perry, *IEEE J. Quantum Electron.* **31**, 528 (1995).

[Stuart 1995c] B. Stuart, M.D. Feit, M.D. Perry, A.M. Rubenchick, and B.W. Shore, *Phys. Rev. Lett.* **74**, 2248 (1995).

[Takahashi 1994] T. Takahashi, "Physics of e^+e^-, γe^- and $\gamma\gamma$ collisions at Linear Accelerators", *Proc. INS Workshop*, Tokyo, Japan, 93 (1994).

[Takahashi 1995] T. Takahashi, Hiroshima Univ. Preprint, HUPD–9526 (1995).

[Takahashi 1996] T. Takahashi, in preparation.

[Tandean 1995] J. Tandean, *Phys. Rev.* **D52**, 1398 (1995).

[Tauchi 1993] T. Tauchi, K. Yokoya, P. Chen, *Particle Acclerators* **41**, 29 (1993).

[Telnov 1990] V. Telnov, *Nucl. Instr. Methods A* **294**, 72 (1990).

[Telnov 1991] V. Telnov, private communication and *Proc. of Workshop on Phys. and Exper. with Linear Colliders*, Lapland, Finland, 551 (1991).

[Telnov 1993] V. Telnov, *Proc. of Workshop on Physics and Experiments with Linear Colliders*, Wokoloa, Hawaii (World Scientific, 1993).

[Telnov 1995] V. Telnov, *Proc. of Workshop on Gamma-Gamma Colliders*, Berkeley CA, USA, (1994); *Nucl. Instr. Methods A* **355**, 3 (1995).

[Telnov priv] V. Telnov, private communication.

[Treacy 1969] E.B. Treacy, *IEEE J. Quantum Electron.* **QE–5**, 454 (1969).

[Watanbe 1995] I. Watanabe, talk presented at Workshop on Physics and Experiments with Linear e^+e^- Colliders, Appi, Japan, (1995).

[White 1992] W.E. White, J. Hunter, L. Van Woerkum, T. Dimitre, and M.D. Perry, *Opt. Lett.* **17**, 1067 (1992).

[Xie 1995] M. Xie, K.-J. Kim, and A.M. Sessler, *Nucl. Instr. and Methods* **355**, 163 (1995).

[Yehudai 1990] E. Yehudai, *Phys. Rev.* **D41**, 33 (1990).

[Yehudai 1991] E. Yehudai, *Phys. Rev.* **D44**, 3434 (1991).

[Yokoya, 1986] K. Yokoya, KEK–Report 85–9, October 1985; also *Nucl. Instr. and Methods* **A251**, 1 (1986).

[Yokoya 1996] *User's Manual of CAIN 2.0*, (KEK publication, April, 1996).

Contributors

- Karl van Bibber
- Swapan Chattopadhyay
- Bill Fawley
- Dick Helm
- Tim Houck
- John Irwin
- Kwang-Je Kim
- Dan Klem
- David Meyerhofer
- Hitoshi Murayama
- Micheal Perry
- Mike Ronan
- Andy Sessler
- Jim Spencer
- Tohru Takahashi
- Valery Telnov
- Achim Weidemann
- Glen Westenskow
- Ming Xie
- Kaoru Yokoya
- Sasha Zholents